Government of Western Australia

Department of
Mines and Petroleum

REPORT
114

IMAGING CRUSTAL STRUCTURE IN THE WEST MUSGRAVE PROVINCE FROM MAGNETOTELLURIC AND POTENTIAL FIELD DATA

by AR Aitken, MC Dentith, SF Evans, LA Gallardo, A Joly, S Thiel, RH Smithies, and IM Tyler

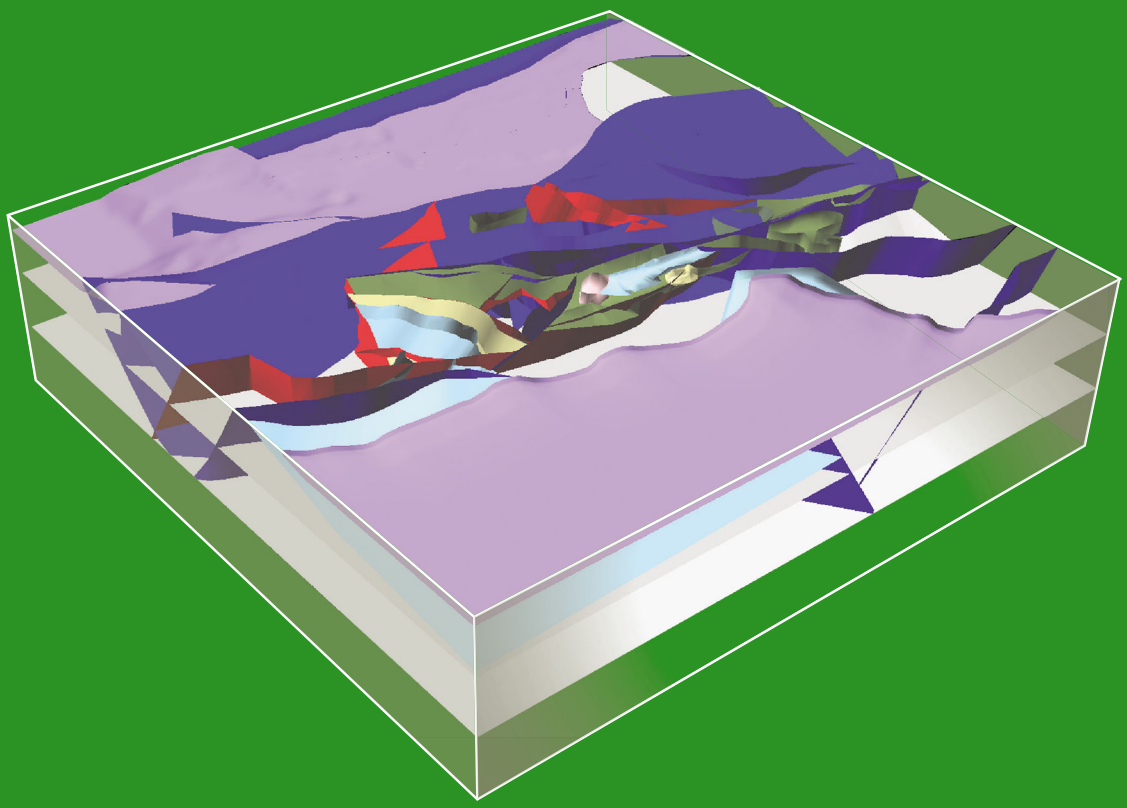

ROYALTIES FOR REGIONS
EXPLORATION INCENTIVE SCHEME

Centre for EXPLORATION TARGETING

Geological Survey of Western Australia

Government of Western Australia
Department of Mines and Petroleum

REPORT 114

IMAGING CRUSTAL STRUCTURE IN THE WEST MUSGRAVE PROVINCE FROM MAGNETOTELLURIC AND POTENTIAL FIELD DATA

by
AR Aitken[1], MC Dentith[1], SF Evans[2], LA Gallardo[1], A Joly[1], S Thiel[3], RH Smithies, and IM Tyler

[1] Centre for Exploration Targeting, The University of Western Australia, 35 Stirling Highway, Crawley, Perth WA 6009

[2] Moombarriga Geoscience, 32 Townshend Road, Subiaco WA 6008

[3] TRaX, Mawson Building, North Terrace Campus, The University of Adelaide, Adelaide SA 5005

Perth 2013

Geological Survey of Western Australia

REFERENCE
The recommended reference for this publication is:
Aitken, AR, Dentith, MC, Evans, SF, Gallardo, LA, Joly, A, Thiel, S, Smithies RH and Tyler, IM 2013, Imaging crustal structure in the west Musgrave Province from magnetotelluric and potential field data: Geological Survey of Western Australia, Report 114, 81p.

National Library of Australia Cataloguing-in-Publication entry

Title: Imaging crustal structure in the West Musgrave Province from magnetotelluric and potential field data / Alan Aitken ... [et al.]

ISBN: 9781741684834 (pbk.)

Series: Report (Geological Survey of Western Australia) ; 114.

Subjects: Remote sensing--Western Australia--Musgrave Province.
Geology, Structural--Western Australia--Musgrave Province.
Prospecting--Geophysical methods.
Magnetotelluric prospecting--Western Australia--Musgrave Province.
Gravity prospecting--Western Australia--Musgrave Province.

Other Authors/Contributors: Aitken, Alan.
Geological Survey of Western Australia

Dewey Number: 621.3678

ISSN 0508–4741

Grid references in this publication refer to the Geocentric Datum of Australia 1994 (GDA94). Locations mentioned in the text are referenced using Map Grid Australia (MGA) coordinates, Zone 52. All locations are quoted to at least the nearest 100 m.

Copy editor: SR White
Cartography: M Prause
Desktop publishing: RL Hitchings
Printed by Images on Paper, Perth, Western Australia

Published 2013 by Geological Survey of Western Australia
This Report is published in digital format (PDF) and is available online at <www.dmp.wa.gov.au/GSWApublications>.

Further details of geological publications and maps produced by the Geological Survey of Western Australia are available from:
Information Centre
Department of Mines and Petroleum
100 Plain Street
EAST PERTH WESTERN AUSTRALIA 6004
Telephone: +61 8 9222 3459 Facsimile: +61 8 9222 3444
www.dmp.wa.gov.au/GSWApublications

Cover image: 3D model of the crustal structure of the west Musgrave Province showing the geometry of lithological units, Giles Event aged faults, and Petermann Orogeny aged faults

Contents

Appendix

Figures

Tables

Imaging crustal structure in the west Musgrave Province from magnetotelluric and potential field data

by

AR Aitken[1], MC Dentith[1], SF Evans[2], LA Gallardo, A Joly[1], S Thiel[3], RH Smithies, and IM Tyler

Abstract

The west Musgrave Province in central Australia occupies a position at the intersection between the South, West, and North Australian Cratons, and was a focal point for tectonic activity from the Mesoproterozoic through to the latest Proterozoic. The series of tectonic events includes two Mesoproterozoic orogenic events (the Mount West and Musgrave orogenies), a major intraplate rift event (the Giles Event), and two episodes of compressional intraplate orogenesis (the Petermann and Alice Springs orogenies). As a result of this activity, the west Musgrave region may be prospective for several types of mineral deposits, principally Ni–Cu–PGE, for which the world class Nebo–Babel deposit is the major occurrence, but also nickeliferous laterites, orogenic and intrusive gold, and, potentially, iron oxide – copper – gold. Here, we use magnetotelluric (MT), gravity, and magnetic data to determine the crustal structure of this region, with a particular focus on identifying the geometry of large-scale faults and shear zones that may be prospective for mineralization.

MT data were collected specifically for this work along two orthogonal profiles. These profiles show that the region is dominated by resistive lithosphere, within which several conductive zones are recognized. Several of these relate to deep-penetrating faults or shear zones that may have been important pathways for mineralizing fluids. Petrophysical data (density and magnetic susceptibility) were collected for the main lithological groups, and were used to constrain potential field modelling of crustal structure. 2D gravity and magnetic forward modelling provides a broad overview of crustal structure, and develops a link between geological observations and the lithospheric structure revealed in the MT data. These results are built on by the construction of an interpretative 3D model. Subsequent gravity and magnetic inversions show that this model is acceptable given the petrophysical constraints, although alternative geometries are investigated also.

Together, the results of these geophysical investigations suggest that the west Musgrave Province is dominated by the structure of the Giles Event and the Petermann Orogeny. The Giles Event was characterized initially by the intrusion of enormous quantities of mafic magma along an ESE–WNW trending rift axis. Subsidiary ENE trends are observed later in the event. This intrusive event was followed by the deposition of thick volcanic–sedimentary packages of the Bentley Supergroup. The forward models indicate that primary layering within these units dips shallowly to the south to southwest, although this is disrupted in many places by faulting and folding that occurred in the later stages of the Giles Event. Previous studies indicated that the Petermann Orogeny was characterized by three types of deformation: low-angle thrust faulting and nappe-style folding dominate in the footwall of the Woodroffe Thrust; low-angle thrusts and crustal flow zones dominate in the hanging wall of the Woodroffe Thrust; and high-angle transpressional shear zones dominate in the core of the orogen, south of the Mann Fault. Our models are consistent with this, and also show that the intensity of the Petermann Orogeny decreases to the south and west. The crustal structure revealed by these studies defines the geometries of numerous features that are potentially prospective for mineralization, including the large Giles Suite mafic intrusions, and major crust-penetrating shear zone networks.

KEYWORDS: geophysical models, image analysis, image interpretation, lithology, magnetic data, magnetic surveys, magnetic susceptibility, resistivity, structural terranes

---

1 Centre for Exploration Targeting, The University of Western Australia, 35 Stirling Highway, Crawley WA 6009

2 Moombarriga Geoscience, 32 Townshend Road, Subiaco WA 6008

3 TRaX, Mawson Building, North Terrace Campus, The University of Adelaide, Adelaide SA 5005

Introduction

The Musgrave Province is located in central Australia, straddling the border between Western Australia and South Australia, and extending northwards into the Northern Territory (Fig.1). The west Musgrave Province consists of the part of the Musgrave Province located west of longitude 129º E, i.e. within Western Australia.

The geology of the west Musgrave Province has been a subject of intense study by the Geological Survey of Western Australia (GSWA) (Smithies et al., 2009a; Evins et al., 2010; Smithies et al., 2011). This work has greatly improved the understanding of the geology and geological history of the west Musgrave Province, and resulted in a major increase in the amount of geoscientific data available. Based on these new datasets, the west Musgrave Province is generally considered to be under-explored relative to its potential. The most important occurrence of mineralization is the world class Nebo–Babel Ni–Cu–PGE deposit, and other known mineralization includes nickeliferous laterites and lode gold. The region is also potentially prospective for other types of mineralization; for example, iron oxide – copper – gold and uranium (for more detail see Joly et al., 2013).

Funded by the Western Australian Government's Exploration Incentive Scheme, the Centre for Exploration Targeting <www.cet.uwa.edu.au> at The University of Western Australia has undertaken a study of the prospectivity of the west Musgrave Province in association with the GSWA. This work is described in this report, and also in a companion report that analyses the structural evolution of the area and its mineral prospectivity (Joly et al., 2013). In the present report the sub-surface geometry of major geological entities in the west Musgrave Province is described with emphasis on delineating deep penetrating fault zones, which are considered to be likely conduits for hydrothermal fluids and magmas and therefore are potentially important indicators of prospectivity. The basis for this study is magnetotelluric (MT) data collected specifically for this study, and modelling of existing regional gravity and aeromagnetic data. The MT data are necessarily limited in extent to two 2D profiles but are deeply penetrating in that they contain responses from mantle depths. The gravity and magnetic data extend over the entire study area but are most useful for determining structure at upper crustal depths. A detailed and systematic structural and stratigraphic interpretation of the gravity and magnetic data in map form is described in the companion report (Joly et al., 2013). An important outcome from Joly et al. (2013) is the assignment of ages of formation and/or reactivation of observed structures. In this report we present the results of modelling variations in total magnetic intensity and free-air gravity along a series of profiles, two of which coincide with the MT traverses. Furthermore, we develop an interpreted 3D model of crustal structure, and test this model using 3D gravity and magnetic inversions. To constrain the potential field modelling, a database of density and magnetic susceptibility measurements has been created using samples in the GSWA rock store.

In the companion report (Joly et al., 2013), the prospectivity of the west Musgrave Province is quantitatively assessed using a fuzzy logic-based method and a mineral systems analysis in a GIS framework. This work is based on all available geoscientific data including the new work described here, plus a new interpretation of the gravity and magnetic data emphasizing the age and history of major structures described in the companion report.

Geology of the west Musgrave Province

The geological history recognized in the west Musgrave Province took place mostly during the Mesoproterozoic and comprised several magmatic and metamorphic–tectonic events (Table 1), resulting in a complex geology. As a result of extensive mapping, and geologically constrained interpretation of potential field data, this geology is relatively well understood in the west Musgrave Province. Recent publications describe the results of this work in detail (Evins et al., 2010; Howard et al., 2011; Smithies et al., 2009a; Smithies et al., 2011; Joly et al., 2013). The main events and their likely influence on crustal structure are summarized below.

Mesoproterozoic Tectonic Events

The early Mesoproterozoic evolution of the Musgrave Province remains poorly understood, although recent work has established possible inception as an arc at c. 1600 Ma (Edgoose et al., 2004; Wade et al., 2006). Evidence for a c. 1600 Ma formation age is lacking in Western Australia; however, there is evidence for a magmatic event at c. 1400 Ma (Smithies et al., 2009a). The c. 1345–1150 Ma evolution of the Province is better defined, and is characterized by two phases of orogenesis: the 1345–1290 Ma Mount West Orogeny (Howard et al., 2009; Smithies et al., 2011) and the 1220–1150 Ma Musgrave Orogeny (Aitken and Betts, 2008; Wade et al., 2008; Smithies et al., 2011). Preserved structures from these events exist at relatively small scales, and it is difficult to link these explicitly to the larger scale crustal structure with any confidence. Nevertheless, it is likely that current crustal structure is to some degree controlled by the architecture of these early events.

The Mount West Orogeny

The Mount West Orogeny is characterized by granitic magmatism (The Wankanki Supersuite; Fig. 1) and limited volcanism, as well as the deposition of the sedimentary rocks that make up the Wirku Metamorphics (Howard et al., 2009; Smithies et al., 2011). The granulite facies paragneisses of the Wirku Metamorphics contain several suites of rocks that may represent the metamorphosed and tectonically dissected remnants of an originally continuous sedimentary basin (Smithies et al., 2009a). The Wankanki Supersuite is characterized by

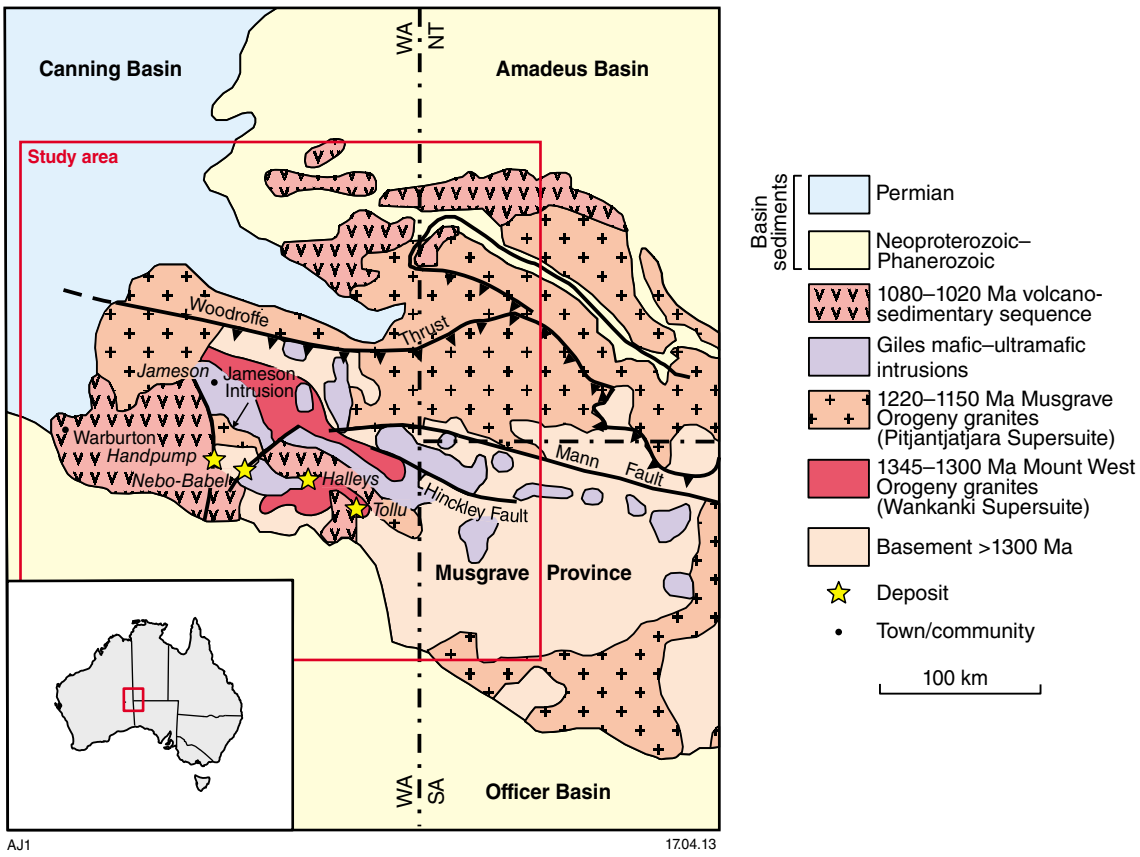

Figure 1. Regional geological sketch of the west Musgrave Province. Modified by Smithies et al. (2009a) from Glickson et al. (1996) and Edgoose et al. (2004).

porphyritic granodiorites and monzogranites, typically with a significant mafic mineral component, including clinopyroxene, orthopyroxene, and hornblende (Smithies et al., 2009a). Currently, U–Pb SHRIMP dating on these granites suggests magmatism extended from 1345 to 1293 Ma, but with most granites emplaced between 1326 and 1312 Ma. The chemistry of these granites (Smithies et al., 2009a), and correlations with the Albany–Fraser Province (Clarke et al., 1995; White et al., 1999), suggests a continental arc setting for this event, although this interpretation is not especially well constrained. Deformation associated with the Mount West Orogeny is observed in several localities (Glikson et al., 1995; Stewart, 1995; Joly et al., 2013). This deformation takes the form of bedding-parallel foliation, and tight to isoclinal folding of this foliation. However, this deformation does not permit the tectonic setting or large-scale crustal architecture to be constrained further (Joly et al., 2013).

The Musgrave Orogeny

The Musgrave Orogeny is defined by ultra-high temperature metamorphism with widespread granitic magmatism (The Pitjantjatjara Supersuite; Fig. 1) and deformation of prior fabrics (Edgoose et al., 2004; Smithies et al., 2011). In the west Musgrave Province, the Pitjantjatjara Supersuite includes high-grade granitic gneisses and charnockites. Current U–Pb SHRIMP dating suggests magmatism extended from 1220 to 1155 Ma, and may indicate several sub-groupings, although there is significant overlap between these (Smithies et al., 2009a; Smithies et al., 2011). Rocks of the Pitjantjatjara Supersuite are chemically distinct from the Wankanki Supersuite, and this chemistry suggests within-plate, A-type magmatism (Smithies et al., 2009a). Observed deformation within the west Musgrave Province indicates NW–SE shortening defined by close folding of the Wirku Metamorphics, the Wankanki Supersuite, and the Pitjantjatjara Supersuite during the Musgrave Orogeny (Joly et al., 2013). This deformation is relatively low-strain compared to the Musgrave Orogeny deformation interpreted in the eastern Musgrave Province (Aitken and Betts, 2008; Aitken and Betts, 2009a; Aitken and Betts, 2009b). Magmatic trends within the Pitjantjatjara Supersuite indicate that northwest-trending structures may also have been influential in controlling magma ascent (Smithies et al., 2009a).

The c. 1085–1040 Ma Giles Event

In Western Australia, the Giles Event is the dominant influence on the present-day geology (Glikson et al., 1996; Evins et al., 2010). Although significant deformation has been recognized (Evins et al., 2010; Joly et al., 2013), the Giles Event is primarily magmatic. Magmatism during the Giles Event was both intrusive and extrusive, resulting

Table 1. Geological and structural history of the west Musgrave Province

Age (Ma)	*Event*	*Specified event (Joly et al., 2013)*	*Age (Ma)*	*Structure description*	*Magmatic event*	*Tectonic setting*	*Metamorphic event*
1345–1290	Mt West Orogeny	MWO1	c. 1300	Earliest fabric (bedding?) in Wirku Metamorphics, and foliation in Wankanki Supersuite	Wankanki Supersuite	Convergent plate margin	Amphibolite to granulite facies metamorphism
		MWO2	c. 1300	Tight to isoclinal folding of MWO1, reasonably widespread throughout area, but not pervasive			
1220–1150	Musgrave Orogeny	EMO	c. 1220	Foliation and folds in Wankanki/Wirku Basement and Pitjantjatjara Supersuite; folded by MMO	Pitjanjatjara Supersuite	Intraplate orogen	Amphibolite to granulite facies ultra-high-temperature metamorphism (T >750°C, P = 5 ± 1 kb)
		MMO	1220–1180	Between early and late phases of Pitjantjatjara Supersuite. Widespread approximately NE-oriented close folding of Wankanki/Wirku basement and parallel shear zones.			
		LMO_MP	<1165	Fabric in Pitjantjatjara Supersuite north of Woodroffe Thrust			
		LMO	<1145	E–W trending fabric in Umutju granite — could be much younger			
			1155–1135	Fabric in Wirku Metamorphics and Pitjantjatjara Supersuite at Cohn Hill			
1085–1040	Giles Event	S_K	1085–1078	Bedding in Kunmarnara Group	Basalt and conglomerate	Intraplate rift event	
		S_G1	1078–1075	Igneous layering or contact in G1 intrusions	Emplacement of Bushveld-scale layered Giles intrusion at c. 1080 Ma; most abundant rock types are olivine gabbronorite to gabbronorite and troctolite		
		S_G2	1078–1074	Igneous layering or contact in G2 intrusions	Emplacement of massive gabbroic intrusions		
		EGE	1078–1075	Early fabrics and folding in Giles intrusions; syn-magmatic deformation			

Table 1. Geological and structural history of the west Musgrave Province (continued)

Age (Ma)	*Event*	*Specified event (Joly et al., 2013)*	*Age (Ma)*	*Structure description*	*Magmatic event*	*Tectonic setting*	*Metamorphic event*
		EGE2	c. 1075	N–S oriented tight to isoclinal folding and shear zones in Murray Range and Hinckley gabbro; syn-Giles 2			
		S_T	1073–1068	Bedding in Tollu Group	Smoke Hill Volcanics 1078 ± 3 Ma		
		S_TW	1090–1040	Bedding in Tjauwata Group			
		S_WK	1085–1040	Deformation surrounding Warakurna Supersuite granitoids	Tollu granite 1076 ± 9 Ma; Winburn granite 1077 ± 7 Ma		
		MGE1	1076–1072	Approximately E–W oriented tight folding of stratigraphy up to Tollu Group; syn-Tollu granite			
		MGE1_MP		Tight N-trending folding of LMO_MP			
		S_PC	1071–1065	Bedding/Contact in the Pussy Cat Group	Kathleen Ignimbrite 1071 ± 5 Ma		
		LGE1	1071–1065	NE-oriented normal faults, some associated with large magnetic lows. Includes proto-Cavenagh fault. Postdates Kathleen ignimbrite (1071 ± 5 Ma), pre-dates Warkurna Supersuite granite (1065 ± 9 Ma). Nebo babel intruded into this fabric?	Nebo–Babel 1068 ± 4.3 Ma		
		LGE2	1071–1065	ESE oriented shear zones with relatively minor folding			
		LGE2_MP		ESE oriented shear zones and close folding of prior fabrics			
		S_P	1077–1064	Bedding in the Mount Palgrave Group	Granitic dyke suites 1068 ± 6 Ma; 1052 ± 11 Ma		
		LGE3	1068–1067	N–S oriented shear zones and dykes and fault-related folding. Includes Jamieson Fault of Seat et al. (2007), which cuts Nebo-Babel, and prospective Harcus intrusion in South Australia			
		S_S	1072 ± 8	Saturn intrusion emplaced, with associated deformation			
		S_C	1065–1057	Bedding in the Cassidy Group			
		S_M	<1055	Bedding in the Mission Group			

Table 1. Geological and structural history of the west Musgrave Province (continued)

Age (Ma)	*Event*	*Specified event (Joly et al., 2013)*	*Age (Ma)*	*Structure description*	*Magmatic event*	*Tectonic setting*	*Metamorphic event*
1050–800	Post-Giles events						
c. 1000		PGE1	?	NNE–SSW oriented dykes. May be Kullal Dolerite (undated)	NE-trending type C olivine dolerite dyke suite		
c. 800		S_DQ	1040–800 Ma	Bedding in Dean Quartzite (sediment)	NW-trending type B quartz dolerite dykes	Rifting of Rodinia	
600–520	Petermann Orogeny	EPO		Shear zones of variable, but dominantly E–W, orientation; minor folding		Intraplate orogenesis linked to Gondwana assembly	Locally high pressure conditions (T = 650°C, P = 12 kb)
		EPO_MP		Earlier generation of E–W oriented shear zones			
		EPO_MP2		Petermann Nappe and westward extension			
		MPO		ESE-oriented anastomosing network of shear zones, with subordinate SW-oriented shear zones; minor folding			
		MPO_MP		N-directed thrusting			
		LPO		Late activity on the Woodroffe Thrust and associated splays			
		LPO_MP		Late activity on the Woodroffe Thrust and associated splays			
450–350	Alice Springs Orogeny	ASO	Permian	S-directed thrusting at southern margin of province, and reactivation of N-trending LGE3 shear zones		Intraplate orogenesis linked to Gondwana assembly	
		ASO_MP		Four north-trending shear zones			

in: 1) voluminous mafic intrusions of the Giles Suite; 2) widespread granitic intrusions; 3) abundant Alcurra Dolerite suite dykes and sills; 4) extensive bimodal volcanics of the Bentley Supergroup (see Fig. 1 for distributions of these units).

Recent work suggests that the Giles Suite can be separated into two main groups of intrusions. The first (G1) includes the layered mafic–ultramafic intrusions that make up the main ranges of the west Musgrave Province. From layer to layer, these intrusions range widely in composition; however, troctolite, gabbronorite, and gabbro dominate within the major intrusions of the Mamutjarra Zone (MZ, Fig. 2). In some cases these layers can be correlated between intrusions, suggesting that the G1 intrusions may, in part, represent a vast and once-continuous intrusion (Smithies et al., 2009a). The age of these rocks is ill-constrained, but a minimum age of 1078 ± 3 Ma (U–Pb SHRIMP) is obtained from a leucogranite within the Bell Rock intrusion (Sun et al., 1996). More recently, a sample of interpreted G1 layered leucogabbro at Mt Finlayson returned a U–Pb SHRIMP crystallisation age of 1076 ± 7 Ma (GSWA 194762; Kirkland et al., 2011).

The second group of intrusions (G2) includes massive gabbros that intrude into the G1 rocks. G2 rocks are characterized by fine- to medium-grained, leuco- to mesocratic-gabbro and gabbronorite (Evins et al., 2010). Characteristically, they also contain granitic material, interpreted to represent mingling of co-existing gabbroic and leucogranitic melts during emplacement (Evins et al., 2010). The leucogranitic material within massive Giles gabbros may represent part of a larger suite of granitic rocks that are widespread throughout the west Musgrave Province. Current U–Pb SHRIMP dating suggests granitic magmatism extending from 1078 Ma to at least 1065 Ma. Two major intrusions are of sufficient scale to be of note in this study: the 1077 ± 6 Ma (U–Pb SHRIMP) Winburn granite, and the 1076 ± 9 Ma (U–Pb SHRIMP) Tollu granite.

The Alcurra Dolerite is a younger suite of mafic intrusions. Most of these are relatively small dykes and sills, but some larger intrusions exist (e.g. the Saturn gabbro). This suite of rocks includes several mineralized examples, including the Nebo–Babel deposit, and the Tollu and Halleys prospects (Joly et al., 2013). Current isotopic dating suggests that magmatism occurred at c. 1072–1068 Ma (Seat et al., 2007; Evins et al., 2010), although field relationships suggest a more prolonged event concurrent with several phases of deformation (Joly et al., 2013).

Rocks of the Bentley Supergroup are present throughout the south and west of the west Musgrave Province, and dominate outcrop in the western Mamutjarra Zone. These rocks make up a thick sequence of volcanic, volcaniclastic and sedimentary rocks (Smithies et al., 2009a; Evins et al., 2010; Howard et al., 2011). This sequence of rocks spans the entire evolution of the Giles Event, and includes several groups. The basal group, the Kunmarnara Group, predominantly consists of basalts and conglomerates, although it also includes the rhyolitic to dacitic Skirmish Hill Volcanics (1078 ± 4 Ma; U–Pb SHRIMP). The major layered mafic–ultramafic intrusions (G1) intrude into the Kunmarnara Group indicating that these volcanic rocks predate the Giles Suite. The Tollu Group (1073 ± 7 Ma; U–Pb SHRIMP), consisting of rhyolitic to andesitic volcanic rocks, is a remnant of a presumably larger basin in the Blackstone region (Smithies et al., 2009b). The westernmost part of the Province preserves several sedimentary–volcanic packages. The Pussy Cat Group (1071 ± 5 Ma; U–Pb SHRIMP) consists of the Glyde Formation, dominated by mafic volcanic and volcaniclastic sedimentary rocks, and the Kathleen Ignimbrite, which is dominated by flow-banded rhyolites. The Mount Palgrave Group (1064 ± 7 Ma; U–Pb SHRIMP) is characterized by north-trending, west-dipping volcanic rocks, typically dacitic to rhyolitic, but including minor intercalations of basalt and sedimentary rocks. The Mount Palgrave Group includes the Scamp Formation, which also contains a unit with granofelsic texture, herein referred to as Scamp granite. The Bentley Supergroup is completed by the Cassidy and Mission (1065–1050 Ma) groups, each of which consist primarily of intercalated basalt and rhyolite layers. These rock packages dip shallowly to the south or southwest, are non-metamorphosed and are largely non-deformed, with the exception of some faults and long-wavelength folding.

At the large scale, the crustal structure of the Giles Event is characterized by a dominant ESE–WNW trend, reflecting the broad structure of the rift, although subordinate N–S and NE–SW trends are also observed (Evins et al., 2010; Joly et al., 2013). Constrained interpretation of geological, aeromagnetic, and gravity data permitted the definition of a sequence of deformation events throughout the Giles Event (Joly et al., 2013). Early Giles Event deformation is characterized by syn-magmatic deformation that both accommodates and is caused by the emplacement of Giles Suite intrusions (Joly et al., 2013). This includes the faults that bound the Murray Range Gabbro. Mid-Giles event deformation is characterized by shallowly east-plunging upright to north inclined close folding of layered Giles Suite intrusions, and also the Tollu Group (Evins et al., 2010; Joly et al., 2013). This deformation event is spectacularly preserved in the Blackstone region, but is also observed throughout the southeast Tjuni Purlka Tectonic Zone. Late Giles Event (LGE) deformation is characterized by three distinct sets of faults that cut the upper Bentley Supergroup, excepting the Mission Group. Overprinting relationships between these fault sets indicate a transition from northeast-trending normal faults (LGE1), east-southeast trending dextral transtensional faults (LGE2), to north-trending sinistral transtensional faults (LGE3) (Joly et al., 2013).

Neoproterozoic–Devonian intraplate orogenesis

Subsequent to the Giles Event, a prolonged period of sedimentation persisted until the latest Neoproterozoic, when the Musgrave Province region experienced the first of two major intraplate orogenic events, the c. 600–520 Ma Petermann Orogeny. Recent studies suggest that this orogenic event is characterized by three contrasting styles of deformation. Each of these

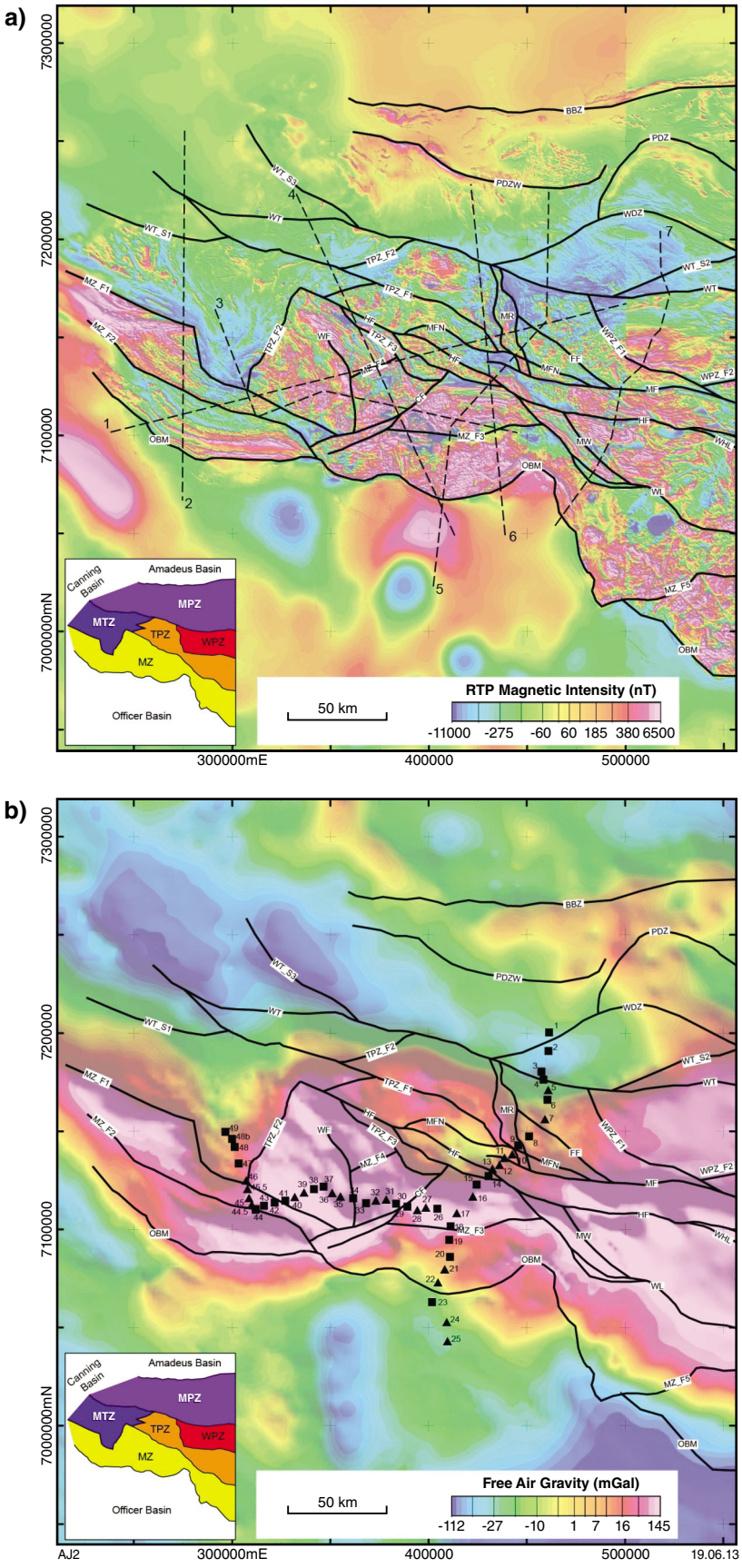

Figure 2. Map of the west Musgrave Province showing: a) reduced-to-pole aeromagnetic data, overlain by major faults and shear zones and the locations of gravity and magnetic forward modelling profiles (numbered dashed lines); b) free-air gravity data, overlain by major faults and shear zones, and the locations of MT stations (numbered). Squares indicate sites occupied with ANSIR equipment, whereas triangles indicate that Phoenix equipment was used. Named faults are denoted by: BBZ – Bloods Backthrust Zone, PDZ – Piltardi Detachment Zone, PDZW – Piltardi Detachment Zone West, WDZ – Wankari Detachment Zone, WT – Woodroffe Thrust, FF – Fanny Fault, MR – Murray Range, MF – Mann Fault, MFN – Mann Fault North HF – Hinckley Fault, WHL – Wintiginna–Hinckley Lineament, WL – Wintiginna Lineament, MW – Mount West Shear Zone, WF – Winburn Fault, CF – Cavenagh Fault, OBM – Officer Basin Margin. Unnamed faults are identified according to their zone (MZ_F1, TPZ_F1, and so on), and splays are indicated by an S prefix (e.g. WT_S1). Inset shows the major tectonic zones of the west Musgrave Province: MZ – Mamutjarra Zone, TPZ – Tjuni Purlka Zone, WPZ – Walpa Pulka Zone, MTZ – Mitika Zone, MPZ – Mulga Park Zone.

deformation styles indicates approximately N–S-oriented shortening, but there is a clear partitioning of deformation style between the foreland (The Mulga Park Zone), the deep crust (the Walpa Pulka Zone), and the hinterland (The Tjuni Purlka Tectonic Zone). In the Mulga Park Zone of the Northern Territory, deformation is characterized by low-angle thrust faulting and nappe-style folding that involves both granitic basement and the overlying cover sequences (Edgoose et al., 2004; Flöttmann et al., 2005). Within the Walpa Pulka Zone, ductile upwards flow of lower-crustal material is identified along low-angle structures (Raimondo et al., 2010). Finally, transpressional shearing on high-angle crustal-scale shear zones, which divide regions exhibiting little deformation, is identified (Aitken et al., 2009a). Within South Australia, this last style of deformation involves significant vertical offset of the lower crust and crust–mantle boundaries (Lambeck and Burgess, 1992; Aitken et al., 2009a; Korsch and Kositcin, 2010). In the west Musgrave Province, Petermann Orogeny structures are widespread, and are found in all tectonic zones, although the frequency and magnitude of faults decreases to the south and west (Joly et al., 2013). Geological mapping and aeromagnetic interpretation indicate that this tectonic event may comprise several deformation events (Glikson et al., 1995; Joly et al., 2013), although a paucity of isotopic dating and lack of magmatism means that the ages of these deformation events are poorly constrained.

The final event to have affected the Musgrave Province is the c. 450–350 Ma Alice Springs Orogeny. This event is most intense to the north, in the Arunta Province and Amadeus Basin. However, two major structures have been identified in the west Musgrave Province that are associated with this event. Seismic data within South Australia indicate that early Paleozoic strata within the Officer Basin have been monoclinally upturned as a result of thrust faulting at the southern margin of the Musgrave Province (Lindsay and Leven, 1996). Although the exact nature of this boundary in Western Australia is ill-constrained, it is likely that this structure continues for some distance. The second structure considered to have been active during the Alice Springs Orogeny is the Lasseter–Mundrabilla shear zone, which may have accommodated the differential strain between shortening to the east and extension to the west (Braun et al., 1991). The trace of this structure is approximately demarcated in the aeromagnetic data by a zone of smooth texture that indicates the presence of a sandstone unit (Fig. 2a).

Economic geology

The economic geology of the west Musgrave Province is described in more detail in Joly et al. (2013). Abeysinghe (2003) reviewed mineral occurrences and exploration activity in the west Musgrave Province up to 2002, and an update is provided in Howard et al. (2011). By far the most important occurrence of mineralization in the west Musgrave Province is the Nebo–Babel Ni–Cu–PGE deposit. Massive and disseminated sulphide mineralization occurs within a shallowly WSW-plunging pipe of gabbronorite (Sun et al., 1996). The host intrusion is a component of the Alcurra Dolerite Suite. Baker and Waugh (2005) provide a description of the discovery of the Nebo–Babel deposit. The geology of the deposit is described by (Seat et al., 2007).

Magnetotelluric survey

The magnetotelluric (MT) survey involved two orthogonal traverses (Fig. 2b) and was designed to cross major faults in the west Musgrave Province, and also to cross a major positive gravity anomaly of uncertain origin but postulated to be associated with a large magma chamber in the subsurface. An improved understanding of the extent and relationships between major crustal domains/terranes (see Fig. 2 inset), and the intervening large-scale structures in the study area, was the primary motivation for the MT survey in the west Musgrave Province.

The magnetotelluric method is a deep-penetrating, passive (natural-source), frequency-domain electromagnetic method which allows variations in electrical conductivity to be mapped in the crust and upper mantle. For a comprehensive description of the method the reader is referred to Simpson and Bahr (2005). Briefly, natural fluctuating magnetic fields, due to the interaction of the geomagnetic field and the solar wind, and at higher frequencies lightning strikes, induce telluric (electric) currents in the Earth. These variations span a broad range of frequencies/periods. Note that both the terms frequency and period are used when describing MT data. Frequency (f) in Hertz (Hz) is the reciprocal of period (P) in seconds (s).

It is because the magnetic fields vary at a range of frequencies that electrical conductivity variations at depth can be determined. The penetration, i.e. attenuation with distance, of an electromagnetic field into a medium depends on the medium's electrical conductivity and the frequency of the variations in the electromagnetic field. Lower frequencies penetrate more deeply and greater sub-surface conductivity reduces penetration for a given frequency. After recording, the electric and magnetic fields can be mathematically separated into components with different frequencies, and therefore electrical properties at different depths can be estimated. For this reason, during the description of the processing and interpretation of the MT data (see below), period can be thought of as a proxy for depth. However, because the conductivity of the Earth varies from location to location, the conversion factor from period to depth will also vary. The maximum period (depth) of interest dictates the length of the time interval over which the variations in the electric and magnetic fields must be recorded. To achieve penetration to mantle depths requires recording for several tens of hours.

Data acquisition

The MT data were collected by personnel from Moombarriga Geoscience, the Centre for Exploration Targeting at The University of Western Australia, and the Geological Survey of Western Australia. The survey comprised 51 stations and data were acquired in a single campaign in April 2011. Coordinates for all the MT stations are given in Table 2. MT equipment came from two sources: Moombarriga Geoscience and the

Australia National Seismic Imaging Resource (ANSIR). The equipment differed in important respects requiring different field practices and set-ups.

Figure 3 is a schematic illustration of the equipment layout at each MT station. For both types of equipment two (horizontal) components of the electric field were measured using non-polarizable electrodes and three components of the magnetic field variation were measured using coil sensors. The coils are sensitive to noise and this is reduced by burying them; a significant task, especially for a vertical coil, because these are approximately 2 m in length. Electric dipoles and horizontal coils were installed in magnetic north–south and east–west azimuths. Each site was occupied for approximately 40 hours. Exact details of deployment are given in Table 2.

The Phoenix set-up (Fig. 3a) used a Phoenix Ltd MTU-5A data recorder with MTC-50 magnetic induction coils. The electric dipoles were approximately 100 m in length and deployed in a cross array with an earth electrode near the centre. The electric field was measured using non-polarising ($Pb/PbCl_2$ solution) electrodes.

The ANSIR set-up (Fig. 3b) used an Earth Data PR6-24 Portable Field Recorder with KMS LIC-120 induction coils. The electric dipoles were 50 m in length and deployed with an L-shape with a common electrode at the southern or western end of each, respectively. The electric field was measured using non-polarizing Tinker & Rasor, model 3A ($Cu/CuSO_4$ solution) electrodes.

Survey sites were all relatively flat and most sites were remote from any sources of cultural electromagnetic noise.

At every MT station, time-domain electromagnetic soundings were made using a TerraTEM transmitter and receiver. A 100 m-sided square transmitter loop (Tx area = 10 000 m^2) was used with sides oriented north–south and east–west. The receiver coil had a 1-m side length (Rx area = 105 m^2). The TerraTEM 'intermediate' time series was used (135 channels between 0.0015 and 1900 ms). A minimum of four soundings were made at each site.

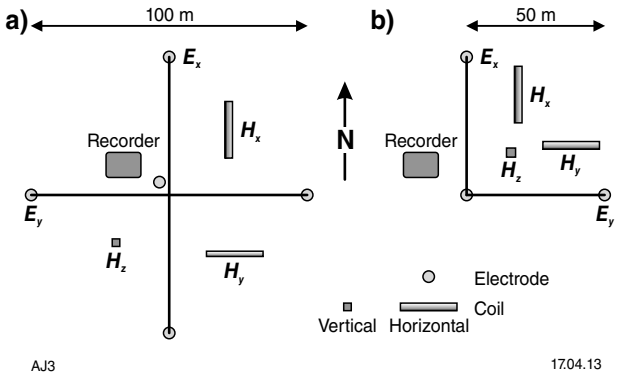

Figure 3. Schematic illustration of equipment set-up at each magnetotelluric (MT) station: a) Phoenix equipment; b) ANSIR equipment. *E* – electric field sensor, *H* – magnetic field sensor

Visual checks were made to ensure these data were self-consistent and were not obviously noisy, with additional soundings made if necessary.

Data processing

Variations of the electric and magnetic field components are recorded as a function of time; i.e. these data comprise time series and are in the 'time domain'. The MT data are subsequently converted to the 'frequency domain'. This enables parameters of interest to be calculated as a function of frequency (or period) and subsequently used to model electrical property variations as a function of depth.

Examples of partial electric and magnetic field time series from sample stations are shown in Figure 4. These series were checked in the field to ensure that there had been adequate variation in the geomagnetic field for the data to be useful, and also to check that the equipment was deployed correctly, as can be determined by the relationships between the different time series. Electric field measurements are designated E, for which the north–south component is termed E_x and the east–west component E_y. Magnetic field components are designated as H, with the same notation, plus H_z defining the vertical component.

The Phoenix time-series data were processed using robust remote-reference algorithms supplied by Phoenix Limited, and based on the coherence-sorted cascade decimation method of Wight and Bostick (1981) and the heuristic robust approach of Jones and Jödicke (1984). Remote reference processing (Gamble et al., 1979) compares recordings from different locations to identify noise in the time series, whereas the coherence-based methods are based on statistical comparison of the various time series. A simultaneously recording station within the traverse was used as the remote reference. The ANSIR time series were processed using the BIRRP code (Chave and Smith, 1994) and the sequential processing tools developed by the University of Adelaide (G Heinson, written comm.). This combination allows a robust estimation of the impedance tensor functions for selected frequencies using a window averaging technique (Chave et al., 1987).

Frequency-domain MT responses

The same dataset as (partly) shown in Figure 4 is presented in Figure 5 after being transformed into the frequency domain. Two parameters, apparent (electrical) resistivity and phase as a function of period, are shown. The two curves on each plot are called the TM and TE modes (see below). Note that electrical resistivity ρ (rho), is the reciprocal of electrical conductivity.

In general, data quality from the survey is good, as indicated by the small error bars in Figure 5 up to periods of about 1000 s. A complete set of apparent resistivity and phase curves is shown in Appendix 1.

The apparent resistivity values for each period were calculated as follows. Apparent resistivity can be written in terms of the electric (E) and magnetic (H) fields:

Table 2. Locations and recording times of MT stations

Site	Equipment	Latitude	Longitude	Elevation (metres)	Start time	End time	Duration (hours)
MUS001	ANSIR	-25.313450	128.615580	623	12/04/2010 2:29	13/04/2010 1:56	23.45
MUS002	ANSIR	-25.399520	128.611260	613	11/04/2010 4:23	13/04/2010 1:09	44.77
MUS003	ANSIR	-25.492250	128.575700	601	11/04/2010 3:08	13/04/2010 0:34	45.43
MUS004	ANSIR	-25.528810	128.585500	612	10/04/2010 7:27	12/04/2010 1:17	41.83
MUS005	Phoenix	-25.576033	128.611267	603	10/04/2010 7:00	12/04/2010 0:22	41.37
MUS006	ANSIR	-25.621360	128.605630	601	10/04/2010 5:20	12/04/2010 0:22	43.03
MUS007	Phoenix	-25.710100	128.593500	608	10/04/2010 10:00	11/04/2010 23:45	37.75
MUS008	ANSIR	-25.789390	128.512970	571	09/04/2010 7:00	11/04/2010 0:49	41.82
MUS009	ANSIR	-25.832880	128.456180	564	09/04/2010 8:20	10/04/2010 23:40	39.33
MUS010	Phoenix	-25.872933	128.427450	553	09/04/2010 4:00	10/04/2010 23:33	43.55
MUS011	Phoenix	-25.887800	128.386533	552	09/04/2010 7:00	11/04/2010 0:21	41.35
MUS012	Phoenix	-25.919483	128.361733	565	11/04/2010 4:00	12/04/2010 23:20	43.33
MUS013	Phoenix	-25.938567	128.325600	542	11/04/2010 6:00	13/04/2010 0:08	42.13
MUS014	ANSIR	-25.973180	128.305800	555	14/04/2010 1:28	15/04/2010 23:21	45.88
MUS015	ANSIR	-26.010410	128.243500	553	12/04/2010 6:36	13/04/2010 23:46	41.17
MUS016	Phoenix	-26.063783	128.224983	535	12/04/2010 4:00	13/04/2010 23:48	43.80
MUS017	Phoenix	-26.141450	128.144167	524	12/04/2010 6:00	13/04/2010 21:47	39.78
MUS018	ANSIR	-26.201480	128.110150	540	13/04/2010 6:41	15/04/2010 0:03	41.37
MUS019	ANSIR	-26.265050	128.103750	541	13/04/2010 8:21	14/04/2010 23:16	38.92
MUS020	ANSIR	-26.340860	128.107070	571	14/04/2010 4:13	16/04/2010 1:47	45.57
MUS021	Phoenix	-26.399967	128.081233	550	13/04/2010 3:30	14/04/2010 23:14	43.73
MUS022	Phoenix	-26.457717	128.044467	523	13/04/2010 5:00	14/04/2010 23:54	42.90
MUS023	ANSIR	-26.548900	128.012260	488	14/04/2010 7:05	15/04/2010 23:59	40.90
MUS024	Phoenix	-26.640917	128.088483	481	14/04/2010 5:30	15/04/2010 21:45	40.25
MUS025	Phoenix	-26.730467	128.092083	464	14/04/2010 4:00	15/04/2010 17:47	37.78
MUS026	ANSIR	-26.120510	128.043880	508	16/04/2010 8:14	17/04/2010 23:49	39.58
MUS027	Phoenix	-26.114717	127.986083	504	16/04/2010 6:00	17/04/2010 23:55	41.92
MUS028	Phoenix	-26.125817	127.941867	510	16/04/2010 5:00	18/04/2010 0:25	43.42
MUS029	ANSIR	-26.109660	127.890640	485	16/04/2010 6:36	18/04/2010 0:45	42.15
MUS030	ANSIR	-26.094320	127.834490	478	16/04/2010 5:35	18/04/2010 1:20	43.75
MUS031	Phoenix	-26.076167	127.784800	478	15/04/2010 6:00	16/04/2010 23:45	41.75
MUS032	Phoenix	-26.079017	127.731867	472	15/04/2010 5:30	17/04/2010 0:21	42.85
MUS033	ANSIR	-26.091940	127.680840	472	15/04/2010 4:01	17/04/2010 0:32	44.52
MUS034	ANSIR	-26.068080	127.616090	490	15/04/2010 5:37	17/04/2010 1:10	43.55
MUS035	Phoenix	-26.058417	127.551117	503	17/04/2010 3:00	18/04/2010 23:45	44.75
MUS036	Phoenix	-26.043317	127.509100	519	17/04/2010 4:00	19/04/2010 0:37	44.62
MUS037	ANSIR	-26.015860	127.465810	543	17/04/2010 2:46	18/04/2010 22:53	44.12
MUS038	ANSIR	-26.025000	127.416070	523	17/04/2010 3:39	18/04/2010 23:19	43.67
MUS039	Phoenix	-26.040067	127.367117	495	18/04/2010 5:30	19/04/2010 23:13	41.72
MUS040	Phoenix	-26.059817	127.320433	485	18/04/2010 4:00	19/04/2010 23:43	43.72
MUS041	ANSIR	-26.076700	127.269580	476	17/04/2010 5:14	18/04/2010 23:52	42.63
MUS042	ANSIR	-26.085680	127.216110	488	18/04/2010 3:54	19/04/2010 23:20	43.43
MUS043	ANSIR	-26.097070	127.161620	485	18/04/2010 5:59	20/04/2010 0:13	42.23
MUS044	ANSIR	-26.114660	127.119490	509	20/04/2010 1:21	22/04/2010 1:30	48.15
MUS044.5	Phoenix	-26.090650	127.101600	494	20/04/2010 2:00	21/04/2010 23:32	45.53
MUS045	Phoenix	-26.061217	127.086817	530	20/04/2010 4:00	22/04/2010 0:26	44.43
MUS045.5	Phoenix	-26.020017	127.080333	551	19/04/2010 8:00	21/04/2010 0:02	40.03
MUS046	Phoenix	-25.980017	127.073800	533	19/04/2010 6:00	21/04/2010 1:03	43.05
MUS047	ANSIR	-25.902700	127.035600	522	20/04/2010 6:08	22/04/2010 1:26	43.30
MUS048	ANSIR	-25.825640	127.017910	517	19/04/2010 7:00	21/04/2010 0:50	41.83
MUS048b	ANSIR	-25.789930	127.004740	509	19/04/2010 5:59	21/04/2010 2:12	44.22
MUS049	ANSIR	-25.756860	126.971520	500	19/04/2010 4:04	21/04/2010 1:21	45.28

where $\omega = 2\pi f$ is the angular frequency of the fields and μ is the magnetic permeability of the Earth. The ratio of the two fields is used to determine the impedance ($Z = E/H$), a measure of the opposition to the flow of alternating electric currents. As shown by Equation 1, apparent resistivity is related to the square of the impedance.

$$\rho = \frac{1}{\omega\mu}\left|\frac{E}{H}\right|^2 \qquad \text{Equation 1}$$

The MT impedance tensor contains four complex-valued transfer functions (Z_{xx}, etc.) between the various orthogonal components of the horizontal electric and magnetic fields (Equation 2). Each MT impedance term can be used to estimate an apparent resistivity, a volumetrically averaged resistivity over the penetration depth of the signals.

$$\begin{bmatrix} Z_{xx} & Z_{xy} \\ Z_{yx} & Z_{yy} \end{bmatrix}\begin{bmatrix} H_x \\ H_y \end{bmatrix} = \begin{bmatrix} E_x \\ E_y \end{bmatrix} \qquad \text{Equation 2}$$

If the Earth's electrical structure is 1D (i.e. the Earth consists of a horizontally layered structure and hence only varies in 1 direction), or 2D (varies in two directions) with the X-direction parallel to strike and perpendicular to Y, then $Z_{xx} = Z_{yy} = 0$. If the strike is known, the data can be rotated accordingly, in which case the non-zero Z_{xy} and Z_{yx} impedance can be used to determine apparent resistivity as a function of frequency using Equation 1, where ρ_{xy} uses E_x and H_y and ρ_{yx} uses E_y and H_x (Equation 3; Fig. 5). XY data are referred to as transverse electric (TE) mode, and YX as transverse magnetic (TM). In the TE mode, the electric field is parallel to strike and the magnetic field is perpendicular. In the TM mode, the magnetic field is parallel to strike and the electric field is perpendicular.

$$\rho_{xy} = \frac{1}{\omega\mu}\left|\frac{E_x}{H_y}\right|^2 \qquad \rho_{yx} = \frac{1}{\omega\mu}\left|\frac{E_y}{H_x}\right|^2 \qquad \text{Equation 3}$$

Also important is the phase difference (ϕ) between the two fields; $\phi = \arctan(E/H)$. The electric field always leads the magnetic field. If electrical property variations are 1D, there is a phase difference of 45°. In many situations, phases exceeding 45° correspond to geoelectric structures in which resistivity is decreasing with depth and phases of less than 45° correspond to resistivity increasing with depth. As with apparent resistivity, XY and YX phase responses can be determined (Equation 4; Fig.5).

$$\phi_{xy} = \arctan\left|\frac{E_x}{H_y}\right| \qquad \phi_{yx} = \arctan\left|\frac{E_y}{H_x}\right| \qquad \text{Equation 4}$$

Static corrections

MT data are prone to 'static shifts' due to heterogeneous electrical properties in the near surface at a scale smaller than the resolving capability of the MT data (Fig. 6). The result is a frequency-independent shift, i.e. the entire curve is involved, of the apparent resistivity data parallel to the apparent resistivity axis. The amount of shift is called the static shift factor (s). Failure to account for this will lead to incorrect estimation of resistivities, and the depths at which they occur, during data modelling.

Static shifts were estimated using the time-domain (TD) electromagnetic soundings. However, it was not possible to acquire useful TD data in areas where surface resistivity was very high and at approximately half of the sites it was not possible to use the measured TD data for static shift

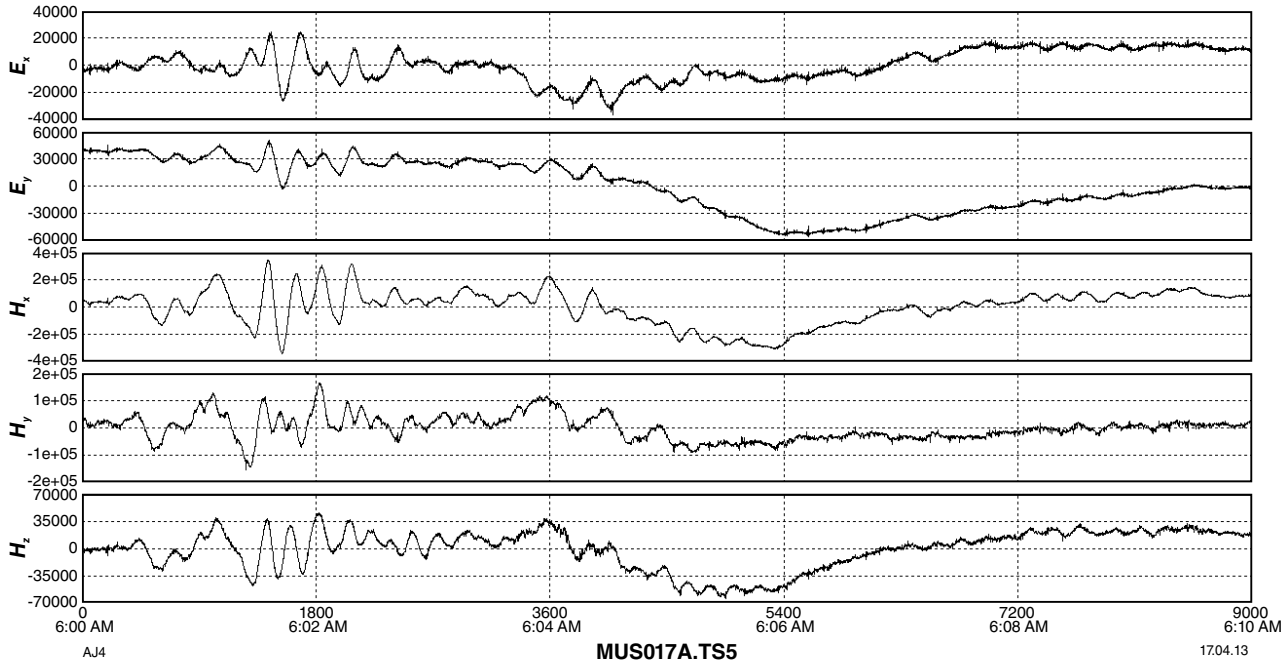

Figure 4. Example MT time series MUS017 (Phoenix equipment). Units are microvolts for electric (E) field data and nanoTesla for magnetic (H) field data.

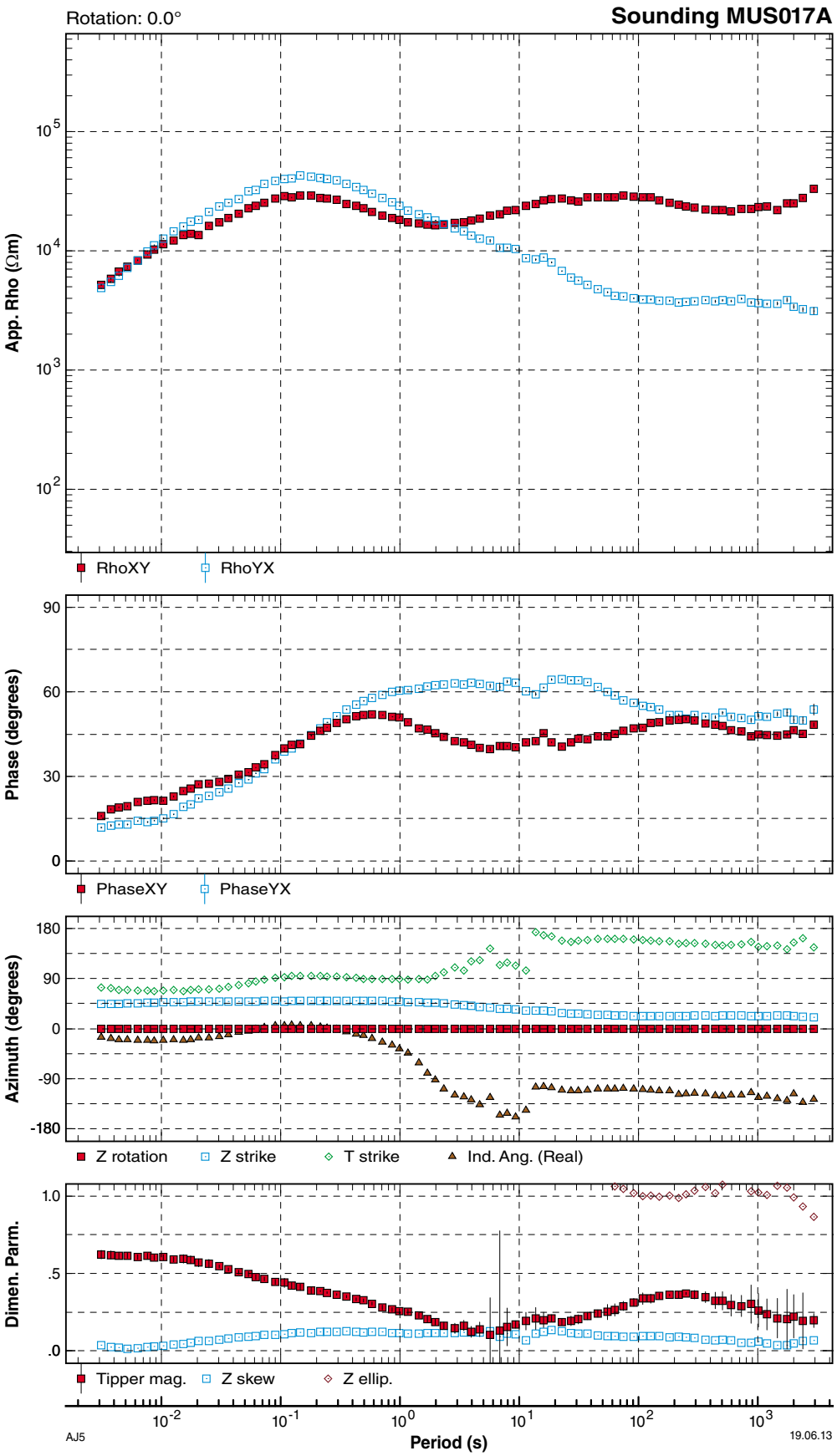

Figure 5. Example of MT sounding from the same station (MUS017) as in Figure 4. Red symbols show the transverse electric (TE) response and blue symbols show the transverse magnetic (TM) response. Note the increased errors as the data approach the longest periods (greatest depths).

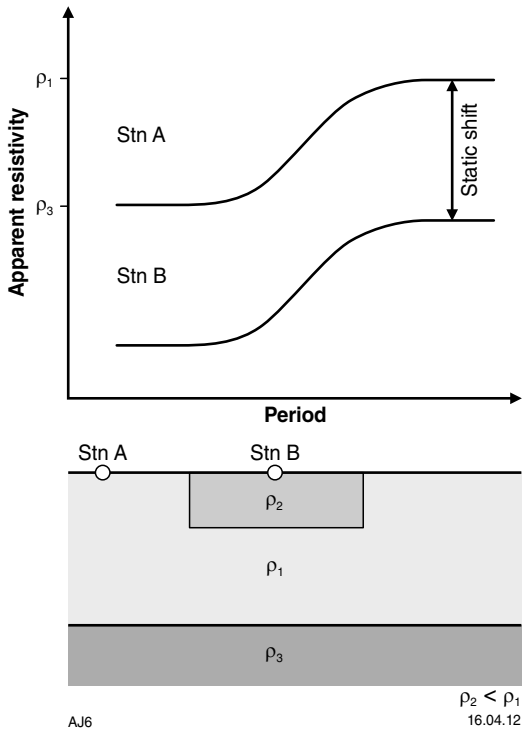

Figure 6. Schematic illustration of the static shift effect in MT data. Note lower apparent resistivity at station B due to shallow ρ_2.

corrections. Where useful data were recorded, these data were inverse modelled to derive a two- or three-layered 1D Earth model that is consistent with the observed TD data. This model was then used to forward model an MT response, which was compared with the observed MT data. The MT curves are translated so that they overlay the time-domain data. To achieve this with accuracy requires the time domain-derived and MT data curves to overlap. This was generally the case. The equivalent MT curves derived from the time-domain soundings are shown in Appendix 1. The static-shift factor dictates whether the apparent resistivity curves are moved up (s >1) or down (s <1). The average XY static shift factor was 2.20, and for the YX data, 2.78.

Dimensionality and geoelectric strike

Most MT modelling algorithms assume the area of interest is geoelectrically 1D or 2D. A 3D, i.e. varying in three directions, electrical structure requires greater computational power to model the data and the Earth models must be comparatively simple. In the 'normal' 2D modelling scenario the direction of geoelectric strike is assumed to be consistent; that is, there must not be any localized or off-profile geoelectrical property variations, and the strike direction must be known. The frequency-dependent variations in impedance are also used to determine electrical dimensionality and geoelectric strike direction of the subsurface.

The dimensionality of the MT data was assessed using the phase-tensor method of Caldwell et al. (2004). Unlike many other dimensionality estimation methods, this method analyses only the phase variations, because these are unaffected by galvanic distortion associated with near-surface changes in electrical conductivity and the method does not rely upon assumptions that the regional electrical structure is 1D or 2D.

The parameters used to characterize the phase tensor are minimum phase values and the skew angle (β). The angle α is a measure of the tensor's orientation relative to the coordinate system and the ellipticity is a measure of the ratio of the maximum (Φ_{max}) and minimum (Φ_{min}) phase values. The phase tensor is commonly represented as an ellipse (Fig. 7), with the long and short axes of the ellipse representing the maximum and minimum phase values, respectively. The orientation (α–β) of the major axis represents the direction of maximum current flow. A 1D subsurface will be represented by a circle. With the influence of two dimensionality, the ellipticity increases. A 3D subsurface results in a skewed ellipse with the main axis deflected by an angle β from the symmetry axis (dashed line in Fig. 7).

Plots of minimum phase and phase skew calculated from the Phoenix instrument recordings are shown in Figures 8 and 9, respectively. The minimum phase data are typical for crustal MT surveys, in that the data are quite heterogeneous for short periods (0.01 s) and become more coherent towards 10 s with the main orientation north–south. Similarly the minimum phase values become less scattered at longer periods. At periods above 100 s (lower crust – upper mantle depths), the ellipses are consistently oriented in a northwest–southeast direction, with some variability perhaps due to the influence of major domain boundaries. The phase skew data draws a similar picture.

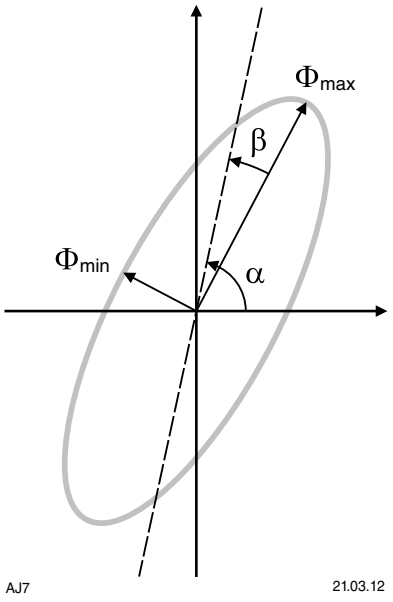

Figure 7. Graphical representation of the MT phase tensor illustrating parameters used to define the ellipse. From Caldwell et al. (2004)

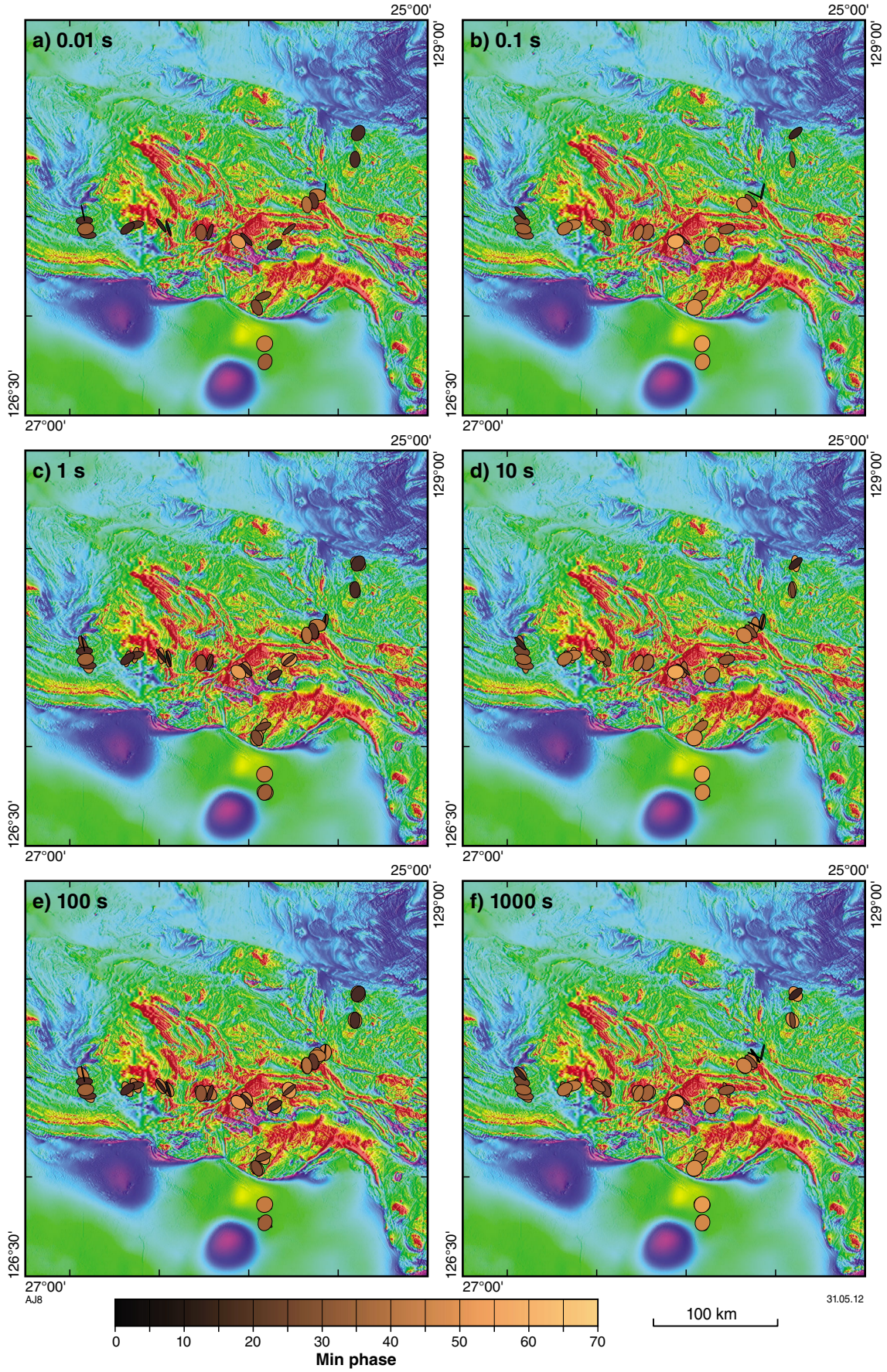

Figure 8. Minimum phase data from the stations recorded with Phoenix equipment for different periods

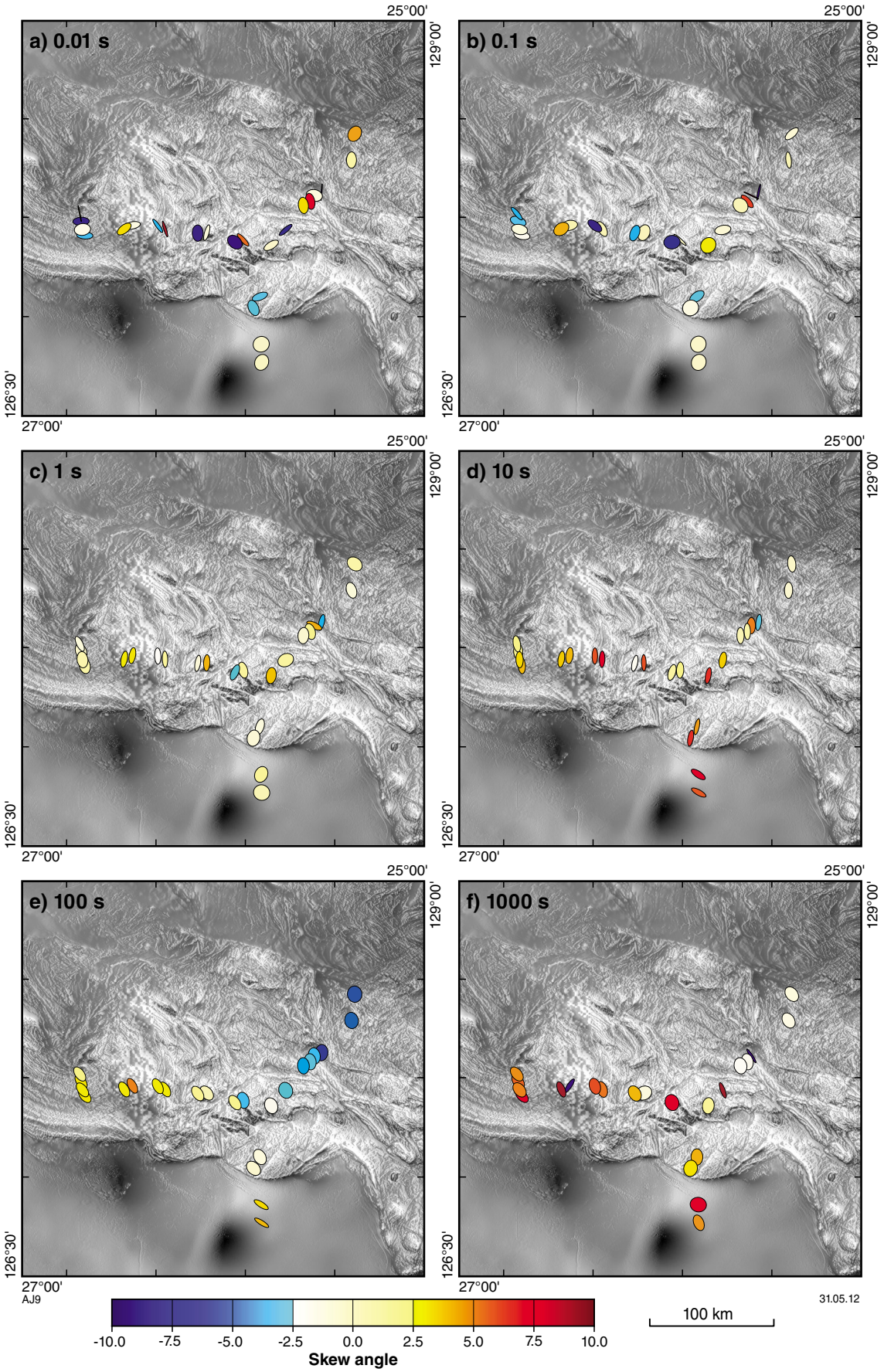

Figure 9. **Phase skew data from the stations recorded with Phoenix equipment for different periods**

For periods below 1 s the values are quite variable, representing the variable electrical properties in the area immediately the station. At 1 s, the skew is generally low across the whole survey area before increasing at 10 s. The higher skew at 10 s may be due to this period responding to depths where there is a boundary between two different strike directions, resulting in a 3D effect. For periods of 100 s the skew is still higher, but generally below 5° suggesting that the electrical strike is now dominated by the northwest–southeast electrical strike in the mantle. At 1000 s the signal-to-noise ratio is poor, resulting in a lack of coherent responses.

The 2D strike rose plots (Fig. 10a) are the strike angles from the seven invariants (Weaver et al., 2000). Together, these invariants define the 1D magnitude, dimensionality, and galvanic distortion effects (Groom and Bailey, 1989). The phase tensor azimuth (Fig. 10b) is the orientation of the phase-tensor ellipse. No preferred strike direction is observed below 0.1 s. For periods between 0.1 and 10 s the preferred direction is about 15° degrees north-northeast. At 10 to 100 s the dominant direction is about –10° (north-northwest). At the longest period the dominant direction is northwest–southeast.

Data modelling

Figures 11 and 12 show TM and TE mode pseudosections of apparent resistivity and phase for all data points not judged to be excessively noisy. Note that the data recorded by the Phoenix equipment (stations with red triangles) tend to extend to lower frequencies. Figures 13 and 14 comprise equivalent data after removal of data affected by 3D conductivity variations. Data with a skew value of greater than 5° or less than –5° were deemed to be 3D and removed from the inversion. A significant amount of data had to be excized prior to modelling, especially from the east–west line (compare Figures 12 and 14).

2D conductivity model

The data not significantly affected by 3D conductivity variations were modelled using the 2D non-linear conjugate gradient inversion algorithm of Rodi and Mackie (2001), as implemented in the Winglink software package (GEOSYSTEM SRL). This inverse-modelling method minimizes an objective function consisting of the data misfit and a measure of model roughness, with the user-specified trade-off parameter, τ, defining the balance between these terms. Both TE and TM modes and the Hz transfer function were modelled over the frequency range 500–0.001 Hz using a uniform-grid Laplacian operator and $\tau = 3$. Geoelectric strike was taken to be –20° for the east–west model and –10° for the north–south (see above). Error floors are listed in Table 3.

Due to the high near-surface resistivity affecting the time-domain data, many of the apparent resistivity curves had not been corrected for static shift. Visual inspection suggests that static shifts may be more prevalent along the east–west line and this is possibly the reason for slightly higher error floors on the apparent resistivity. When no static shift could be quantified, the shift is allowed to vary at relevant stations during the inversion.

The preferred 2D models, displayed as resistivity variations, for the two traverses are shown in the uppermost cross sections in Figures 15a and 16a. Note that the misfit between observed and calculated data corresponds to an RMS difference of 4.3291 and 5.385 for the north–south and east–west transects, respectively. To test the reliability of various features seen within resistivity cross sections produced by inverse modelling of MT data it is normal practice to replace features with anomalous resistivity with background values and then re-run the inversion algorithm to see if the feature reappears; i.e. this indicates whether it is required to fit the data.

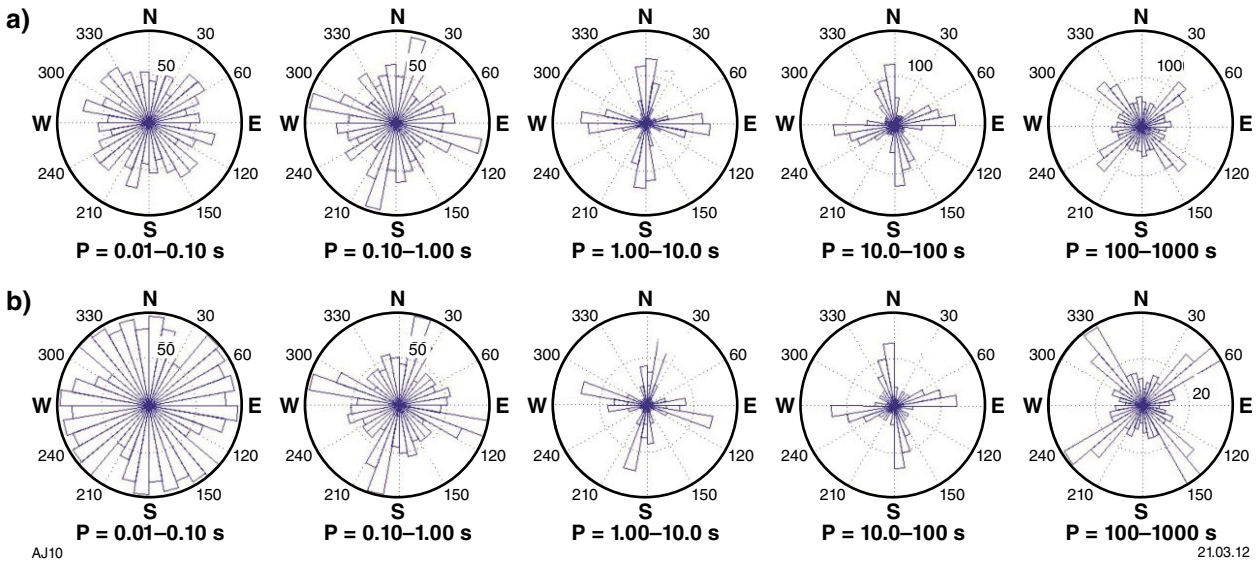

Figure 10. Rose diagrams of phase tensor ellipse orientations: a) strike angles from the seven invariants; b) phase tensor azimuth

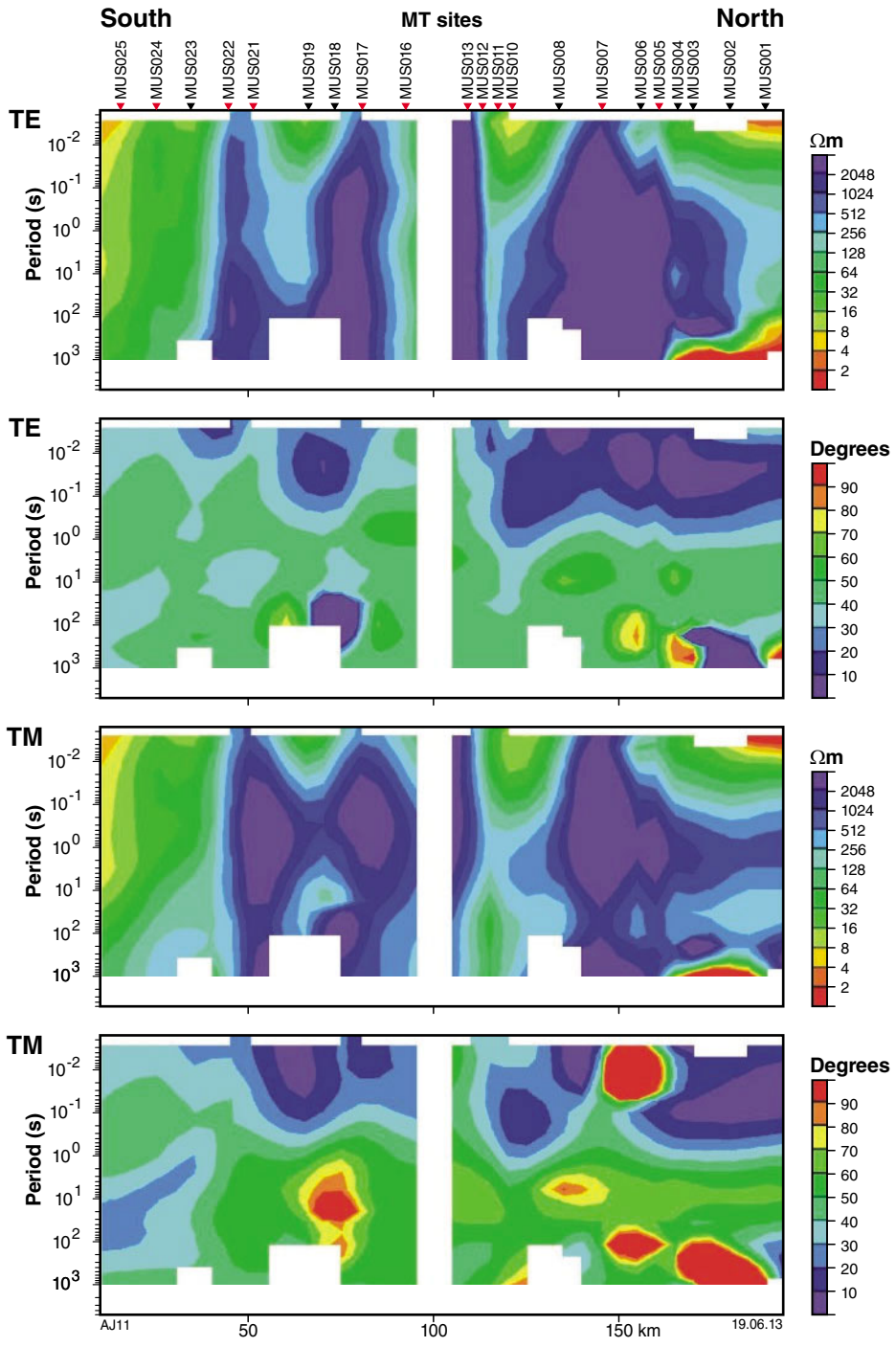

Figure 11. Pseudosections comprising data considered to have an acceptable signal-to-noise level, N–S transect

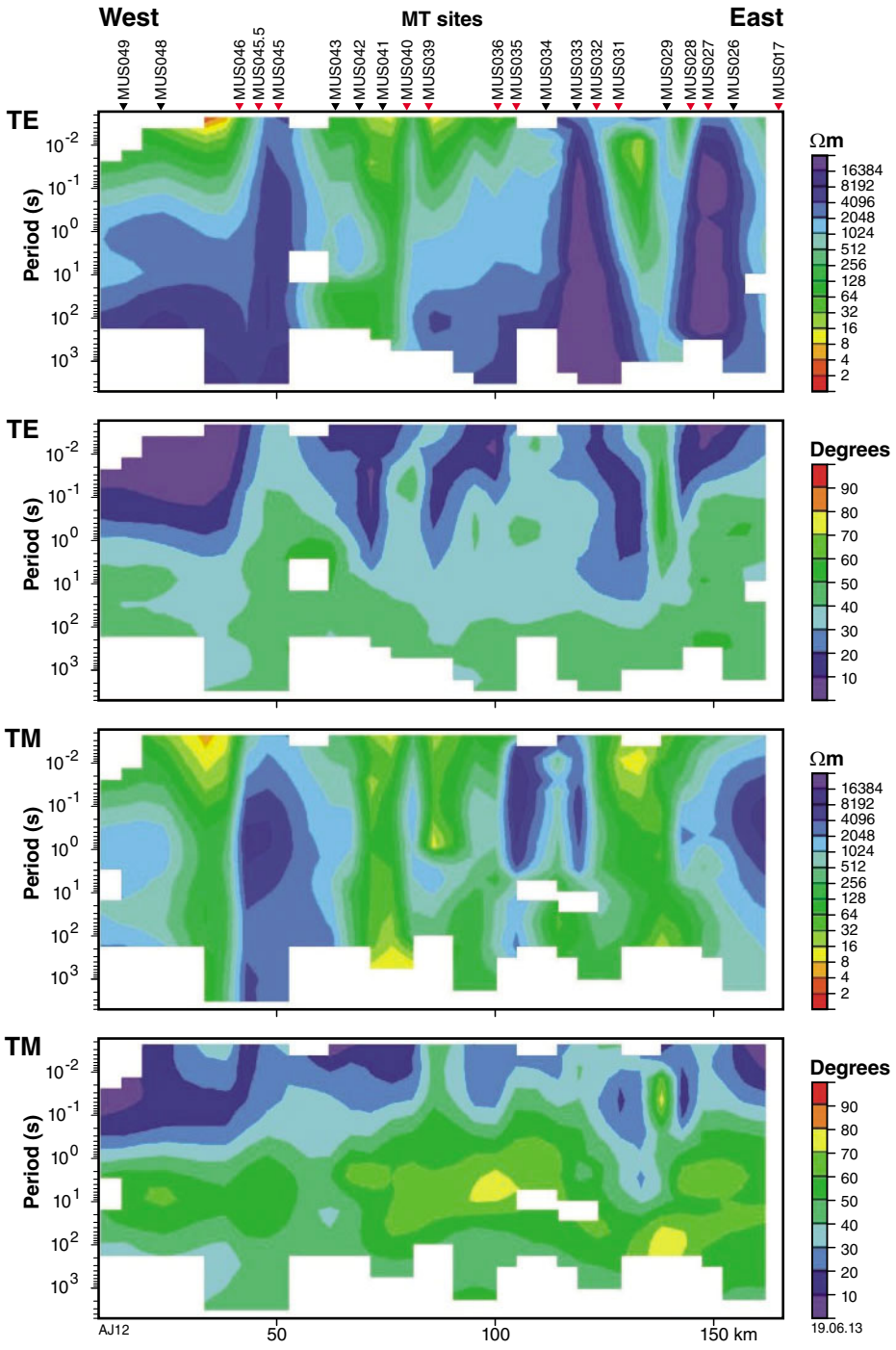

Figure 12. Pseudosections comprising data considered to have an acceptable signal-to-noise level, E–W transect

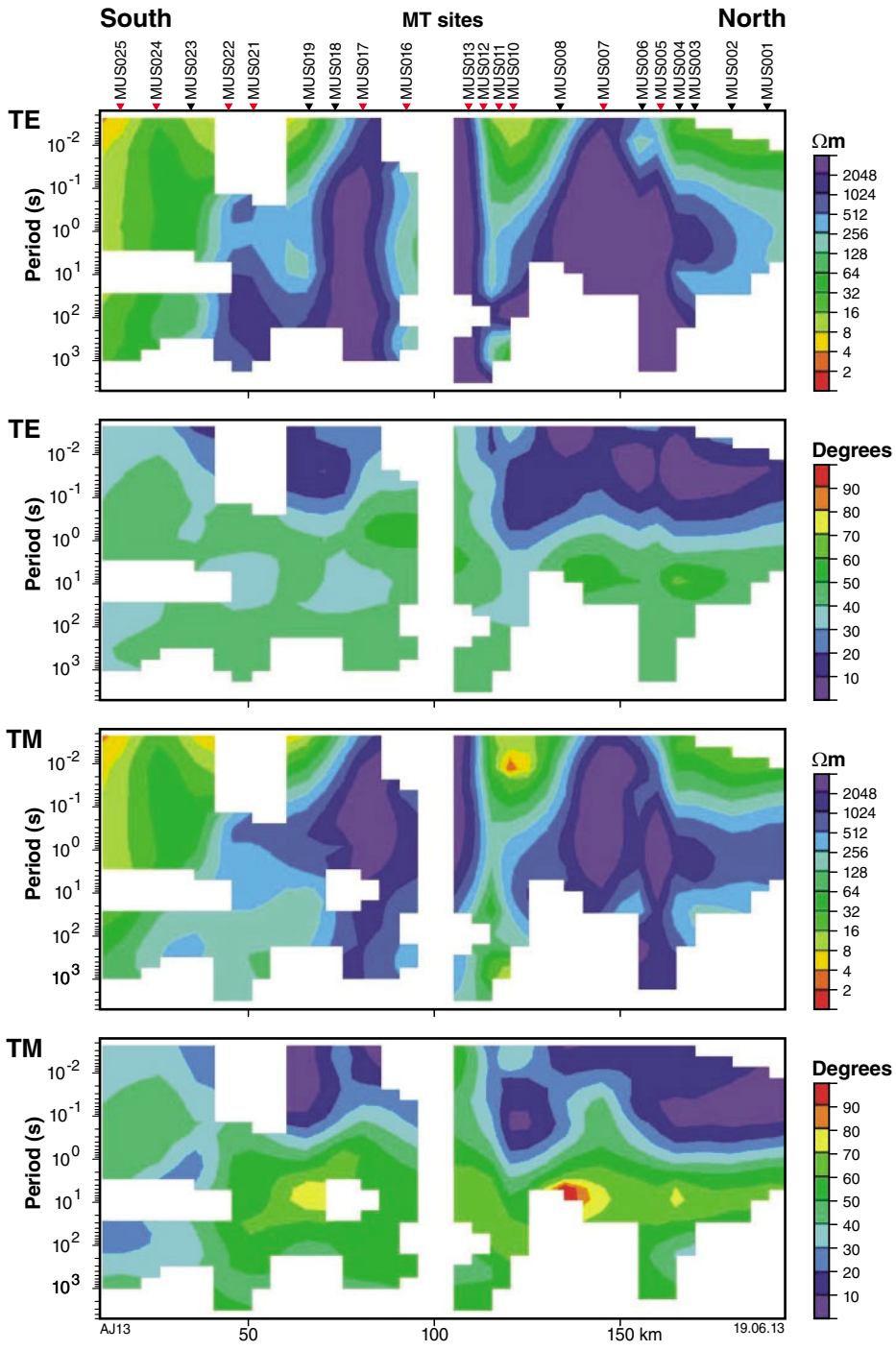

Figure 13. Pseudosections comprising data considered to have an acceptable signal-to-noise level and no significant 3D influence, N–S transect. These data were modelled to create the resistivity cross section in Figure 17.

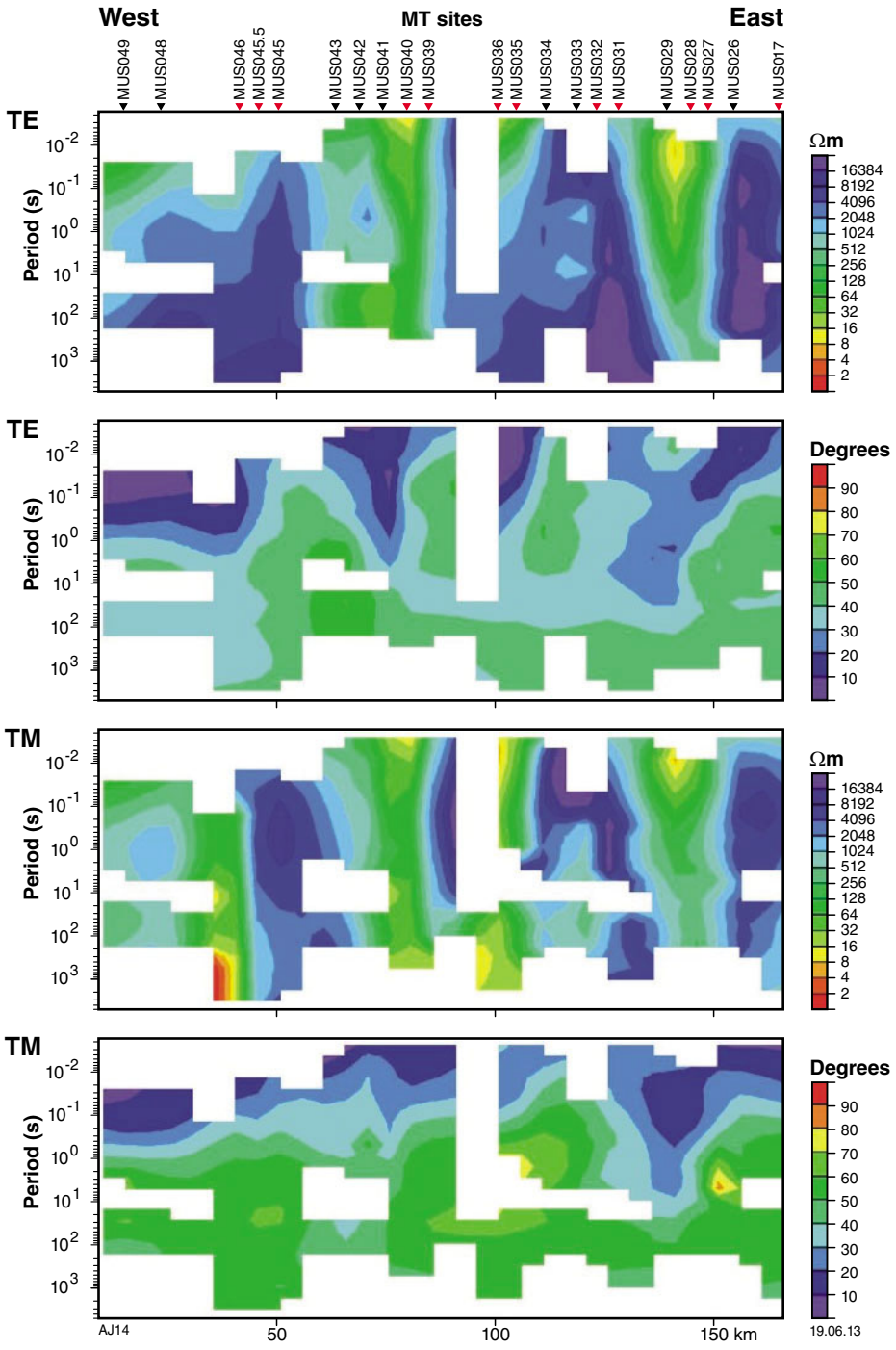

Figure 14. Pseudosections comprising data considered to have an acceptable signal to noise level and no significant 3D influence, E–W transect. These data were modelled to create the resistivity cross section in Figure 18.

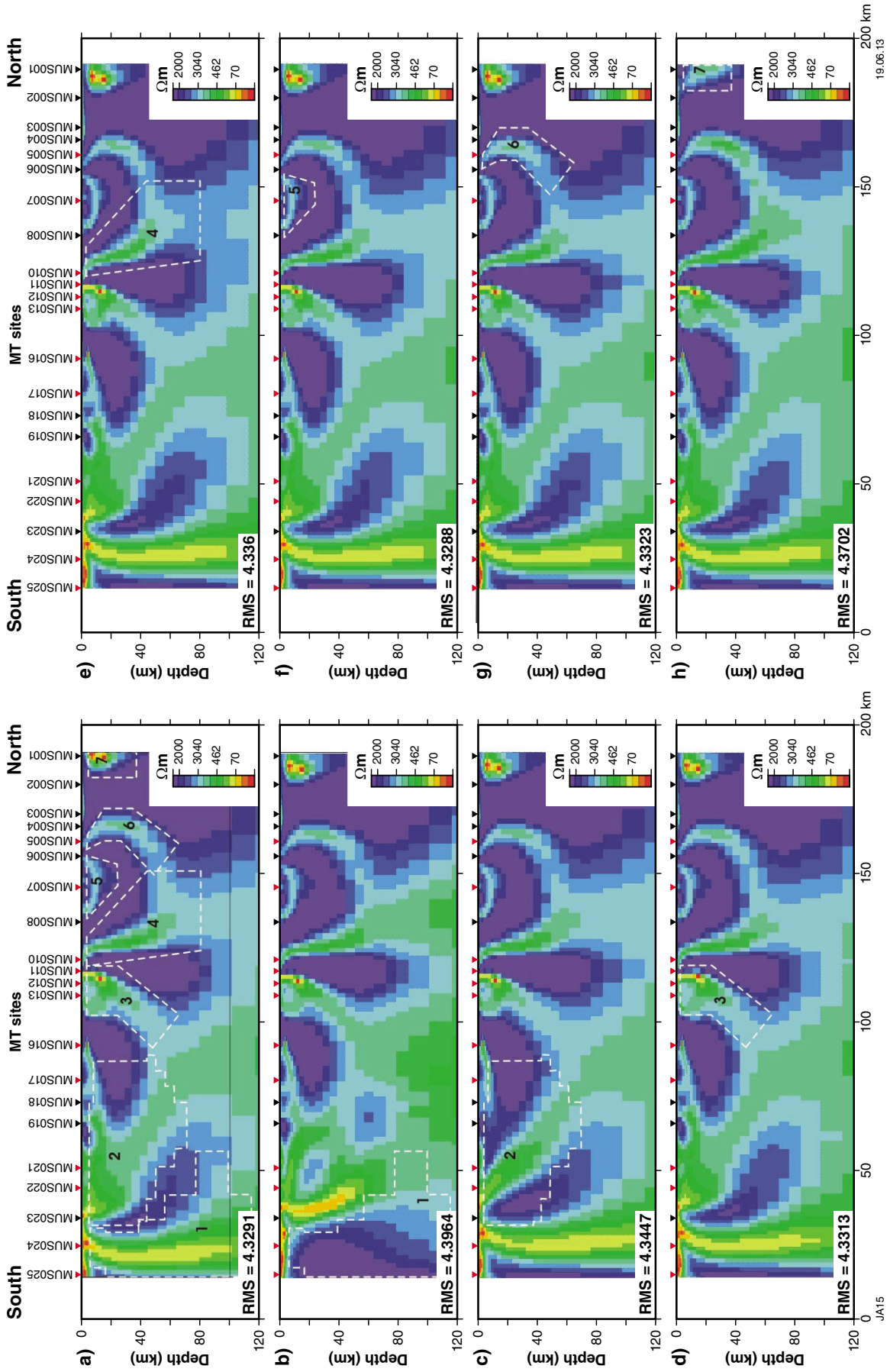

Figure 15. Assessment of the reliability of features with anomalous electrical properties in the preferred resistivity cross section (15a) for the N–S transect. Each of the numbered features is 'removed' in turn and the data re-modelled to see if they reappear; this provides evidence of the feature required to correctly model the observed data. Vertical exaggeration in this diagram is 0.5. See text for explanation of specific cross sections.

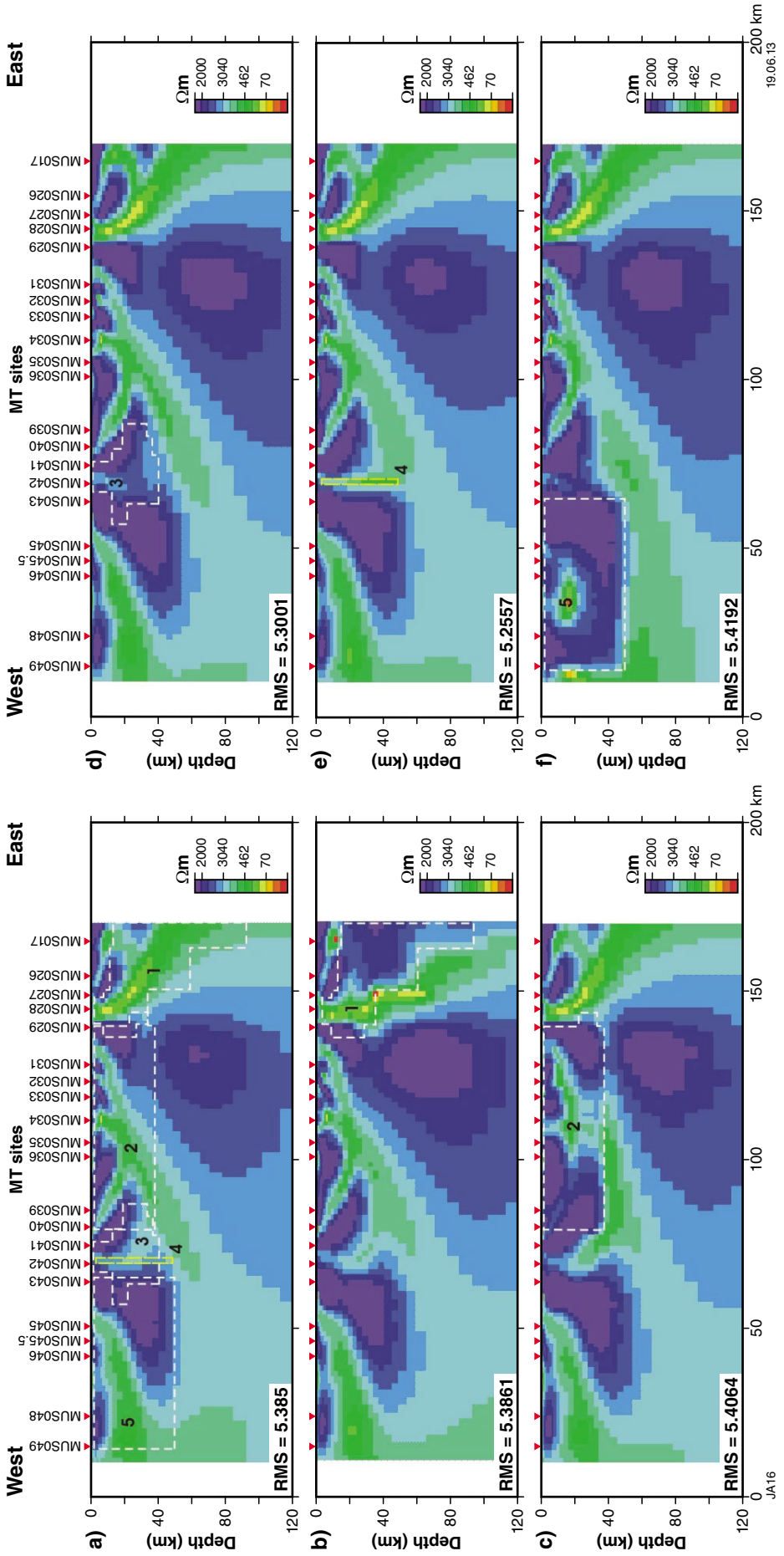

Figure 16. Assessment of the reliability of features with anomalous electrical properties in the preferred resistivity cross section (16a) for the E–W transect. Each of the numbered features is 'removed' in turn and the data re-modelled to see if they reappear; this provides evidence of the feature required to correctly model the observed data. Vertical exaggeration in this diagram is 0.5. See text for explanation of specific cross sections.

Table 3. Error floors used in 2D modelling

Error Floors		*Apparent resistivity (Ω.m)*	*Phase (°)*
N–S line	TE	15	5
	TM	10	2.5
E–W line	TE	20	5
	TM	12.5	2.5

The two resistivity cross-sections were systematically analysed (feature tested) to determine the reliability of the various higher or lower resistivity zones that comprise the section. This was achieved by, for example, replacing that part of the cross section which comprises a low-resistivity zone with higher resistivity material. The inverse modelling was then repeated to determine whether the excized feature reappears. The similarity between the resulting model and those comprising Figures 15a and 16a is taken as a measure of how well constrained the feature's presence/geometry is in the preferred conductivity cross sections. For example, the lower-resistivity area outlined in white and labelled '1' in Figure 15a is replaced by higher resistivity material. Figure 15b shows the model after the inversion is restarted using the modified resistivity model as input. In this case a conductive feature with similar geometry reappears but its dip is shown to be poorly constrained. In contrast, features '2' and '3' are very similar in the 're-run' model, as occurs in most cases. In most cases of feature testing, the resulting conductivity variation is effectively identical to the original model. An exception is feature '1' on the north–south transect (Fig. 15a and b) where the near-vertical conductive zone in the preferred model has a significantly different location and geometry in the re-run dataset (as shown below, the new geometry is more consistent with the results of the gravity and magnetic modelling). Another exception is feature '5' on the east–west profile where a shallowly dipping conductive feature reappears as a localized zone of greater conductivity (Fig. 16f).

Geological implications of the MT data

Figures 17 and 18 show the preferred conductivity cross sections in relation to the surface geology and the extent of major positive gravity features. A detailed interpretation of the MT data to crustal depths in conjunction with the results of the gravity and magnetic modelling is described later. Both resistivity cross sections are notable for the very high resistivities of the lithosphere. Figure 19 shows the range of resistivities as presented by Jones (1999). There is no obvious distinction between upper and lower crust in the Musgrave Province data, and the observed resistivities are within the range of upper-crustal values seen elsewhere in the world. The mantle is of unusually

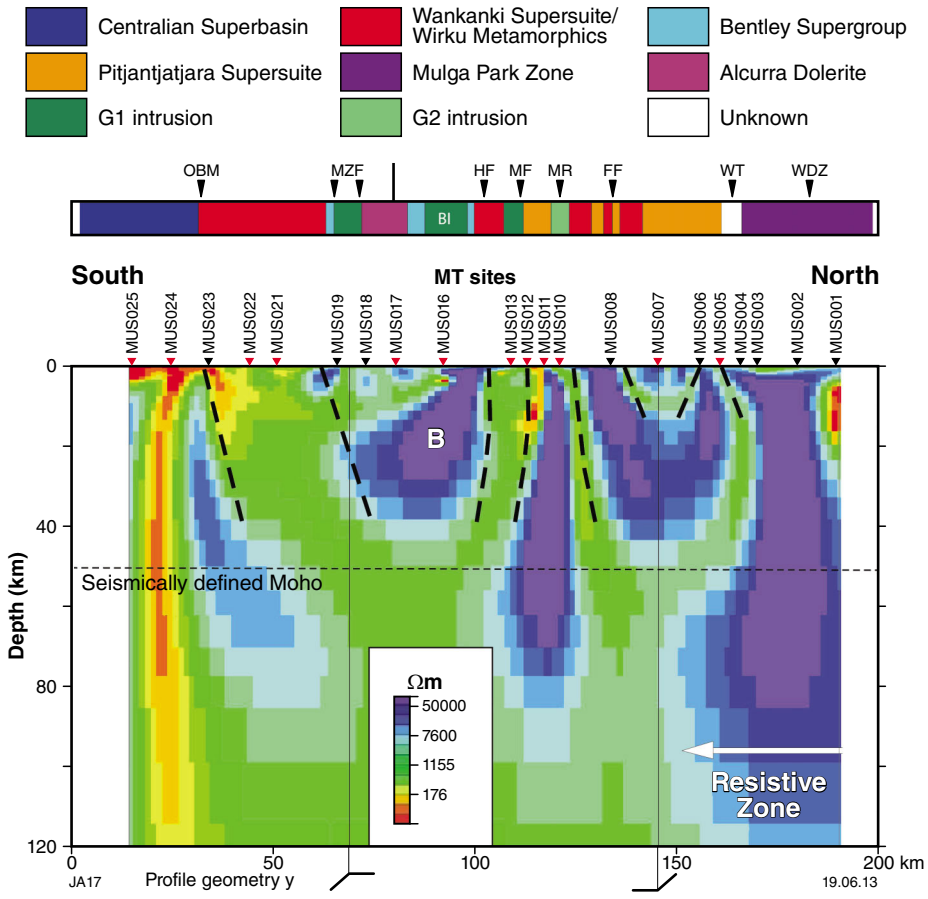

Figure 17. Geological interpretation of resistivity cross section from the N–S transect. Labelled features are discussed in the text. See Figure 2 for fault abbreviations

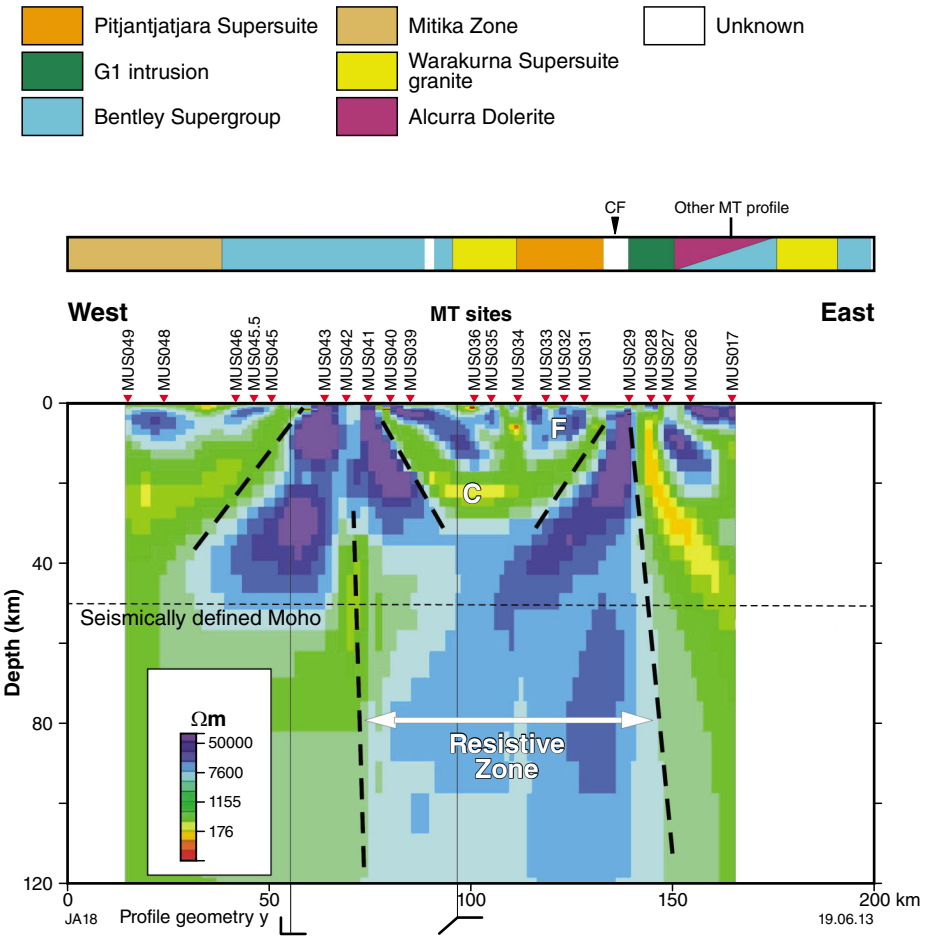

Figure 18. Geological interpretation of resistivity cross section from the E–W transect. Labelled features are discussed in the text. See Figure 2 for fault abbreviations

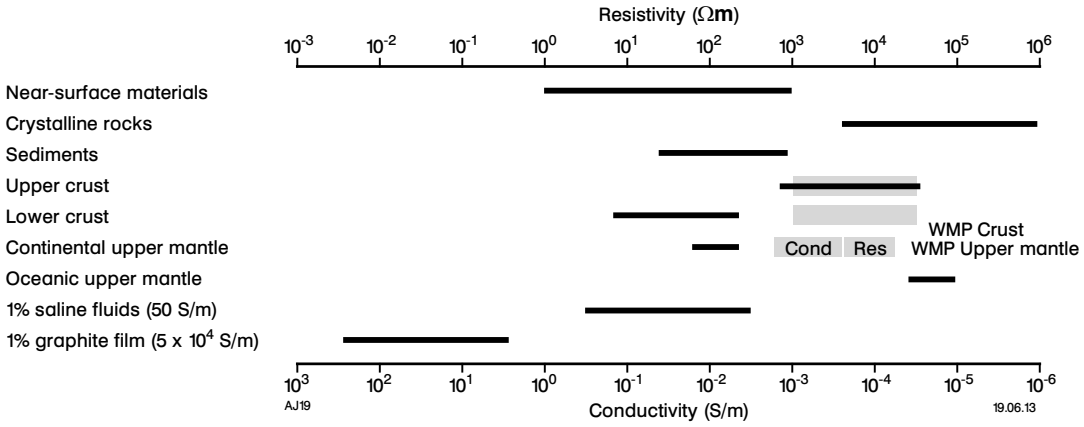

Figure 19. Resistivity ranges of selected geological entities and materials. Re-drawn from Jones (1999) with additions

high resistivity, even accounting for the possibility that Jones' (1999) range may not extend to sufficiently high values.

Three other MT surveys have studied the Musgrave Province. Two of these are almost coincident, and cross the easternmost Musgrave Province (Korsch and Kositcin, 2010; Selway et al., 2011). Here, to depths of about 10 km, resistivities were between about 50 and 5000 Ω.m. The underlying region had high resistivities of >10 000 to several hundred thousand Ω.m (Korsch and Kositcin, 2010; Selway et al., 2011). This structure continues southwards beneath the northern part of the Paleoprotoerozoic Nawa Domain (part of the Gawler Craton). A third profile across the Amadeus Basin and the underlying Warumpi Province just crosses into the Musgrave Province from the north. The Warumpi Province has similar aeromagnetic character to the Musgrave Province, and may represent a continuation of the Musgrave Province (Aitken and Betts, 2008). This model suggests that the Warumpi Province lithosphere is also resistive, although to a lesser degree, with resistivities between 1000 and 4000 Ω.m (Selway et al., 2009). Thus, the results from these earlier surveys confirm the highly resistive nature of the west Musgrave Province lithosphere.

Selway et al. (2011) speculated that the Musgrave Province involves a Gawler Craton-like basement upon which younger rocks were deposited prior to Grenville-age orogenesis (Mount West and/or Musgrave Orogeny). However, the cause of the high resistivities is difficult to determine because of the poor understanding of controls on electrical properties in the deep crust and mantle. The high resistivity is indicative of a lack of conductive material, which in this context indicates a lack of conductive mineral species. The chemistry, especially iron content, of mineral species such as pyroxene and olivine is thought to affect their electrical properties. Ultimately, the high resistivities in the mantle may reflect a high degree of melting associated with the voluminous magmatism in the west Musgrave Province.

As is commonly seen in MT data in basement terrains, and best developed on the north–south traverse, there are more conductive areas that comprise narrow linear zones that are probably due to the presence of more conductive mineral species in major fault zones. Resistive zones with similar geometries could also be associated with such structures because, if there is silicification of the crust, then resistivities may be very high in shear zones (Jones and Garcia, 2004). The maximum depths of such features are poorly constrained but most seem to terminate at roughly the seismically defined Moho depth. These features are useful indicators of deep-penetrating fault zones, which are important features in the prospectivity analyses described by Joly et al. (2013), due to the likelihood of their control on the movement of metal-bearing fluids.

The positive gravity features crossed by both MT traverses are associated with contrasting crustal resistivity characteristics. On the east–west profile, the source of the gravity anomaly is the G1 Jameson intrusion (see below) and there is a conductive zone 'C' (Fig. 18), which, according to the gravity and magnetic modelling, lies below the base of the intrusion. One possible interpretation of this zone of greater conductivity is that it is associated with an accumulation of conductive mineral species at the base of the intrusion, although the presence of the Kunmarnara Group is also a potential source of higher conductivity. A geological scenario similar to the former was identified in an MT survey in Alaska (Pellerin et al., 2003).

The most interesting deep-seated feature in the MT data is the one of more resistive mantle on the east–west cross section between approximately 75 and 150 km (Fig. 18). The western limit of the zone does not coincide with any known feature in the surface geology, but the eastern margin coincides with the Cavenagh Fault. Resistive mantle occurs at the northern end of the north–south profile and its southern extent coincides with the boundary between the Walpa Pulka and Mulga Park Zones at the surface. If the two zones are continuous, it implies there is a north-northeasterly trending resistive zone in the mantle. The contrast in mantle electrical characteristics may be indicative of the juxtaposition of different lithospheric blocks, the boundaries between which are considered as the most prospective areas for some kinds of mineral deposits (Begg et al., 2010), notably magmatic nickel – sulfide deposits such as occur in the west Musgrave Province.

Density and magnetic susceptibility measurements

For the purpose of constraining properties for gravity and magnetic modelling, measurements of magnetic susceptibility and specific gravity data were made on 666 hand specimens. These specimens were collected throughout the west Musgrave Province, and represent most of the major geological units. Specimens were selected to provide the most representative database of the surface rocks possible, given the available material. However, it must be noted that the distribution of outcrop may introduce spatial biases into the dataset, and may also lead to preferential sampling of erosion-resistant units. The use of specimens from outcrop also introduces the possibility that weathering may influence the results. The data were primarily collected to provide constraints on the petrophysical properties of units during geophysical modelling (potential fields), but may also provide additional insight into other aspects of the rocks, such as oxidation states related to hydrothermal alteration.

Methods

Magnetic susceptibility measurements were made with a GMS-2 magnetic susceptibility meter, which has a sensitivity of 1 x 10^{-5} SI units. For each specimen, several measurements were made, taking care to sample different faces of the specimen, and different orientations. The arithmetic mean of these individual measurements is considered indicative of the overall magnetic susceptibility of the specimen.

Specific gravity was determined using the relation between the weight of the specimen in air (dry weight), and the

weight of the specimen suspended in water (wet weight) (Equation 5). Each specimen was weighed on a benchtop balance to determine the dry weight, and wet weights were established by suspending the specimen in water using a simple apparatus. Care was taken to ensure that the volume of the apparatus immersed as a result of the addition of the specimen was minimal. Most specimens were crystalline metamorphic or igneous rocks with low porosity, so it was deemed unnecessary to establish the difference between a water-saturated specimen and an unsaturated specimen. The scales used were precise to 0.25 g, resulting in measurement errors (Equation 6) of up to 0.1 g/cm^3, although for most samples measurement error is below 0.01 g/cm^3 (Fig. 20). This measurement error is primarily related to the mass of the specimen, although dense rocks have greater error than less dense rocks due to the smaller difference between wet and dry weights.

$$SG = W_D/(W_D - W_W) \qquad \text{Equation 5}$$

$$E = \left| SG * \sqrt{\left(\frac{P}{W_D}\right)^2 + \left(\frac{E_1}{W_D - W_W}\right)^2} \right| \qquad \text{Equation 6}$$

where $E_1 = \sqrt{P^2 + P^2}$

E = measurement error, SG = specific gravity, W_D = dry weight, W_W = wet weight, P = balance precision.

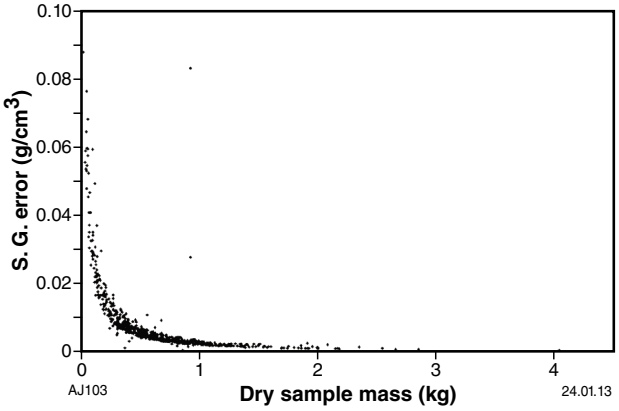

Figure 20. Specific gravity error plotted against dry sample mass. Most samples show error below 0.01 g/cm^3. Measurement error is principally dependent on sample mass, although dense samples show greater error, due to the smaller difference between wet and dry weights (see Equation 5).

Results and analysis

For analysis, the susceptibility and specific gravity data were divided into relevant lithological groups and statistical analysis was performed on the resulting populations. As well as documenting the statistical properties of these datasets as a whole, populations were modelled to detect sub-populations and to provide a better description of the petrophysical properties. For specific gravity, we assumed a normal distribution, and considered unimodal and bimodal populations. For magnetic susceptibility, we considered normal and log-normal (natural logarithm) distributions, with unimodal and bimodal populations. Where bimodal populations were modelled, each sample was assigned to one population or the other by applying a cutoff value, below which the sample is in the lower population, and above which the sample is in the higher population. The cutoff value was located either at the most prominent discontinuity in the overall population or, if data are nearly continuous, at the centre of the region where property values increase most rapidly. This means that the overlap of the lower and higher populations is not modelled perfectly. However, this method preserves the data-derived nature of the statistical models. Degree-of-fit was assessed by comparison of predicted distribution with observed frequency histograms (Fig. 21), both visually and by generating the root-mean-square (RMS) misfit. In constructing frequency histograms, bin sizes remained constant to allow easy comparison of different datasets. Specific gravity was divided into 0.05 g/cm^3 bins, typically ranging from 2.40 to 3.40 g/cm^3 although for some lithologies, extra bins were added either to the low or to the high end of the spectrum to accommodate significant populations outside of these limits. Magnetic susceptibility was analysed using a natural logarithmic scale, with 20 bins ranging from 0.5 (1.65 x 10^{-5} SI units) up to 10 (22 000 x 10^{-5} SI units). Population sizes for the main units are sufficiently high to permit robust analysis. However, some of the lesser units may be insufficiently sampled for a robust assessment of bimodality, and also for their fit to the various statistical laws used in modelling.

Wankanki Supersuite and Wirku Metamorphics

The oldest rocks widespread in the Musgrave Province are the c. 1345–1290 Ma granitic gneiss of the Wankanki Supersuite and paragneisses of the Wirku Metamorphics.

The specific-gravity data for the Wankanki Supersuite rocks are best fitted by a weakly bimodal distribution with a cutoff at 2.80 g/cm^3. This distribution yields a lower population (n = 31) with a mean* of 2.67 ± 0.07 g/cm^3 and a higher population (n = 7) at 3.00 ± 0.09 g/cm^3. Overall RMS misfit is 0.8, whereas a unimodal distribution yields a misfit of 1.75. The two populations do not correlate with the unit codes of the specimens, suggesting intra-unit variations. This distribution can be seen to fit the data well (Figs 21 and 22). The susceptibility data for the Wankanki Supersuite are best fitted by a unimodal log-normal distribution, with a log-susceptibility mean of 6.61 ± 1.30 (Fig. 22). Bimodal distributions produced a poor fit to the data, as did a normal distribution. Pyroxene-bearing units tend to produce the highest susceptibility values.

* All uncertainties in mean specific gravity and susceptibility values are at 1σ level

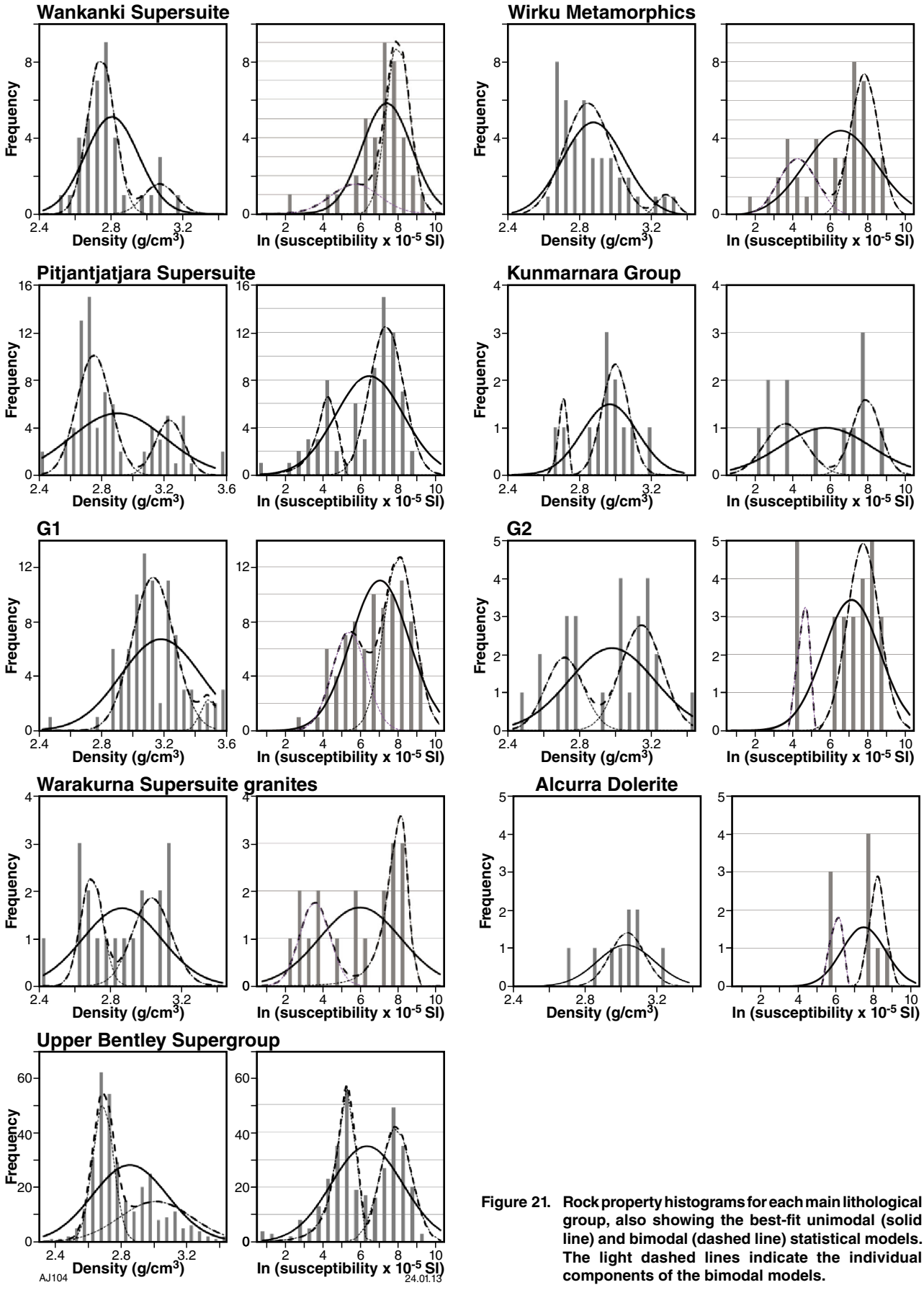

Figure 21. Rock property histograms for each main lithological group, also showing the best-fit unimodal (solid line) and bimodal (dashed line) statistical models. The light dashed lines indicate the individual components of the bimodal models.

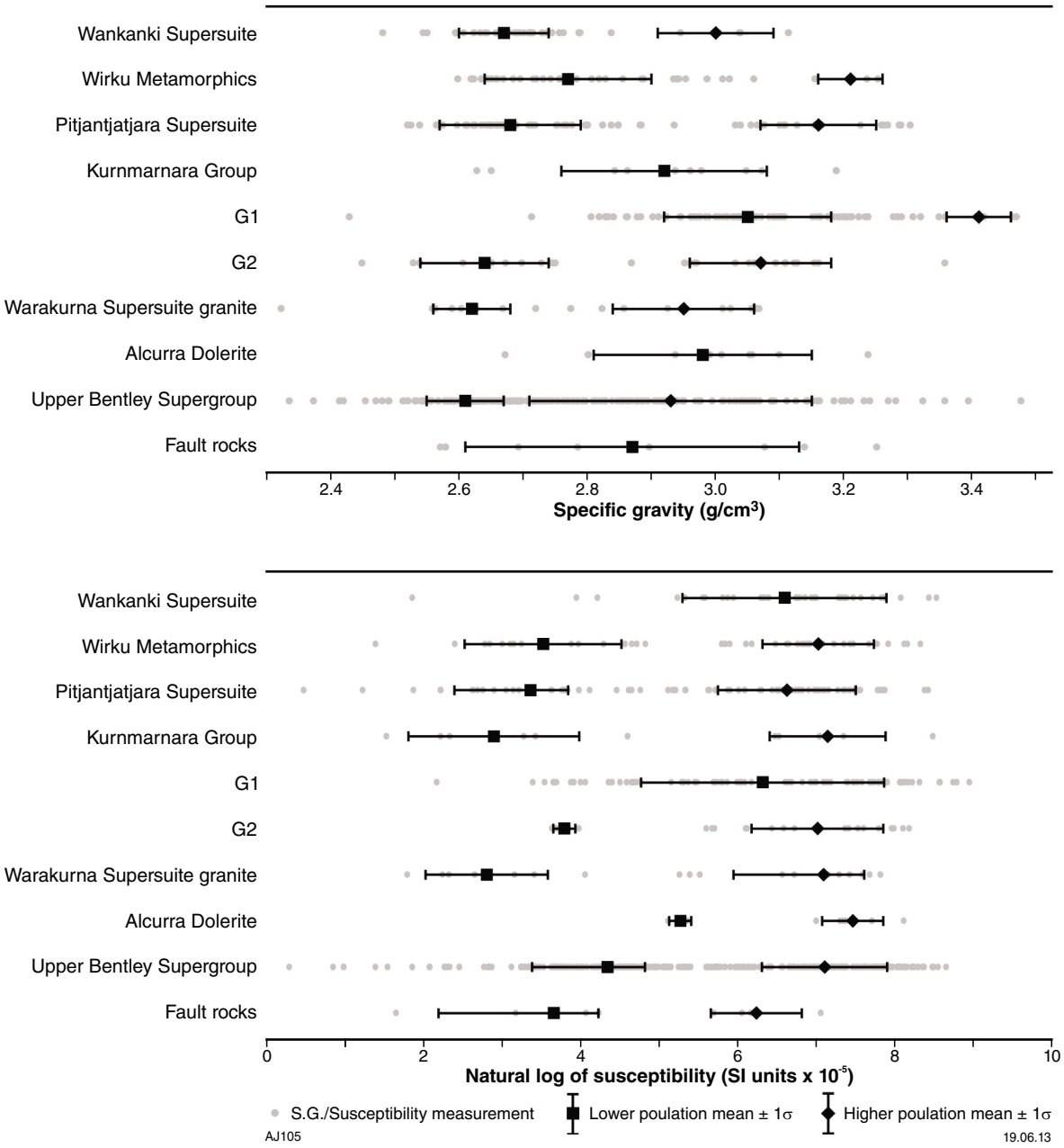

Figure 22. Plot showing the distributions of specific gravity and magnetic susceptibility for all rock types for easy comparison.

Specific gravity data for the Wirku Metamorphics are best fit by a very weakly bimodal distribution with a cutoff at 3.06 g/cm^3. This distribution yields a lower population (n = 39) with a mean of 2.77 ± 0.013 g/cm^3 and a higher population (n = 3) at 3.21 ± 0.005 g/cm^3. Overall RMS misfit is 1.54, whereas a unimodal distribution including all samples yields a misfit of 1.63. Visually, these distributions can be seen to fit the data reasonably well (Fig. 21) except for a positive skew to the data. There is no clear correlation between specific gravity and unit code. The susceptibility data for the Wirku Metamorphics are best fitted by a bimodal log-normal distribution, with a cutoff at 128 x 10^{-5} SI units. A log-susceptibility mean of 3.53 ± 1.00 is derived for the lower population (n = 15), and a log-susceptibility mean of 7.04 ± 0.71 is derived for the higher population (n = 27) (Figs 21 and 22). This distribution produced a RMS misfit of 1.26, as compared to 1.78 for a unimodal log-normal distribution and 2.21 for a unimodal normal distribution. Visually, the fit is good, especially for the higher population, although the lower population exhibits negative skew. This negative skew may be explained by a normal distribution within the lower population, although attempts to model this generated higher misfit (1.45) and strong positive skew. Comparison with the unit codes indicates that the coarser-grained units tend to have higher magnetic susceptibility.

Pitjantjatjara Supersuite

This unit represents the widespread granitic magmatism of the Musgrave Orogeny, and is found as discrete small intrusions or dykes, or larger composite intrusions, and forms the apparent basement in some regions. On the basis of geochemistry and field relationships, this supersuite can be separated into the early Pitjantjatjara Supersuite and the late Pitjantjatjara Supersuite, although there is significant age overlap between the populations (Smithies et al., 2009a).

Specific-gravity data for Pitjantjatjara Supersuite rocks show a well-spread and distinctly bimodal distribution. A cutoff at 2.90 g/cm^3, omitting both positive and negative outliers, yields a lower population (n = 55) with a mean of 2.68 ± 0.011 g/cm^3, and a higher population (n = 21) at 3.16 ± 0.009 g/cm^3. Overall RMS misfit is 2.29, as compared to a RMS misfit of 3.60 for a unimodal distribution (also omitting outliers). Visually, this distribution can be seen to fit the data reasonably well (Fig. 21). Dividing these rocks into early and late Pitjantjatjara Supersuite shows that each displays very similar characteristics to the overall dataset. In each, a strongly bimodal distribution is evident, comprising a dominant lower specific gravity population at 2.68 – 2.70 g/cm^3 and a higher specific gravity population centred at 3.15 g/cm^3. The early Pitjantjatjara Supersuite samples have more variability in specific gravity compared to the late Pitjantjatjara Supersuite samples.

Susceptibility data for Pitjantjatjara Supersuite rocks indicate that a bimodal distribution exists, with an interpreted cutoff at 75 x 10^{-5} SI units. Although log-normal distributions for each population provide a reasonable fit (RMS = 1.63), the best-fit model is that for which the lower population has a normal distribution, and the higher population has a log-normal distribution (RMS misfit = 1.53). In this model, the lower population (n = 19) has a mean of 29 ± 18 x 10^{-5} SI units, and the higher population (n = 56) has a log susceptibility mean of 6.64 ± 0.88 (Figs 21 and 22). Unimodal distributions, and a bimodal distribution with two normal distributions, provide a poor fit to the data (RMS >3). As with specific gravity, the early and late Pitjantjatjara Supersuite have similar characteristics, although the boundary between populations is higher in the late Pitjantjatjara Supersuite (150 x 10^{-5} SI units) than in the early Pitjantjatjara Supersuite (50 x 10^{-5} SI units), and the early Pitjantjatjara Supersuite have greater bimodality than the late Pitjantjatjara Supersuite.

These data show there is no petrophysical difference between early and late Pitjantjatjara Supersuite rocks, although the former are perhaps more variable for specific gravity and the latter more variable for susceptibility. The higher and lower populations are interpreted to dominantly reflect significant intra-unit variation. However, there is a clear link between deformation and petrophysics, in that mylonitized and strongly foliated rocks typically have lower density and lower susceptibility than their undeformed equivalents. Nonfoliated pyroxene-bearing granites are a significant component of the higher-susceptibility populations.

Kunmarnara Group

This unit is the oldest component of the supracrustal Bentley Supergroup, and was deposited onto the basement rocks prior to the emplacement of the Giles Suite intrusions. It is dominated by amygdaloidal basalts and is observed across a wide area.

Specific-gravity data for these rocks indicate an almost unimodal distribution. A unimodal normal distribution including all samples yields a mean of 2.92 ± 0.16, and generates a misfit of 0.53. This model includes two low outliers at 2.63 – 2.65 g/cm^3 and a lone high outlier at 3.19 g/cm^3 (Fig. 21). The main population (n = 9) has a mean of 2.95 ± 0.08 g/cm^3, and has a near-symmetrical distribution. RMS misfit for a bimodal model including this population and the lower outliers is 0.45. The low outliers relate to specimens of granophyre and quartz-pebble conglomerate, whereas the main population is composed of basalts and meta-basalts. The high outlier is a specimen that has been metamorphosed to amphibolite facies.

Susceptibility data show quite a lot of scatter due to the limited sample size. However, they indicate a likely bimodal population with an interpreted cutoff at 100 x 10^{-5} SI units. This is best fitted by log-normal populations with log-susceptibility means of 2.90 ± 1.09 (n = 6) and 7.16 ± 0.74 (n = 6) (Figs 21 and 22), which yield an RMS misfit of 0.71. For comparison, a unimodal log-normal distribution yield an RMS misfit of 0.85, and a unimodal normal distribution an RMS misfit of 0.93. These two populations approximately split into unmetamorphosed basalts and conglomerates (the lower susceptibility population), and metabasalts and granophyres, which make up the higher population.

Giles Suite intrusions

Based on field relationships and mineralogy, the Giles Suite can be divided into early-stage layered mafic–ultramafic intrusions (G1) and later-stage massive gabbroic intrusions (G2), although in absolute time these are within the uncertainties of current isotopic dating.

Specific-gravity measurements on G1 rocks can be approximated by a unimodal distribution, and a unimodal normal distribution with a mean of 3.10 ± 0.26 g/cm^3 provides a reasonable fit to the data (RMS = 2.74). More detailed analysis, excluding a single low outlier and extracting a sub-population of very dense rocks (SG >3.35 g/cm^3), provides improved misfit (RMS = 2.22). In this model, the main population (n = 75) has a mean of 3.05 ± 0.13 g/cm^3, whereas the denser population has a mean of 3.41 ± 0.05 g/cm^3. Visually, this model fits much better (Fig. 21), although there are still large discrepancies in some bins, in particular the 3.10 – 3.15 g/cm^3 bin, which has captured very few samples. This may relate to a petrophysical gap between different mineralogies, although it may also be a result of chance. A broad, unimodal log-normal distribution (log-susceptibility mean 6.33 ± 1.55; Figs 21 and 22) is sufficient to explain the susceptibility data, generating an RMS misfit of 1.66. Using a bimodal log-normal distribution with a cutoff at 375 x 10^{-5} SI units reduced the numerical misfit a little (RMS = 1.44), perhaps suggesting slight bimodality. Normal distributions produce a poor fit to the data.

Although near-unimodal distributions are observed for both specific gravity and magnetic susceptibility, the large number of samples permits further subdivision of these G1 rocks, according to their mineralogy, from which some trends can be derived (Table 4). In the mafic rocks, troctolites (WKg1-ot) and gabbros (WKg1-og) tend to be denser than norites (WKg1-ow), leucogabbronorites (WKg1-om), and leucocratic olivine gabbronorites (WKg1-ol). Olivine gabbros (WKg1-oo) and metagabbros (WKg1-mo) are of intermediate density. Magnetic susceptibilities of gabbros and leucocratic olivine gabbronorites are close to the overall mean. Norites are slightly less magnetic, and troctolites are less magnetic still, although not significantly so. Olivine gabbros tend to be slightly more magnetic than average, whereas leucogabbronorites are significantly more magnetic than the other mafic units. Metagabbros are also significantly more magnetic than average. Unsurprisingly, anorthosites (WKg1-oa) have the lowest density overall, although they are relatively magnetic, whereas magnetite-rich gabbros (WKg1-xooj-am) are the densest rocks of all, and are also strongly magnetic. There are few samples of ultramafic rocks. However, pyroxenites (WKg1-ax) and peridotites (WKg1-ap) have relatively low density (<3.3), and are typically nonmagnetic, although one poikilitic peridotite specimen yielded magnetic susceptibility close to average. A single sample of olivine websterite (WKg1-ao) indicates that this unit is dense, but nonmagnetic.

Petrophysically speaking, G2 rocks are quite different from G1 rocks. Although the population size is perhaps insufficient, specific-gravity measurements indicate a likely bimodal distribution, with a cutoff at 2.8 g/cm^3. This yields a lower population (n = 10) with a mean of 2.64 ± 0.10 g/cm^3, and a higher population (n = 16) with a mean of 3.07 ± 0.11 g/cm^3 (Fig. 21). The RMS misfit of this model is 1.06, compared to 1.32 for a unimodal distribution. There is no clear unit code correlation for this difference, although gabbros that display magma-mingling with leucogranite (WKg2-xog-g) form a significant component of the lower population, whereas leucogabbros and leucogabbronorites (WKg2-oga), including those mingled with leucogranite (WKg2-xoga-g), are dominantly in the upper population. This may indicate either a greater component of leucogranite in the gabbros, or a denser mafic component in the leucogabbros. The upper outlier corresponds to a garnet-bearing amphibolite unit (WKg2-moag).

Table 4. Petrophysical properties of Giles Suite G1 subdivisions

Unit code	*Count (n)*	*Specific gravity (g/cm^3)*			*Magnetic susceptibility*			
		Range	*Mean*	*Standard deviation*	*Range[(a)]*	*Mean[(a)]*	*Mean[(b)]*	*Standard deviation[(b)]*
WKg1-oa	4	2.43 – 3.00	2.79	0.25	420–1 077	708	6.56	0.47
WKg1-og	22	2.83 – 4.05	3.12	0.26	35–3 286	585	6.37	1.51
WKg1-ol	11	2.71 – 3.22	3.03	0.15	82–4142	533	6.28	1.32
WKg1-om	6	2.88 – 3.16	3.02	0.10	810–3 775	2 093	7.65	0.61
WKg1-oo	9	2.86 – 3.29	3.06	0.12	58–6 666	652	6.48	1.52
WKg1-ot	7	2.81 – 4.04	3.12	0.44	242–1 332	431	6.07	0.63
WKg1-ow	3	2.96 – 3.06	3.00	0.05	106–2 745	496	6.21	1.63
WKg1-mo	6	2.97 – 3.16	3.06	0.07	1232–5 385	2 588	7.86	0.53
WKg1-ax	10	3.04 – 3.46	3.23	0.14	9–336	87	4.47	1.19
WKg1-ap	2	3.04 – 3.32	–	–	39–580	–		–
WKg1-ao	1	3.42	–	–	78	–		–
WKg1-xooj-am	4	3.20 – 4.16	3.51	0.45	1 784–7 816	4 664	8.45	0.66

NOTES: (a) x 10^{-5} SI units

(b) ln(x 10^{-5} SI units)

The susceptibility data comprise a reasonably tight and discrete lower population (n = 5), with a mean of 3.8 ± 0.14, and a more distributed, higher-susceptibility population (n = 21) with a mean of 7.03 ± 0.84 (Figs 21 and 22). None of the applied statistical models produce a very good visual fit to the data, although a log-normal bimodal model fits best numerically (RMS = 1.21). All other models generate RMS misfits of ~1.38. Owing to the small population size, small differences in bin size and the relevant cutoff values may alter this histogram quite markedly, affecting both visual comparison and RMS misfit. Despite its tight grouping, the lower population contains five samples of different units, and so does not correlate with any particular unit. Within the higher population, mylonitic and strongly foliated units account for the higher values, whereas undeformed rocks occupy the lower end. Magnetite-rich gabbros (WKg2-ogj) return susceptibility values distributed across a range from 47 to 2898 x 10^{-5} SI units, perhaps reflecting the influence of leucogranite mingling, and perhaps also localized biotite enrichment.

Warakurna Supersuite granites

These granitic bodies are broadly synchronous with the Giles Suite mafic intrusions and are possibly genetically related. Specific gravity measurements indicate an unusual distribution of samples across a wide range, with distinct peaks at either end of the spectrum. This distribution is not easily modelled with either a unimodal normal distribution (RMS = 0.88) or a bimodal normal distribution (RMS = 0.79) (Fig. 21). However, there is some correlation with geological units. The lowest value corresponds to the only sample of quartz syenite (WK-ge). Medium-grained leucocratic granites (WK-gfl) show predominantly low values (2.56 – 2.72 g/cm^3), but with a single sample of very dense granite (>2.9 g/cm^3). Massive fine grained granodiorites (WK-gga) show a similar pattern, whereas clinopyroxene-bearing examples (WK-ggc) have higher density (2.82 – 2.86 g/cm^3). Mylonitic syenogranite (WK-mgry) is also very dense.

For susceptibility, the distribution is characterized by a bimodal, or possibly trimodal, distribution, although the population is undersampled. Using a cutoff of 58 x 10^{-5} SI units, the closest fit to the data (RMS = 0.67) is given by a model with a log-normal distribution with a log susceptibility mean of 2.81 ± 0.78 for the lower population (n = 7), and a normal distribution with a mean of 1219 ± 832 x 10^{-5} SI units for the higher population (n = 11) (Fig. 21). Using a log-normal model for the higher distribution generates a significantly higher numerical misfit (RMS = 0.78). For reference, unimodal log normal and normal models generate RMS misfits of 0.99 and 0.93 respectively. As with specific gravity, the unit codes show some correlation. Medium-grained leucocratic granites (WK-gfl) show dominantly moderate values (200–800 x 10^{-5} SI units), but with a single sample of very low susceptibility. Massive fine grained granodiorites (WK-gga) are all very low susceptibility, except clinopyroxene-bearing examples (WK-ggc), which are strongly magnetic (>2000 x 10^{-5} SI units). Mylonitic syenogranites (WK-mgry) are also magnetic (1300–1700 x 10^{-5} SI units).

Alcurra Dolerite

This widespread suite of mafic intrusions, most commonly dykes or sills, intruded across the latter stages of the Giles Event. Although only nine samples were measured, specific gravity measurements indicate that a unimodal normal distribution with a mean of 2.98 ± 0.17 g/cm^3 is adequate (RMS misfit = 0.50). Omitting outliers at either end results in a slightly better match to the observed histogram (Fig. 21, dashed line). Susceptibility data indicate a discrete lower population of three samples and an upper population of six samples. The numerical misfit of all models is similar, with the lowest misfit obtained by using a log-normal bimodal distribution. This distribution has lower and higher susceptibility populations with log-susceptibility mean of 5.28 ± 0.14 and 7.48 ± 0.39 SI units respectively (Figs 21 and 22). There is no clear correlation with unit codes.

Upper Bentley Supergroup

The upper Bentley Supergroup is composed of a series of volcanic–sedimentary packages. In approximate stratigraphic order, these are the Tollu Group, the Pussy Cat Group, the Mount Palgrave Group, the Cassidy Group, and the Mission Group. These rocks are dominated by volcanic rocks of felsic to intermediate composition, although there are several basaltic units and sedimentary rocks are also common.

Specific-gravity measurements for these units as a whole indicate a bimodal distribution, with an interpreted cutoff at 2.69 g/cm^3. This results in a lower population (n = 159) at 2.61 ± 0.06 g/cm^3, and a higher population (n = 164) at 2.93 ± 0.22 g/cm^3 (Fig. 21). The RMS misfit of this model is 4.39, and is a significant improvement over a unimodal model, which has an RMS misfit of 13.13. Many of the specimens sampled in this work were fresh from the field, and hence were not yet logged in the database. For these specimens geological linkages cannot yet be drawn, although it is likely that the strong lower population is dominated by rhyolites, whereas the more dispersed upper population contains rocks of andesitic and basaltic composition. The Tollu Group specimens are included in the database, and a more detailed analysis follows.

The Tollu Group is composed of the Smoke Hill Volcanics and the Hogarth Formation, which outcrop in the core of the Blackstone Syncline. Considered together, specific-gravity measurements for these units indicate a bimodal distribution, with a cutoff at 2.80 g/cm^3. This results in a lower population (n = 17) at 2.68 ± 0.08 g/cm^3, and a smaller upper population (n = 8) at 2.92 ± 0.07 g/cm^3. The RMS misfit of this model is 0.59, and is a significant improvement over a unimodal model, which has an RMS of 0.88. Considering these two units separately leads to similar populations for each at ~2.7 g/cm^3 and ~2.9 g/cm^3, although in the Hogarth Formation the two populations are roughly equal in size, whereas for the Smoke Hill Volcanics the lower population is dominant. Geologically, these populations can be linked to the major geological units, although significant overlap is observed. The lowest densities (2.47 – 2.73 g/cm^3) were found in the granophyric granites (TLs-gvh) of the Smoke Hill

Volcanics, with a median density of 2.64 g/cm^3. Rhyolites of the Smoke Hill Volcanics (TLs-frp) are slightly denser, typically 2.67 – 2.70 g/cm^3, but with a dense outlier. Trachytes of the Smoke Hill Volcanics (TLs-ftp) are denser still, ranging from 2.63 – 2.93 g/cm^3, with a median density of 2.77 g/cm^3. The Hogarth Formation is generally denser than the Smoke Hill Volcanics. Andesites of the Hogarth Formation include lower-density variolitic andesites (TLh-faw), which range from 2.69 – 2.76 g/cm^3, and higher-density acicular andesites (TLh-fa), which range from 2.77 – 2.86 g/cm^3. Rhyolites of the Hogarth Formation (TLh-frp) and related units are typically dense, ranging from 2.61 – 2.98 g/cm^3, and with a median density of 2.93 g/cm^3.

The susceptibility data from the upper Bentley Supergroup are best fitted by a bimodal model with a cutoff at 205 x 10^{-5} SI units. The lower population is best fitted by a normal distribution, with a mean of 77 ± 48 x 10^{-5} SI units, whereas the higher population is best fitted by a log-normal distribution with a log-susceptibility mean of 7.12 ± 0.8 SI units (Figs 21 and 22). This combination results in an RMS misfit of 5.75, compared to a misfit of 8.60 for a bimodal log-normal distribution, and 11.21 for a unimodal log-normal distribution. Once again, the Tollu Group provide the only specimens that can be analysed geologically. The Tollu Group are best fitted by a model with a bimodal distribution that combines a normal distribution below the cutoff (50 x 10^{-5} SI units), and a log-normal distribution above the cutoff. This results in a lower population (n = 7) at 26 ± 15 x 10^{-5} SI units, and a higher population (n = 18) at 6.86 ± 1.05 (log-susceptibility), and yields a RMS misfit of 0.76. A bimodal distribution with log-normal models for each population fits almost as well numerically (RMS = 0.79), but matches the population less well on visual comparison. For comparison, a unimodal log-normal distribution yields an RMS misfit of 1.12. Geologically, the lower population is dominated by Hogarth Formation andesites (TLh-fa, TLh-faw), all of which are very low susceptibility. Rhyolites and similar rocks from both formations span a broad range from very low to high susceptibility with a fairly evenly distributed population. Trachytes of the Smoke Hill Volcanics (TLs-ftp) are more magnetic, and range from 434–4300 x 10^{-5} SI units. Granophyric granites (TLs-gvh) yield a range of values across a moderate range (209–2274 x 10^{-5} SI units).

Other rocks

Several other rock types were analysed, but with population sizes too small to permit detailed analysis. These include eight unassigned mylonites and blastomylonites, which include a wide range of specific gravities (2.57 – 3.25 g/cm^3; Fig. 22), but are characterized by low and very low magnetic susceptibilities, typically less than 500 x 10^{-5} SI units. Three amphibolite gneiss samples indicate a density of 2.8 – 2.85 g/cm^3 and a magnetic susceptibility of 592–1010 x 10^{-5} SI units. Three mafic granulite samples indicate a density of 2.79 – 2.99 g/cm^3 and a magnetic susceptibility of 158–1731 x 10^{-5} SI units, and four felsic granulite samples indicate a density of 2.64 – 3.0 g/cm^3 and a magnetic susceptibility of 159–2951 x 10^{-5} SI units.

Summary of petrophysical data

The petrophysical data provide the basis for the density and susceptibility values used in forward modelling, and are used to constrain the gravity and magnetic inversions. As is common with petrophysical data, there is significant overlap between the petrophysical properties of different rock types (Fig. 22), and these properties do not provide a very reliable basis for geological discrimination. For example, many of the granites are quite dense (>2.8 g/cm^3), and some of the mafic rocks, especially Giles Suite G2, are relatively low-density (<2.7 g/cm^3).

Nevertheless, the main trends can be detected (Fig. 22). The density distributions for the granitic and gneissic suites are characterized by bimodal distributions, with sub-populations at ~2.65 g/cm^3, and 2.9 – 3.1 g/cm^3. Dense to very dense rocks characterize Giles Suite G1, but a bimodal distribution including relatively low-density rocks is observed for Giles Suite G2. The Alcurra Dolerite is composed of fairly typical mafic rocks, with specific gravities clustered in a limited range around 3 g/cm^3, although there are few samples. The Bentley Supergroup distribution shows a strong specific gravity peak at ~2.6 g/cm^3 superimposed on a distribution across a broad range (2.3 – 3.5 g/cm^3). For susceptibility, almost all units are bimodal (Fig. 22), with a higher population centred around a log-susceptibility of ~7 (~1000 x 10^{-5} SI units), and a lower population centred at a log-susceptibility of 3–4 (20–55 x 10^{-5} SI units).

Unimodal units, the Wankanki Supersuite and the Giles Suite G1 intrusions, have populations centred at approximate log-susceptibility of 6.4 (600 x 10^{-5} SI units). Fault rocks typically have lower susceptibility than the other rocks, and this points to the general relationship between the degree of deformation and changes in magnetic susceptibility. These distributions indicate that the variability of magnetic susceptibility is much greater within geological units than between them.

2D joint gravity and magnetic modelling

Here, we present the results of seven model cross sections that provide a fairly comprehensive view of crustal structure in the west Musgrave Province (see Fig. 2a for profile locations).

Data, methods, and scope

Magnetic data for modelling were sampled from a reduced-to-pole (RTP) magnetic grid derived by stitching together RTP grids of several individual surveys with flight-line spacings of 200–400 m, and nominal flying heights of 80–100 m. Most were flown north–south. However, some were flown east–west. Visible artefacts resulting from the stitching process are few (Fig. 2a), although longer wavelength trends may be misrepresented as a result of the detrending process associated with grid stitching. Northern Territory Geological Survey magnetic

data were required at the northern end of profile 7, but these were able to be directly appended to the WA data with no adjustment. The magnetic grid was upward-continued by 100 m and was sampled at 500 m spacing. Magnetic calculations in modelling used a sensor height of 200 m above model topography. For gravity modelling, geoid-corrected free-air gravity measurements from Geoscience Australia's national database were gridded at 500 m cell size (Fig. 2b). This grid was also sampled at 500 m spacing for modelling. Gravity measurement elevations from the same database were also gridded, and form the basis of the model topography, which is sampled beneath each data point. Gravity calculations in modelling used a sensor height of 1 m above model topography.

Forward modelling is an effective and fairly robust method when applied using geological and petrophysical constraints. The method used here involves, as a first step, the construction of an interpreted geological cross section. Geological cross sections were constructed using the distribution of lithologies in mapped in outcrop (where available), and interpreted geology elsewhere.

In addition, the initial crustal structure is constrained by the WAROX database of structural measurements. Measurements used include primary structures (bedding and igneous layering) as well as secondary structures (cleavages or foliations, fold plunges, etc.). Although these data provide a useful guide to the geometry of the subsurface, they are prone to error for several reasons. Firstly, these measurements are rarely exactly on the profile, and are typically clustered in dense groups. Therefore, the structural geometry must be averaged and extrapolated. This is particularly important where the measurements strike near-parallel with the profile. Secondly, with the exception of bedding, the structural data in this database are not explicitly linked to particular deformation events or larger scale structures. Finally, the structures indicated by these structural observations do not necessarily correlate with the geophysically defined features. Igneous layering in the volcanic units is chaotic and is not parallel to bedding in the sedimentary rocks beneath, so these data are not used. As a result of these uncertainties, the data are considered to be a guide to geometry, rather than a firm constraint.

Seismic data throughout central-western Australia indicate generally thick crust (Collins et al., 2003; Kennett et al., 2011). From this, the crust–mantle boundary is assumed initially to be at 50 km depth, and the lower crust – upper crust boundary is assumed initially to be at a depth of 25 km. Throughout modelling, these boundaries were assumed to be parallel. Adjustment of these boundaries was generally avoided, but was introduced where required by long-wavelength data trends or supported by geological inference.

The starting models are populated with statistically acceptable petrophysical properties to achieve an approximate fit before starting the modelling of near surface structure. Near-surface structure, i.e. the top few kilometres, is primarily defined by generating a fit to the magnetic data, although short-wavelength gravity anomalies were considered where they are preserved in the data. Once near-surface structure is defined, the deeper crust is modelled, with an emphasis on the fit to the gravity data. Where applicable, the magnetotelluric-derived conductivity models were used to constrain the deeper structure.

Ultimately, the models generated using this method can be considered as geological models of crustal structure that satisfy both gravity and magnetic data. As such, they may include features that are not required by the geophysical data, but are supported by geological inference, and serve to illustrate the likely geological scenario. For example, thin layers are often continued to depths beyond their limit of sensitivity on the basis that they are part of a conformable package of rocks.

Results

Profile 1 (Figure 23)

This profile traverses the west Musgrave Province from west to east, crossing all the main tectonic zones of the region, and some of the largest gravity and magnetic anomalies (Fig. 2). The profile is targeted at understanding the thickness and geometry of the Bentley Supergroup and the Jameson intrusion (G1), and understanding shear-zone architecture in the Tjuni Purlka and Walpa Pulka Zones (Fig. 23).

The western half of the model is characterized by shallowly southwest dipping layering, including the ~8-km-thick G1 Jameson intrusion (from 125–155 km on horizontal axis), and a thick sequence of volcanic–sedimentary packages of the Bentley Supergroup. Although gravity above the outcropping portion of the Jameson intrusion is higher than background, the highest gravity values lie above the Winburn granite (115–125 km) and the felsic volcanic rocks of the Mount Palgrave Group (88–115 km). This situation requires the dense Jameson intrusion to extend significantly westwards beyond its surface extent. The model includes a 2-km-thick layer of dense (3400 kg/m^3), material at the top of the subsurface part of the Jameson intrusion. The most likely geological explanation for this is the presence of magnetite-rich gabbro. Such rocks do not outcrop where the profile crosses the intrusion, but numerous magnetite seams are common in the upper parts of the intrusion, which is exposed to the north–west. In this model, the thickness of the Jameson intrusion is preserved, and west-up reverse faulting is called upon to satisfy subpeaks in the gravity anomaly. Alternatively, these subpeaks could be satisfied by thickening of the intrusion, or by additional density variations within the intrusion or the overlying units.

The Winburn granite (115–125 km) lies above the Jameson intrusion, and this stratiform intrusion has a dense, high-susceptibility lower layer (13 000 x 10^{-5} SI units), and a lower density, non-magnetic layer above. The Mount Palgrave Group (88–115 km) is dominated by shallow west-dipping layering, although several microgranite intrusions disrupt the stratigraphy. Continuing west, a region of more complex structure is reached, with the east-

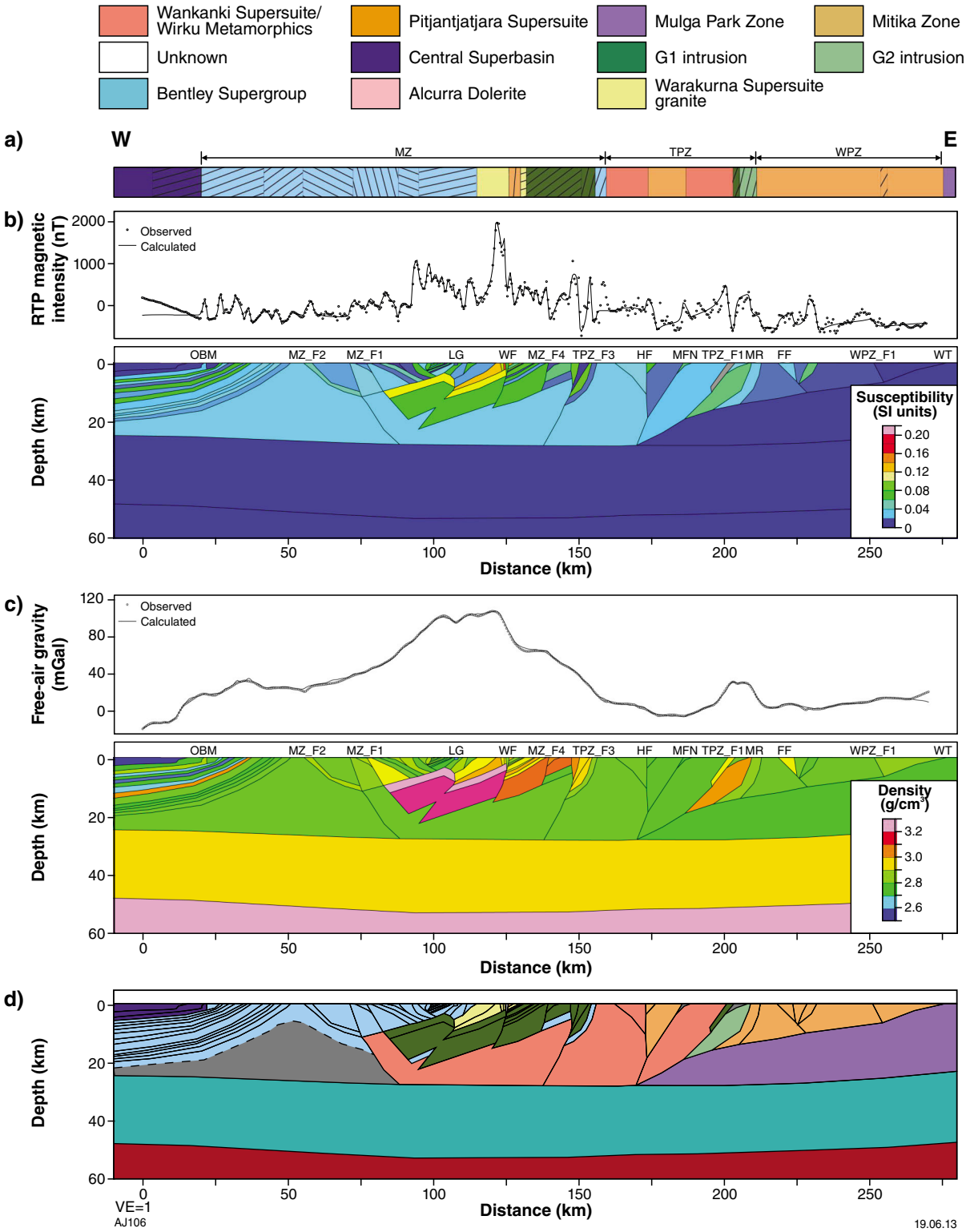

Figure 23. Joint magnetic and gravity model along profile 1 (see Fig. 2a for location) showing: a) interpreted geology. Hash pattern indicates apparent dips derived from structural measurements; b) magnetic-susceptibility distribution and the fit to magnetic data. Units with remanent magnetization are coloured grey; c) density distribution and the fit to gravity data; d) interpreted geological fit to magnetic and gravity data. The locations of major faults and shear zones are annotated using the same names as Figure 2 (MF, HF, TPZ_F1, etc). This profile emphasizes the different structure in each zone. The Mamutjarra Zone is characterized by shallowly southwest-dipping layering, the Tjuni Purlka Zone is characterized by steeply dipping fault zones, and the Walpa Pulka Zone is characterized by shallowly south-dipping structures. VE = vertical exaggeration

dipping Pussy Cat Group juxtaposed against the Mount Palgrave Group (F1). The Jameson intrusion continues beneath this structure, but is truncated by a major north-east dipping structure (MZ_F1, Fig. 23b,c). This structure is interpreted as the syn-emplacement bounding fault of the Jameson intrusion, although, because it cuts the c. 1070–1063 Ma Mount Palgrave Group, it is interpreted as a late Giles Event-age structure (Joly et al., 2013). The westernmost part of the profile is characterized by a broad, asymmetric antiform, with north-dipping Scamp Formation rocks (61–73 km) to the north, Pussy Cat Group (41–61 km) exposed along the axis, and the shallowly south-dipping Cassidy (35–41 km) and Mission (26–35 km) Groups to the south. The Cassidy and Mission Groups, along with the overlying Neoproterozoic Officer Basin, are largely undeformed and have distinct gravity and magnetic anomalies associated with the basaltic layers within these groups.

The eastern half of the profile traverses the high-metamorphic grade Tjuni Purlka and Walpa Pulka Zones, which are characterized by moderately dense (2770 kg/m^3) basement rocks. The Tjuni Purlka Zone is broken into discrete crustal blocks by several shear zones, most of which have planar geometries and fairly steep dips. These include the Hinckley Fault (173 km), the Mann Fault North (185 km) and Tjuni Purlka Zone F1 fault (TPZ_F1, 200 km). A small Giles Suite (G1) intrusion lies next to this shear zone and geological data suggest that this intrusion dips to the southwest at 50–75°. With this geometry, remanent magnetization is required to satisfy the aeromagnetic anomaly. Although unconstrained by rock-property data, magnetization of 3 A/m with an inclination of 15° and declination of 100° fits the RTP data well. This intrusion is in faulted contact with the Murray Range Gabbro (G2), which also dips steeply to the southwest, and is characterized by relatively dense (2950 kg/m^3) and magnetic (5000 x 10^{-5} SI units) rocks.

The Walpa Pulka Zone contains a mixture of dense, high-susceptibility Pitjantjatjara Supersuite and lower density, low-susceptibility Wirku Metamorphics rocks. Structures are more shallowly dipping than those in the Tjuni Purlka Zone, and the major examples (The Fanny Fault and WPZ_F1) each dip to the northeast at ~50°. Gravity data support the existence of low-density (2680 kg/m^3) crust beneath the shallow south-dipping Woodroffe Thrust (200–275 km), which likely merges into TPZ_F1 at depth.

Profile 2 (Figure 24)

This profile crosses the westernmost part of the Musgrave Province from south to north. The purpose of this profile is to understand the structure of the Bentley Supergroup, the geometry of the Woodroffe Thrust, and the nature of the crust in the intervening Mitika Zone, which is of uncertain origin.

As in profile 1, the Officer Basin and the Mission and Cassidy Groups are characterized by shallow southerly dips, and are essentially undeformed. The same antiformal architecture is observed in the Bentley Supergroup, with Pussy Cat Group exposed at the fold axis and north-dipping Scamp Formation to the north. However, the structure of the Scamp Formation (56–90 km) is much better defined. This region is characterized by high-amplitude gravity and magnetic anomalies that are modelled using a synform–antiform pair. The geometry of this folding is constrained by a series of asymmetric magnetic anomalies that require dip reversals coincident with the axial trace of the fold, clearly visible in aeromagnetic data (Fig. 2a). The depth extent of these thin layers is poorly constrained. This region is bounded to the north and south by steeply north-dipping faults. The northernmost of these, MZ_F1, is a fundamental boundary, juxtaposing the high-density, high-susceptibility Scamp Formation against the low-density, low-susceptibility crust of the Mitika Zone.

The Mitika Zone shares many characteristics with the crust of the Mulga Park Zone, including layered rocks of similar magnetic and gravity character to the Tjauwata Group. The Mitika Zone is interpreted to overlie a shallowly south-dipping Woodroffe Thrust, although petrophysical contrast across this shear zone is small.

Profile 3 (Figure 25)

This profile follows the east–west magnetotelluric profile (although Figure 25 is oriented west–east), and is intended to link the structures in the magnetotelluric models with the gravity, magnetic, and geological data. Owing to kinks in the magnetotelluric profile, this profile was modelled as three separate linear segments (Figs 2 and 25).

The western segment is oriented NW–SE, and extends from the Mitika Zone into the Bentley Supergroup-dominated western Mamutjarra Zone. In this profile the Mitika Zone is characterized by low-density, low-susceptibility resistive crust, but with a ~2-km-thick layer of lower density, higher conductivity material of variable magnetization. This surficial layer is interpreted to represent Tjauwata Group sedimentary rocks overlying felsic basement, similar to that of the Mulga Park Zone. The boundary with the Mamutjarra Zone at ~40 km is a steeply dipping structure (MZ_F1), marked by a zone of low-density and low-susceptibility crust. This boundary does not have any apparent electrical character. South of MZ_F1, magnetic and gravity highs over the Scamp Formation rocks are best fitted by a sill approximately 1-km-thick. A second north-dipping structure at ~55 km (MZ_F2) juxtaposes the high-density, high-susceptibility Scamp Formation against the low-density, low-susceptibility Pussy Cat Group, and this structure is associated with a prominent zone of high

Figure 24. (facing) Joint magnetic and gravity model along profile 2 (see Fig. 2a for location) showing: a) interpreted geology; b) the magnetic susceptibility; c) density distributions; d) interpreted geological fit to magnetic and gravity data. See Figure 23 caption for other details. This profile shows the southwest dipping structure within the southwest Mamutjarra Zone, upright folding near the margin with the Mitika Zone, the structure within the Mitika Zone, and its boundary (the Woodroffe Thrust) with the petrophysically similar Mulga Park Zone.

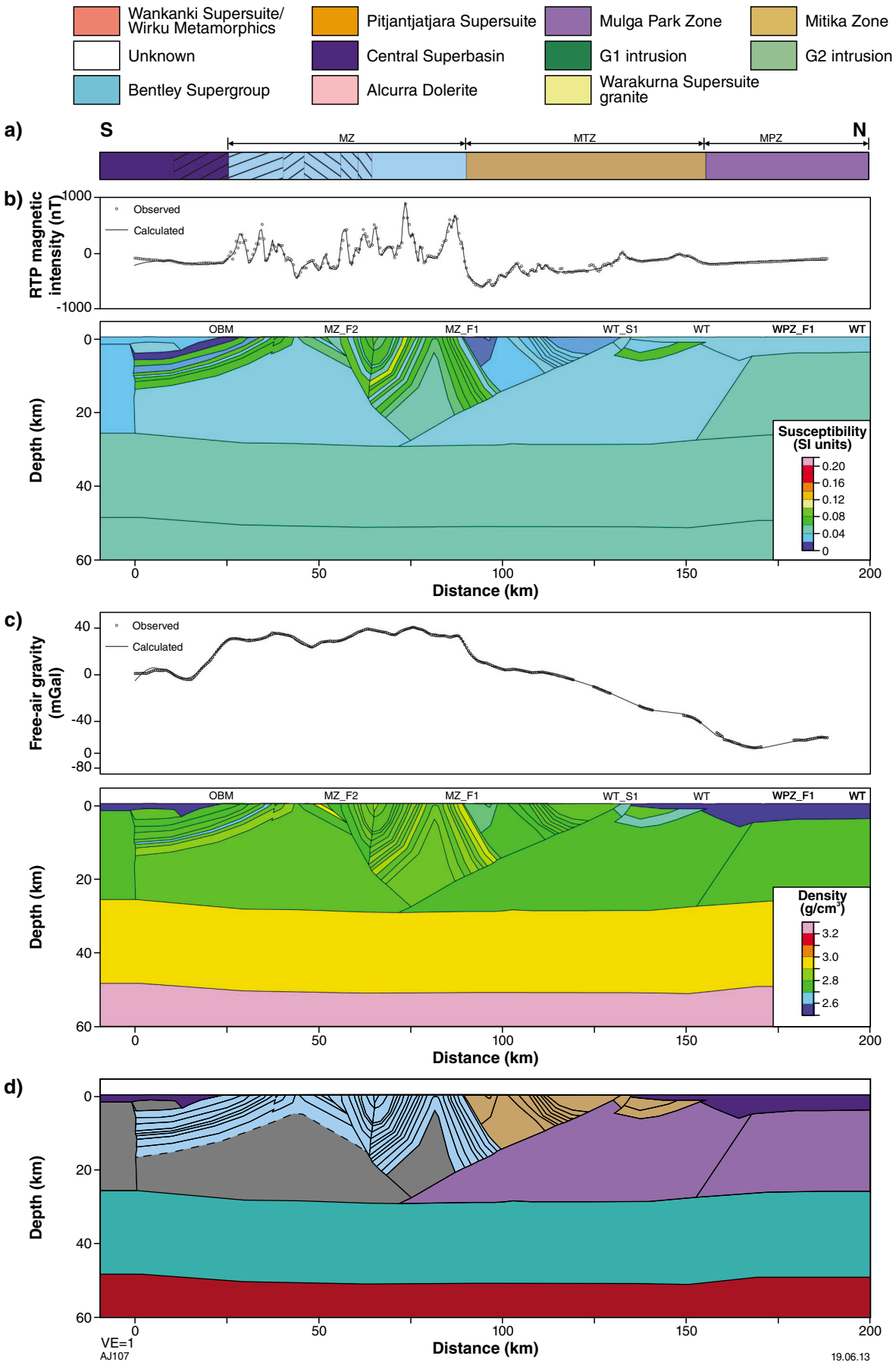
Wankanki Supersuite/ Wirku Metamorphics
Pitjantjatjara Supersuite
Mulga Park Zone
Mitika Zone
Unknown
Central Superbasin
G1 intrusion
G2 intrusion
Bentley Supergroup
Alcurra Dolerite
Warakurna Supersuite granite
a)
S
N
MZ
MTZ
MPZ
b)
RTP magnetic intensity (nT)
Observed
Calculated
OBM
MZ_F2
MZ_F1
WT_S1
WT
WPZ_F1
WT
Depth (km)
Susceptibility (SI units)
0.20
0.16
0.12
0.08
0.04
0
Distance (km)
c)
Free-air gravity (mGal)
Observed
Calculated
Density (g/cm3)
3.2
3.0
2.8
2.6
d)
VE=1
AJ107
19.06.13

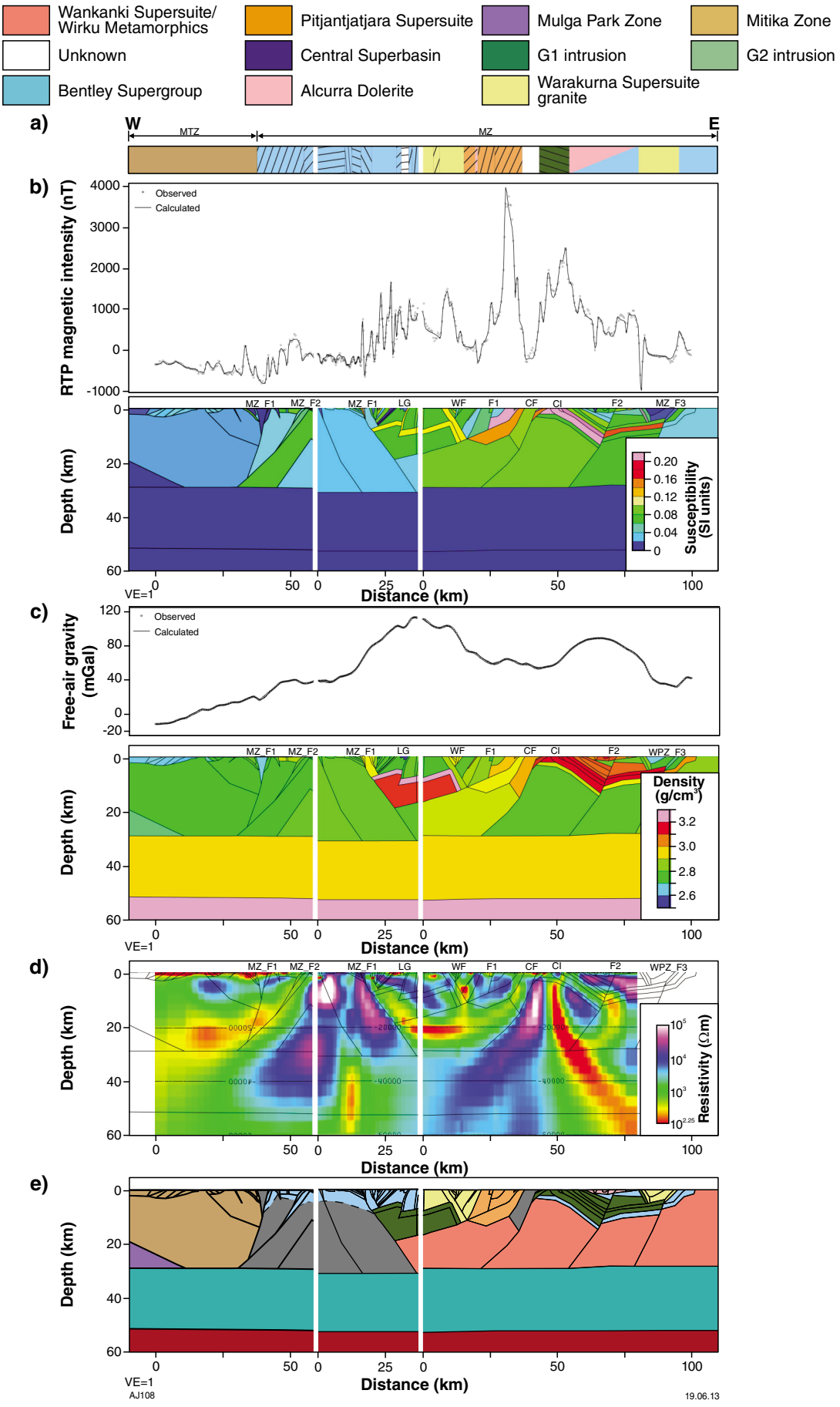
Wankanki Supersuite/ Wirku Metamorphics
Pitjantjatjara Supersuite
Mulga Park Zone
Mitika Zone
Unknown
Central Superbasin
G1 intrusion
G2 intrusion
Bentley Supergroup
Alcurra Dolerite
Warakurna Supersuite granite
a)
W
E
MTZ
MZ
b)
RTP magnetic intensity (nT)
Observed
Calculated
Depth (km)
MZ_F1
MZ_F2
LG
WF
F1
CF
CI
F2
MZ_F3
Susceptibility (SI units)
VE=1
Distance (km)
c)
Free-air gravity (mGal)
WPZ_F3
Density (g/cm3)
d)
Resistivity (Ωm)
e)
AJ108
19.06.13

Figure 25. (facing) Joint magnetic and gravity model along profile 3 (see Fig. 2a for location) showing: a) interpreted geology; b) magnetic susceptibility; c) density distributions. This profile is coincident with the west–east MT line, for which the model is shown in panel (d) using a log-resistivity scale; e) interpreted geological fit to magnetic and gravity data. See Figure 23 caption for other details. Due to kinks in the MT line, gravity and magnetic modelling were undertaken in three linear segments. Although these models extend beyond the MT data, only the portion that coincides with the MT model is shown. This model demonstrates the structure within the southeast Mamutjarra Zone, which is dominated by post-Giles Suite faulting.

conductivity. MT feature testing suggests that while high conductivity in this region is required, its geometry is not especially well constrained (Fig. 16).

The short central section is oriented southwest–northeast, and extends into the Mount Palgrave Group. The structure is similar to profile 1, showing shallow to moderately east-dipping Pussy Cat Group (0–17 km) truncated against a moderately northeast-dipping structure that also truncates the west-dipping Mount Palgrave Group and the Jameson intrusion (MZ_F1). This is the same structure that truncates the Jameson intrusion in profile 1. Magnetotelluric data indicate that this structure is also associated with a zone of high conductivity.

The eastern section is oriented east–west, and extends across the Cavenagh Fault into the Blackstone region, extending as far as the Tollu granite intrusion. West of the Cavenagh Fault, the profile is characterized by west-dipping architecture. As in profile 1, the Winburn granite (0–15 km) is interpreted to overlie the high-density Jameson intrusion, which dips shallowly to the west. A steep, Y-shaped structure marked by high conductivity separates the Winburn granite from Pitjantjatjara Supersuite basement (15–36 km). This basement region is primarily moderate-density, low-susceptibility, and resistive, but with an embedded very high susceptibility (25 000 x10^{-5} SI units), dense, west-dipping intrusion. This intrusion is truncated by a fault (F1), marked by a small conductive zone. The Cavenagh Fault (36–42 km) is demarcated by a steeply west-dipping zone of high density and low-susceptibility relative to the adjacent rocks, and high conductivity. The footwall to the Cavenagh Fault is highly resistive, although it contains a prominent steeply dipping conductor (50 km). This conductor is a robust feature of the magnetotelluric model (Fig. 16). It does not correlate with any particular feature in the gravity and magnetic model, but is truncated at the base of the Cavenagh intrusion, suggesting that it predates the Giles Event.

The Giles Suite Cavenagh intrusion (G1) lies immediately to the east of the Cavenagh Fault. This intrusion dips fairly shallowly to the northeast, and is characterized by high density (3150 kg/m^3). Very high susceptibility is required to achieve the magnetic anomalies observed, and although remanent magnetization is not required to satisfy the magnetic data here, they are necessary elsewhere within the Cavenagh intrusion (e.g. profile 4, Fig. 26), and remanent magnetization of normal polarity is likely a component of the magnetization here. Although disrupted by faulting, the Cavenagh intrusion extends beneath the Tollu Group and Blackstone intrusion for ~50 km. The change in apparent dip indicates a change from northeast-dipping layering to north-dipping layering across a steeply northwest-dipping Fault (F2). Offsets of the Tollu Group and Giles Suite intrusions on this fault indicate approximately 3 km of normal displacement. In the magnetotelluric data, the Cavenagh intrusion is demarcated by a prominent east-dipping conductor, whereas the Blackstone intrusion above is resistive. Outcrop in the region east of the Cavenagh intrusion (55–80 km) is characterized by outcrops of the Tollu Group, predominantly Smoke Hill Volcanics, interspersed with outcrops of Alcurra Dolerite. The magnetotelluric model indicates an extensive, flat, shallow conductor in this region. This feature, along with high gravity and magnetic values in this region, is interpreted to image a 1-km-thick sill of Alcurra Dolerite extending 62–80 km.

Immediately west of the c. 1076 Ma Tollu granite (80–95 km), strong negative magnetic anomalies indicate tilted Giles Suite rocks similar to those at the base of the Cavenagh intrusion. Remanent magnetization of 3 A/m, and an inclination of –90° fits this anomaly well. The Tollu granite itself is low density (~2650 kg/m^3) and low susceptibility (<2000 x 10^{-5} SI units), has tabular geometry, and is ~5 km thick. The Tollu granite is underlain by a fault that is the limiting boundary of the Blackstone and Cavenagh intrusions and likely also controlled the location of the Tollu granite (MZ_F3). Although the last significant motion on this fault is interpreted to be late Giles Event, the control of these igneous units suggests ongoing activity on this fault zone throughout the Giles Event.

Profile 4 (Figure 26)

This north-northwest-oriented profile is aimed at generating insight into the geometry of the Cavenagh intrusion, the Cavenagh Fault, and the Jameson intrusion. The Officer Basin margin (OBM, 22–25 km) is characterized here by moderately north-dipping layering within low-density Wirku Metamorphics rocks (2600 kg/m^3). In contrast to the profiles farther west, the Bentley Supergroup is absent from this area, and basement rocks of the Wirku Metamorphics and Wankanki Supersuite dominate inboard of the margin. The shallow northwest-dipping structure of this region reflects north-plunging folding of the Wirku Metamorphics and Wankanki Supersuite, interpreted to be of Musgrave Orogeny age, based on the intrusion of low-susceptibility, high-density Pitjantjatjara Supersuite granite into the contact between these units (Joly et al., 2013).

North of the ~50 km mark, basement rocks are overlain by the shallowly northeast-dipping Cavenagh intrusion. On this profile, the Cavenagh intrusion is demarcated by very strong magnetic anomalies, but an increase of only 15 mGal in gravity. The shallow dip of the intrusion suggests a maximum thickness of 3 km; this requires a density of 2900–3000 kg/m^3. Obeying the geometrical constraints, the very strong negative magnetic anomalies

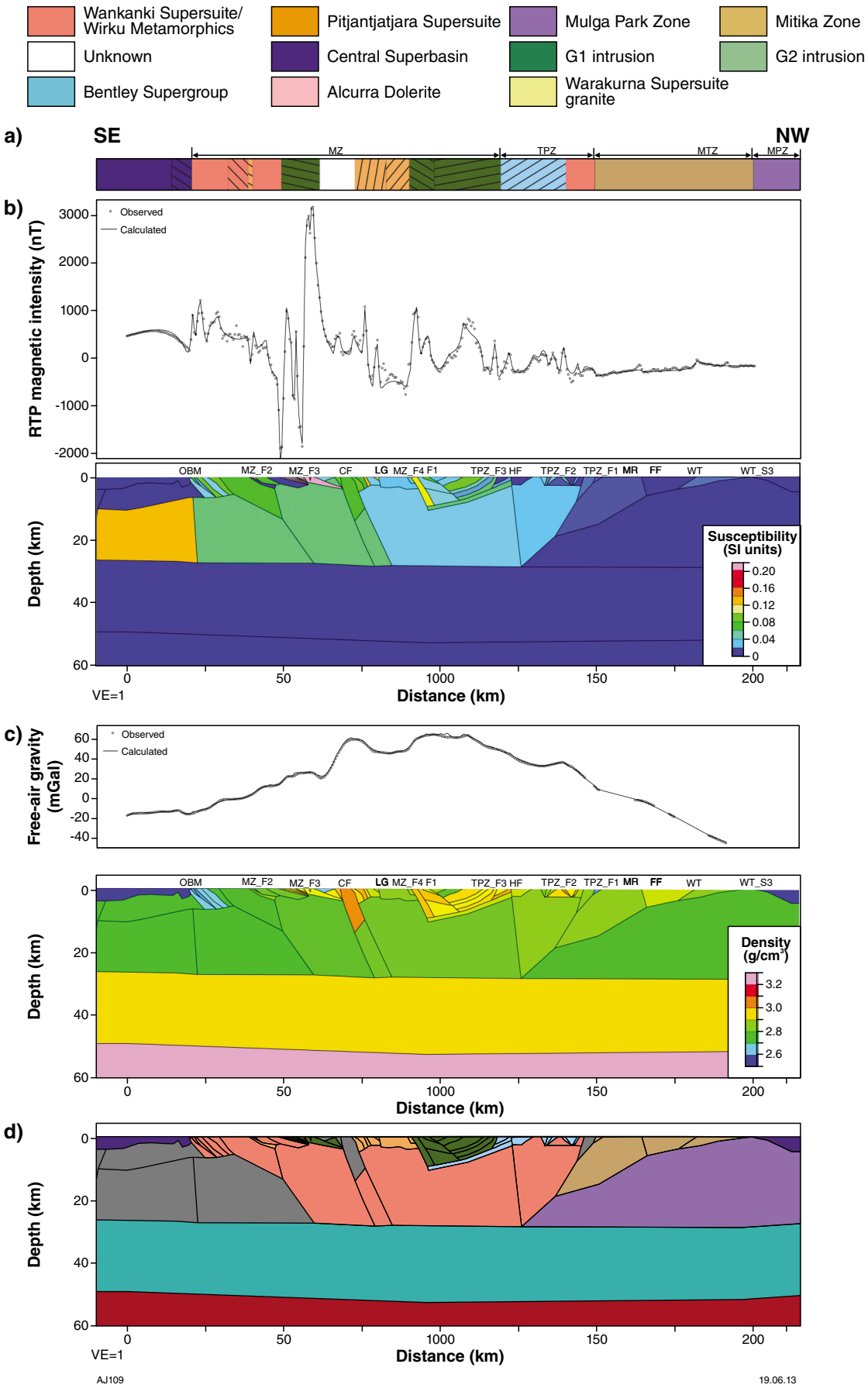
Wankanki Supersuite/ Wirku Metamorphics
Unknown
Bentley Supergroup
Pitjantjatjara Supersuite
Central Superbasin
Alcurra Dolerite
Mulga Park Zone
G1 intrusion
Warakurna Supersuite granite
Mitika Zone
G2 intrusion
a)
SE
NW
MZ
TPZ
MTZ
MPZ
b)
RTP magnetic intensity (nT)
Observed
Calculated
OBM
MZ_F2
MZ_F3
CF
LG
MZ_F4
F1
TPZ_F3
HF
TPZ_F2
TPZ_F1
MR
FF
WT
WT_S3
Depth (km)
Susceptibility (SI units)
0.20
0.16
0.12
0.08
0.04
0
VE=1
Distance (km)
c)
Free-air gravity (mGal)
Observed
Calculated
Density (g/cm³)
3.2
3.0
2.8
2.6
d)
AJ109
19.06.13

Figure 26. (facing) Joint magnetic and gravity model along profile 4 (see Fig. 2a for location) showing: a) interpreted geology; b) magnetic susceptibility; c) density distributions; d) interpreted geological fit to magnetic and gravity data. See Figure 23 caption for other details. This profile shows the geometry of the Cavenagh Fault and the Jameson intrusion, and the Woodroffe Thrust.

cannot be achieved with low susceptibility alone, and remanent magnetization was introduced. Although this remanence is not constrained by petrophysical measurement, magnetization with an inclination of –75°, declination of 105°, and intensity between 2.5 and 10 A/m, fits the RTP anomalies well. The intervening positive anomalies can be largely explained by very high magnetic susceptibility (25000 x 10^{-5} SI units), although adding remanence of opposite orientation to the negatively magnetized units (I = 75, D = –75), and intensity of between 2 and 10 A/m, produces a better fit to the slope of the curves. From southeast to northwest, the intensity of remanent magnetization reduces for both positively and negatively magnetized units, indicating that the lowermost layers in the intrusion possess the strongest remanent magnetization. These lowermost layers are fine- to medium-grained, leucocratic olivine gabbronorites, whereas the upper layers are coarse-grained leucotroctolite, and so this may represent the influence of faster cooling rates resulting in smaller grain size, and hence stronger remanent magnetization (Dunlop and Ozdemir, 1997).

The Cavenagh intrusion is truncated by the Cavenagh Fault (67–73 km), which displays high gravity, and a slightly subdued magnetic response relative to the surroundings. Although the nature of the geology beneath cover here is not known, the geophysical data suggest the fault zone is occupied by dense rocks (2980 kg/m^3) that extend to significant depth (~10–15 km). The hanging wall of the Cavenagh Fault is occupied by Pitjantjatjara Supersuite basement rocks, typified by low to moderate susceptibility and moderate to high density. These extend 73–92 km, where a late-Giles Event aged fault (MZ_F4) juxtaposes these rocks against the Jameson intrusion. The Jameson intrusion, which is ~8 km thick immediately north of this fault, thins gradually to the northwest, until its fault-bounded margin is reached at 121 km, at the Hinckley Fault (HF).

North of the Hinckley Fault is the Tjuni Purlka Zone, which consists of fairly homogenous Wankanki Supersuite basement, overlain by Kunmarnara Group rocks. Overall, steeply south-dipping structures dominate in this region. A major south-dipping shear zone (TPZ_F1) is encountered at 148 km, demarcated by a drop in gravity, and a transition from moderately magnetic rocks of the Tjuni Purlka Zone to the non-magnetic rocks of the Mitika Zone. The gravity anomaly north of this shear zone indicates relatively dense crust (2800 kg/m^3) above the Woodroffe Thrust, with low-density Mulga Park Zone (2700 kg/m^3) rocks beneath. The Woodroffe Thrust dips shallowly to the south, and is interpreted to merge with TPZ_F1 at approximately 20 km depth.

Profile 5 (Figure 27)

This profile follows the south–north MT profile, which begins within the Officer Basin, and follows an arcuate geometry through the Mamutjarra Zone, Tjuni Purlka Zone, and Walpa Pulka Zone, extending into the Mulga Park Zone (Fig. 2). Due to the arcuate geometry of this profile, it was also modelled in three separate sections — south, central, and north. Models were extended beyond the limits of the MT data, but only the portion coincident with the MT data is shown.

In the southern section of the profile, the Officer Basin contains relatively high-density (2650 kg/m^3), low-susceptibility sedimentary rocks that coincide with a flat-lying conductive feature. These are underlain by a large, highly magnetic body. It needs to be noted that the near-vertical conductive feature in this area is not a stable feature of the MT inversion (Fig. 15b). As with profile 4, there are no Bentley Supergroup rocks in this location, but there are basement rocks that are thrust over the Officer Basin. The marginal thrust is also associated with a conductive anomaly that dips moderately to the north and extends to at least 50 km depth. Inboard of the basin margin, the rocks show shallowly south-dipping layering relating to intercalated Wankanki Supersuite and Wirku Metamorphics. At ~65 km, this gives way to apparent north-dipping structure as the profile traverses the eastern limb of a north-plunging antiform (Joly et al., 2013). The fold is truncated by a steeply north-dipping late Giles Event-age structure at ~78 km, beyond which the Giles Suite intrusions dominate.

The central section crosses the Blackstone Syncline at an oblique angle, and clearly shows the geometry of this structure. The Cavenagh intrusion dips moderately northeastward, reaching a maximum depth of ~15 km. The Blackstone intrusion lies above the Cavenagh intrusion and is folded in from the north, although these intrusions are in faulted contact here due to a NW-dipping normal fault (F1). This fault is crossed at ~2 km, and runs near-parallel to the profile, but is interpreted to intersect the profile at 7–8 km depth, based on a dip of 60°. This is the same fault that disrupts these intrusions in profile 3, where it is denoted F2.

Along the central section, outcrop from 2 to 19 km is dominated by Tollu Group interspersed with Alcurra Dolerite, and modelling suggests that on this profile the southern part (2–15 km) is dominated by dense Alcurra Dolerite rocks, with rhyolitic Smoke Hill Volcanics occupying only a small wedge 15–19 km (cf. profile 6). The outcropping Blackstone intrusion (19–28 km) dips very steeply to the south, which results in very steep gravity and magnetic gradients. This intrusion can also be directly associated with a steeply dipping resistive anomaly that extends to ~25 km depth. This is beyond the probable extent of the Blackstone intrusion, given the nature of the folding and the expected density of the Blackstone intrusion. Tests show that the MT data require the zone to be this thick, but this is also an area where the modelled data are sparse (Fig. 11), and this may explain the lack of apparent correlation. An alternative explanation is that the resistivity model is over-smoothed as a result of model regularization.

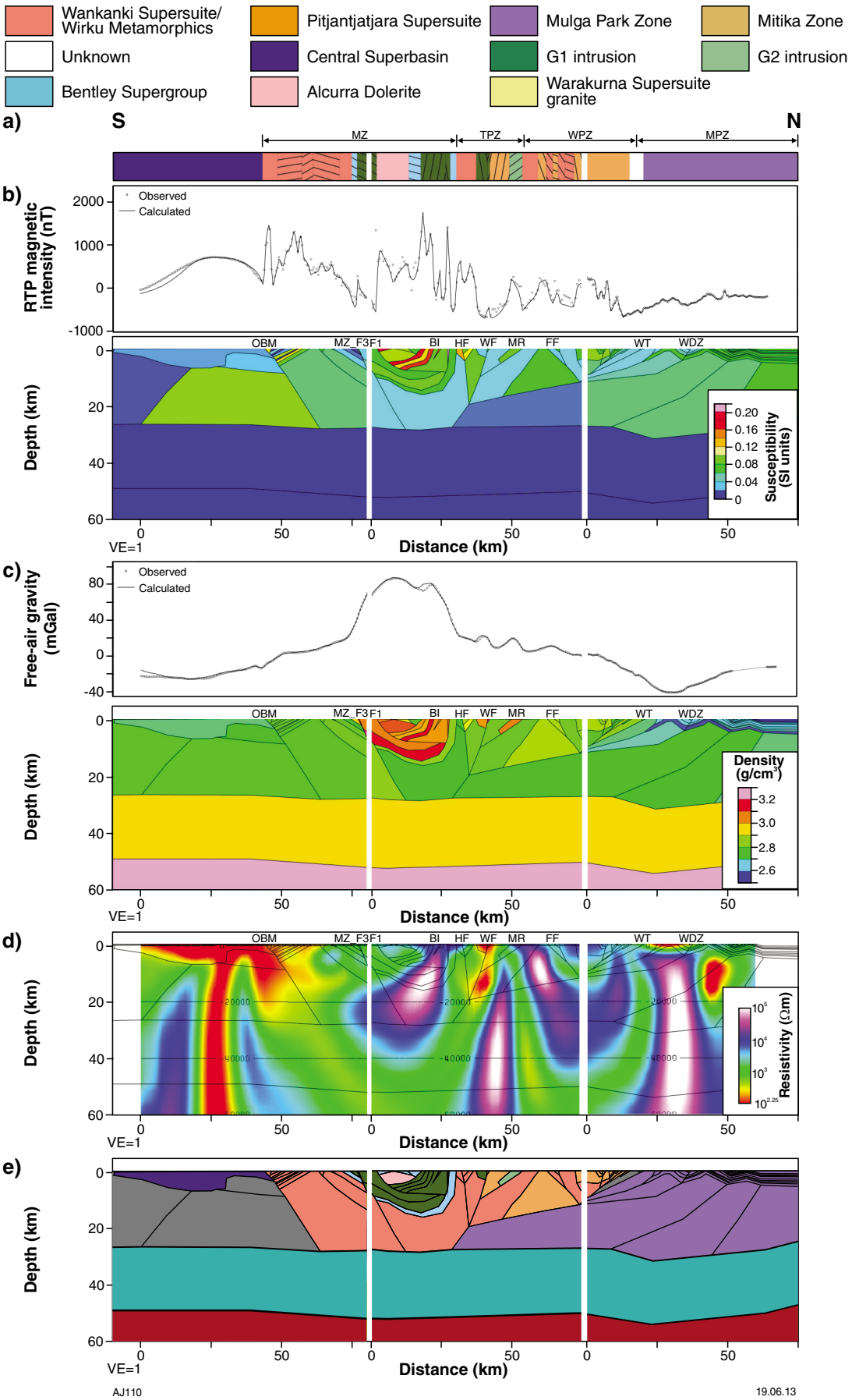
Wankanki Supersuite/ Wirku Metamorphics
Pitjantjatjara Supersuite
Mulga Park Zone
Mitika Zone
Unknown
Central Superbasin
G1 intrusion
G2 intrusion
Bentley Supergroup
Alcurra Dolerite
Warakurna Supersuite granite
a)
S
N
MZ
TPZ
WPZ
MPZ
b)
RTP magnetic intensity (nT)
Observed
Calculated
2000
1000
0
-1000
OBM
MZ_F3
F1
BI
HF
WF
MR
FF
WT
WDZ
Depth (km)
0
20
40
60
0.20
0.16
0.12
0.08
0.04
0
Susceptibility (SI units)
VE=1
Distance (km)
c)
Free-air gravity (mGal)
Observed
Calculated
80
40
0
-40
Density (g/cm3)
3.2
3.0
2.8
2.6
d)
Resistivity (Ωm)
e)
AJ110
19.06.13

Figure 27. (facing) Joint magnetic and gravity model along profile 5 (see Fig. 2a for location) showing: a) interpreted geology; b) magnetic susceptibility; c) density distributions. This profile is coincident with the south–north MT line, for which the model is shown in panel (d) using a log-resistivity scale; e) interpreted geological fit to magnetic and gravity data. See Figure 23 caption for other details. Due to kinks in the MT line, gravity and magnetic modelling were undertaken in three linear segments. Although these models extend beyond the MT data, only the portion that coincides with the MT model is shown. This profile shows the Blackstone Syncline, a steeply dipping Mann Fault, the shallow-dipping structure of the Walpa Pulka Zone, and the relatively little-deformed Tjauwata Group over the Mulga Park Zone.

North of the Blackstone intrusion, the profile crosses into the Tjuni Purlka Zone and, as observed on profile 1, the structural character is dominated by moderately dense and magnetic basement rocks dissected by several shear zones. Foremost amongst these is the Mann Fault (44 km). This steeply south-dipping structure is characterized in this profile by the truncation of a gabbroic Giles Suite intrusion, and by a conductive anomaly, which extends strongly to ~20 km depth. The anomaly extends less strongly to the base of the crust and into the mantle, where it intersects the north-dipping conductivity anomaly from the Officer Basin margin. North of the Mann Fault, near-surface structures are more shallowly dipping, and include the Murray Range Gabbro (47–54 km), which dips shallowly to the west. The eastern-bounding fault of this intrusive complex demarcates the transition from the Tjuni Purlka Zone to the Walpa Pulka Zone.

Within the Walpa Pulka Zone, structure is defined by a mixture of low magnetic susceptibility, moderate density Wirku Metamorphics, and higher magnetic susceptibility, high-density Pitjantjatjara Supersuite rocks that are dissected by several shallowly to moderately dipping shear zones. The gravity and magnetic signature indicates that most of these dip to the south, although the Fanny Fault (66 km) dips to the north. Conductivity contrasts in the magnetotelluric model relate to major lithological boundaries, although it is unclear whether this represents differing lithological properties or the influence of structures.

The northern section extends from the Walpa Pulka Zone into the Mulga Park Zone, and is characterized by a series of south-dipping thrust slices associated with activity on the Woodroffe Thrust. In the Walpa Pulka Zone, these interleave high-susceptibility, high-density Pitjantjatjara Supersuite granites with the lower susceptibility, lower-density Wirku Metamorphics, although outcrop on the profile trace is dominated by Pitjantjatjara Supersuite. The Woodroffe Thrust is demarcated here by series of thrust sheets extending 12–29 km along the profile, although the main boundary lies at 24 km, where high density Walpa Pulka basement rocks are thrust over lower density Mulga Park basement rocks.

The Woodroffe Thrust itself has no apparent electrical signature, although its trace may be indicated by the truncation of overlying anomalies. These anomalies are shown to be robust features of the MT model (Fig. 15) and may represent subvertical structure that exists in both the hanging wall and footwall of the Woodroffe Thrust. To the north of the Woodroffe Thrust, a ~5-km-thick sequence of low-density but variably magnetic sedimentary rocks overlie non-magnetic basement of relatively low density (2680 kg/m^3). In the magnetotelluric model, these may be indicated by a shallow, flat conductor of similar thickness. Upright, open folding of these sedimentary rocks is indicated by a subtle fabric in the magnetic data, and crustal thickening is required to explain the deep gravity low. These structures are interpreted to represent deformation related to the development of thrust faults (e.g. Wankari Detachment Zone – WDZ) in the footwall of the Woodroffe Thrust during the Petermann Orogeny, as documented in the Northern Territory (Edgoose et al., 2004; Flöttmann et al., 2005). However, overall shortening here is much less than in the NT, where more than 100 km of shortening is estimated (Flöttmann et al., 2005).

Profile 6 (Figure 28)

This profile traverses the province from south to north, covering similar features to profile 4, but going through the Blackstone Syncline more directly, and covering the northern Tjuni Purlka Zone. This profile indicates that the Officer Basin (0–24 km) contains fairly dense (2630 kg/m^3), low-susceptibility sedimentary rocks, which dip gently to the south and are essentially undeformed, except for a monoclinal upturn. The upper Bentley Supergroup is not present here, but the Officer Basin is underlain by highly magnetic and dense Kunmarnara Group volcanic rocks. These rocks are apparently folded in a broad antiformal structure with an axis at ~30 km. Gravity data suggest that these dense volcanic rocks extend beneath the Wankanki Supersuite for some distance, indicating reverse motion on a shallowly northwest-dipping fault at the basin margin (F1), although this is cut by a steeply south-dipping fault (F2). The low-susceptibility, low-density Tollu granite (46–59 km) is characterized by shallowly north-dipping tabular geometry and a total thickness of ~5 km. The intrusion is surrounded by a prominent magnetic aureole, interpreted to represent altered Wankanki Supersuite rocks.

The gravity low of the Tollu granite is superimposed on a steep gradient, indicating that the Blackstone intrusion extends below the northern part of Tollu granite, but is truncated beneath the granite at MZ_F3. As discussed for profile 3, this likely reflects control on the igneous intrusions by a long-lived structure. Strong remanent anomalies immediately north of the Tollu granite indicate deformed Giles Suite rocks similar to those at the base of the Cavenagh intrusion (Fig. 26). Remanent magnetization of 3 A/m, inclination of –75°, and declination of 164° fits the RTP anomalies well.

Outcrop between 59–67 km is dominated by the rhyolites and andesites of the Tollu Group, which includes the Smoke Hill Volcanics and the overlying Hogarth Formation, although sills of the Alcurra Dolerite have intruded into the stratigraphy. The deformation of these

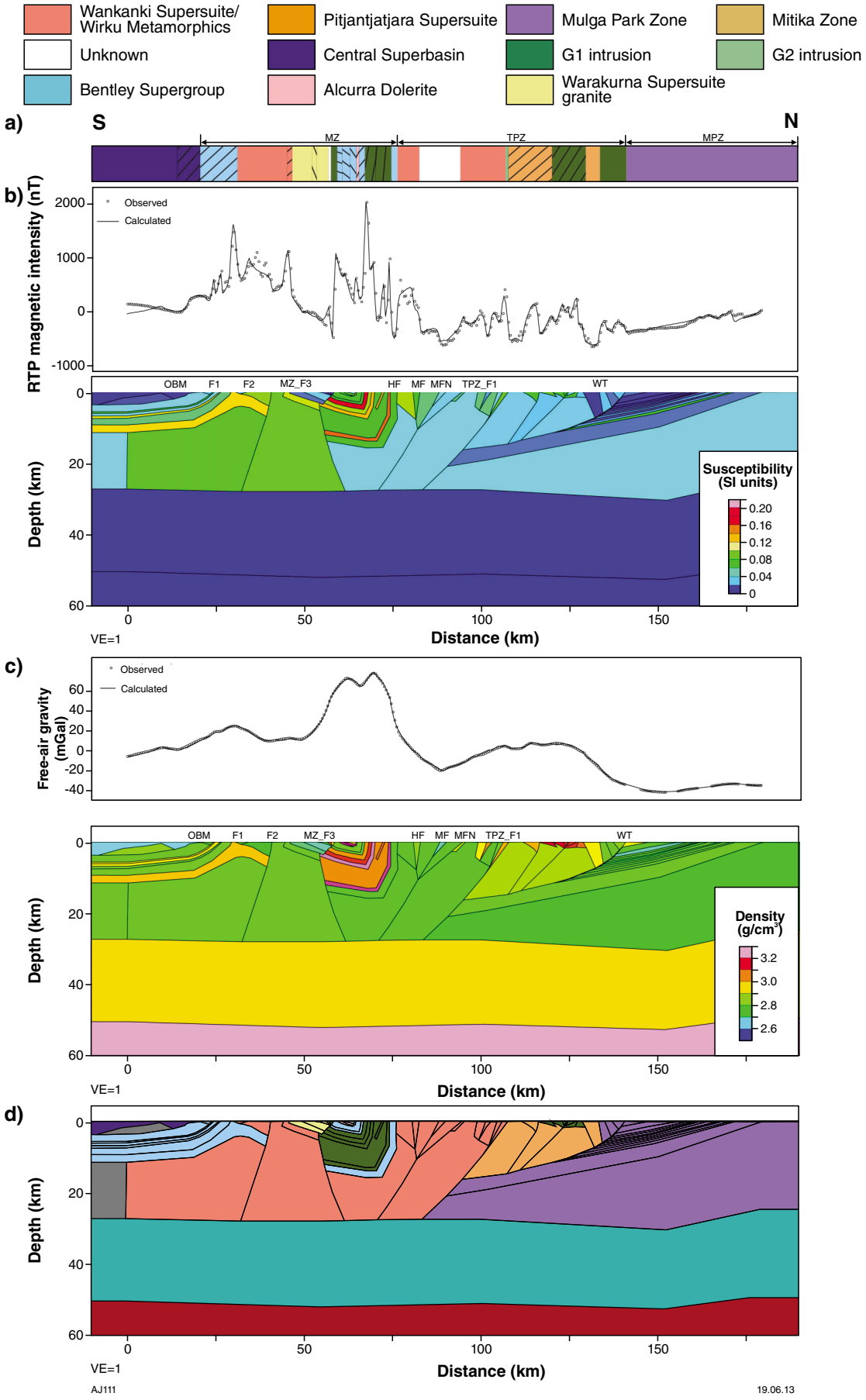
Wankanki Supersuite/ Wirku Metamorphics
Pitjantjatjara Supersuite
Mulga Park Zone
Mitika Zone
Unknown
Central Superbasin
G1 intrusion
G2 intrusion
Bentley Supergroup
Alcurra Dolerite
Warakurna Supersuite granite
a)
S
N
MZ
TPZ
MPZ
b)
RTP magnetic intensity (nT)
Observed
Calculated
OBM
F1
F2
MZ_F3
HF
MF
MFN
TPZ_F1
WT
Depth (km)
Susceptibility (SI units)
Distance (km)
VE=1
c)
Free-air gravity (mGal)
Density (g/cm3)
d)
AJ111
19.06.13

Figure 28. (facing) Joint magnetic and gravity model along profile 6 (see Fig. 2a for location) showing: a) interpreted geology; b) magnetic susceptibility; c) density distributions; d) interpreted geological fit to magnetic and gravity data. See Figure 23 caption for other details. This profile shows the Blackstone Syncline in more detail, the steeply dipping structure of the Northwest Tjuni Purlka and the shallowly south-dipping Tjauwata group in the Mulga Park Zones.

units, along with the Blackstone intrusion, define the Blackstone Syncline, resulting from mid-Giles Event age deformation (Evins et al., 2010; Joly et al., 2013). The Blackstone Syncline is a fold with an axial trace at 66 km. The southern limb of the fold dips shallowly northwards, and the northern limb of the fold dips steeply southwards, indicating an axial planar inclination of ~50° north. In aeromagnetic data, truncations of beds within the core of the syncline indicate minor thrust faulting (Joly et al., 2013). In this model, structural thickening of a sill of the Alcurra Dolerite is required to satisfy the gravity anomaly, and total throw is estimated at 1 km.

As with the other profiles, crustal structure within the Tjuni Purlka Zone is dominated by steeply dipping, planar shear zones, most of which dip to the south. These include the Hinckley Fault, the Mann Fault, and the Mann Fault North. However, the primary shear zone here is TPZ_F1, which is encountered at 107 km. North of TPZ_F1, crustal structure resembles the Walpa Pulka Zone, with dense Pitjantjatjara Supersuite and Giles Suite rocks above a shallowly south-dipping Woodroffe Thrust. Although extensive, the Lehmann Hills Giles Suite intrusion (G1) (115–130 km) is quite thin (<2 km) and is dissected by several fault zones. The Woodroffe Thrust approaches the surface at 141 km. However, between 134 and 141 km, the rocks are of much lower density than the basement rocks to the south, and also dip the opposite way. These are interpreted as Tjauwata Group sedimentary rocks entrained in the hanging wall of a foreland-propagating Woodroffe Thrust. Unfortunately, there is no outcrop with which to constrain this interpretation. North of the Woodroffe Thrust, crustal structure is characterized by crustal thickening under a fairly thick pile (>10 km) of shallowly south-dipping, undeformed, Tjauwata Group rocks. Beneath these rocks, the crust is modelled with a relatively low density (2725 kg/m^3) and thickened by ~5 km.

Profile 7 (Figure 29)

This profile traverses the southeast Tjuni Purlka Zone, the Walpa Pulka Zone and the Mulga Park Zone, with the aim of investigating the architecture of the Petermann Orogeny, which affected this area most strongly (e.g. Joly et al., 2013). In particular, investigations in South Australia indicate the presence of significant crust–mantle boundary offsets accommodated on the major shear zones (Lambeck and Burgess, 1992; Aitken et al., 2009a; Aitken et al., 2009b; Korsch and Kositcin, 2010), and it is important to determine if these continue into Western Australia.

The Officer Basin and Bentley Supergroup in this profile have similar structures to those in the western part of the Province; they are essentially undeformed, except for a monoclinal upturn. The Kunmarnara Group is thinner than in profile 5, and overlies granitic rocks interpreted in GSWA mapping as Warakurna Supersuite granites. These rocks may form part of a large batholith, characterized by an oval magnetic low that extends into South Australia (Fig. 2a). In South Australia, the Wintiginna Lineament delineates one of the major shear zones that may bound a wedge of mantle that has been uplifted into the crust (Aitken et al., 2009a). This structure continues into Western Australia as a prominent northwest-trending shear zone, which is associated with approximately 14 km of apparent dextral offset of the Bell Rock intrusion relative to the Blackstone intrusion (see Joly et al., 2013). Dip-slip offset is poorly constrained, but is probably low, based on the continuity of the Bell Rock and Blackstone intrusions across this structure. These intrusions are both subvertical, however, so several kilometres of dip-slip offset may be possible without disrupting this apparent continuity.

At the location of the profile, the Wintiginna Lineament consists of two splays (Fig. 2): one juxtaposing granite of the Warakurna Supersuite against low-density, low-susceptibility Bentley Supergroup rocks (contact at 24 km), and the other juxtaposing the Bentley Supergroup against high-density, high-susceptibility Pitjantjatjara Supersuite (contact at 31 km). The gravity data require high-density basement rocks below the Bentley Supergroup (2830 kg/m^3). Both the Bentley Supergroup and the Pitjantjatjara Supersuite are exposed in a few small outcrops, and each of these units has a steeply northeast-dipping foliation, (Smithies et al., 2009b), which may indicate the geometry of the Wintiginna Shear Zone. Magnetic layering in the Pitjantjatjara Supersuite is consistent with this, and the gravity gradient is satisfied by a steeply northeast-dipping planar geometry for the Wintiginna Lineament.

The Mount West Shear Zone (MW at 38 km) juxtaposes the Pitjantjatjara Supersuite rocks against the Latitude Hills intrusion (G1). Although not outcropping here, this second-order shear zone outcrops at Mount West, where it is characterized by a mylonite zone that juxtaposes foliated Pitjantjatjara Supersuite against the non-metamorphosed Bell Rock intrusion (G1). Foliations within the granite and the mylonite zone typically dip steeply to the northwest.

The conjoined Latitude Hills and Michael Hills G1 intrusions (40–57 km) are characterized in the aeromagnetic data by very strong anomalies that show clear fold geometries, indicative of north-inclined open folding of mid-Giles Event age (Evins et al., 2010; Joly et al., 2013). In the gravity and magnetic model, this folded geometry is necessary to explain asymmetric magnetic anomalies and short wavelength undulations in the gravity anomaly, and is consistent with dip reversals in outcrop data. Furthermore, modelling indicates that the base of this intrusion is not flat, but dips to the south at ~12°. Preserving the thickness of the upper crust, the upper crust – lower crust boundary is also interpreted to dip south at the same angle (Fig. 29), although this is not required by the gravity data.

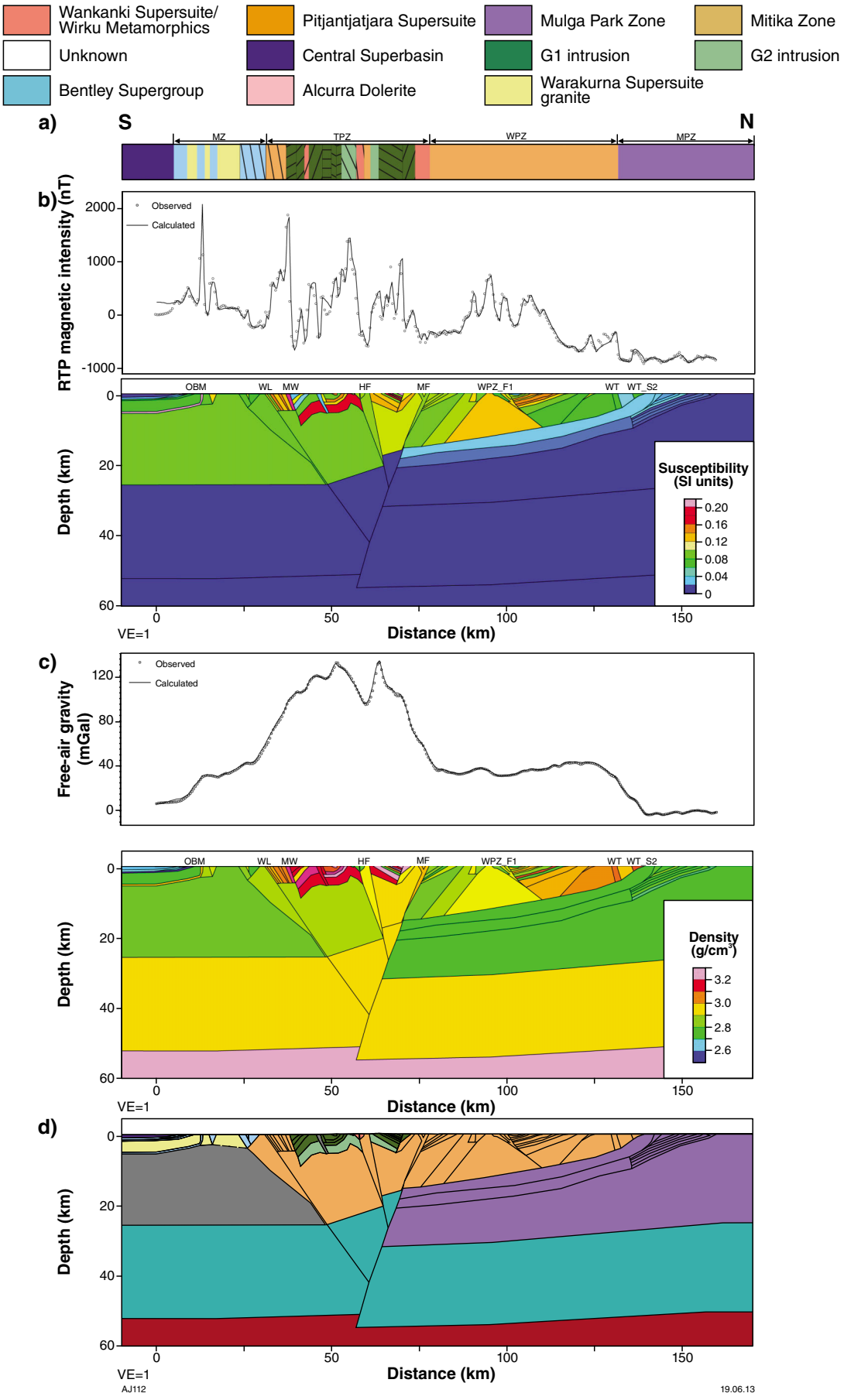
Wankanki Supersuite/ Wirku Metamorphics
Pitjantjatjara Supersuite
Mulga Park Zone
Mitika Zone
Unknown
Central Superbasin
G1 intrusion
G2 intrusion
Bentley Supergroup
Alcurra Dolerite
Warakurna Supersuite granite
a)
S
N
MZ
TPZ
WPZ
MPZ
b)
RTP magnetic intensity (nT)
Observed
Calculated
OBM
WL
MW
HF
MF
WPZ_F1
WT
WT_S2
Depth (km)
Susceptibility (SI units)
0.20
0.16
0.12
0.08
0.04
0
VE=1
Distance (km)
c)
Free-air gravity (mGal)
Density (g/cm3)
3.2
3.0
2.8
2.6
d)
AJ112
19.06.13

Figure 29. (facing) Joint magnetic and gravity model along profile 7 (see Fig. 2a for location) showing: a) interpreted geology; b) magnetic susceptibility; c) density distribution; d) interpreted geological fit to magnetic and gravity data. See Figure 23 caption for other details. This profile highlights the structure of the Petermann Orogeny, including the tilting of Giles Complex plutons, significant offset on the Mann Fault, and shallow-dipping structure within the Walpa Pulka Zone.

The Michael Hills intrusion is truncated to its north by the Hinckley Fault Zone (57 km). This fault zone outcrops and has been mapped in detail (Glikson et al., 1995). Geological studies suggest that it preserves significant post-Giles-intrusion activity on several generations of mylonite and pseudotachylite zones. This includes southeast-directed dextral reverse motion on E–W shear zones (D4), southwest-directed dextral reverse motion on north–south-trending shear zones (D5), south-up reverse motion on a south-dipping shear zone (D6), and north-up reverse motion on north-dipping retrograde shear zones (D7) (Glikson et al., 1995).

At the scale of the model, this structure is characterized by a major north-dipping feature demarcated by a transition to extremely dense crust (2890 kg/m^3) that occupies the region between the Hinckley Fault and Mann Fault. The moderately north-dipping Hinckley intrusion (G1) is immediately to the north of the Hinckley Fault. The offset between the base of this intrusion and the base of the Michael Hills intrusion indicates approximately 3 km of north-up reverse offset across the Hinckley Fault Zone, assuming these layers were originally continuous. Although a fault lies between them, the Hinckley intrusion (G1) is connected to the Wingellina Hills intrusion (G1), which dips steeply to the south.

The Mann Fault is demarcated by a zone of low magnetic intensity, and a transition from very high to lower gravity values. This fault zone dips steeply to the south and, in this model, is associated with ~10 km of south-side-up displacement. Although this displacement and the resultant slope to the upper-crust – lower-crust boundary are not required by the gravity field, they are strongly suggested by the slope of the base of the layered Giles Suite intrusions, and the interpreted ~3 km offset on the Hinckley Fault. This slope is further constrained by the >2 kbar difference in emplacement (or perhaps burial) level between the Blackstone intrusion (<4 kbar; Glikson et al., 1995) and the Wingellina Hills intrusion (6 ± 1 kbar; Ballhaus and Berry, 1991), suggesting at least 6 km of relative exhumation.

Immediately north of the Mann Fault, the crust is thick (55 km) and not especially dense (2790 kg/m^3) or magnetic (~ 8000 x 10^{-5} SI units). Structures are generally south-dipping, until the north-dipping WPZ_F1 is reached (95 km). The footwall to this shear zone is occupied by magnetic (11000 x 10^{-5} SI units), dense (2860 kg/m^3) Pitjantjatjara Supersuite granite. The hanging wall is also occupied by highly magnetic (11 000 – 13 000 x 10^{-5} SI units) Pitjantjatajara Supersuite, with prominent south-dipping layering. Although these rocks are generally lower density (2800 kg/m^3) than those in the footwall, some layers are higher density (3000 kg/m^3). From 117 km to the aeromagnetically interpreted Woodroffe Thrust (WT), rocks are very high density (2950–3050 kg/m^3), but lower susceptibility (6000 x 10^{-5} SI units). The gravity data suggest that the boundary between dense Walpa Pulka Zone crust and low density Mulga Park Zone crust actually occurs on the northern splay of the Woodroffe Thrust (WT_S2).

As in the other profiles, the Woodroffe Thrust is a shallowly south-dipping structure that underlies the Walpa Pulka Zone, merging into the Mann Fault at ~15 km depth. Beneath the Woodroffe Thrust, the Mulga Park Zone crust is low density (2695 kg/m^3) and very low susceptibility (0 x 10^{-5} SI units). Magnetic layering in the footwall of the Woodroffe Thrust is inferred to reflect the southerly dip of Tjauwata Group rocks.

Summary of forward modelling results

The series of profiles across the west Musgrave Province highlight the different character and structure of each major tectonic zone (Fig. 1.). The Mamutjarra Zone is dominated by abundant Warakurna Supersuite rocks, and by crustal structure derived primarily during the c. 1085–1045 Ma Giles Event. The basic crustal structure is typified by shallowly southwest- to south-dipping geological layering, which includes the Jameson intrusion and much of the Bentley Supergroup. Profile 1 presents a near complete section across a relatively undisturbed part of this stratigraphy, and this model indicates that at least 30 km of material was intruded into or erupted onto the crust during the Giles Event. This estimate includes the thickness of the Jameson intrusion (8 km thick) and Winburn granite (6 km thick), and the preserved thickness of the Mount Palgrave, Cassidy, and Mission Groups, each approximately 5 km thick. This estimate does not include the Pussy Cat or Kunmarnara Groups, the thicknesses of which are undefined.

However, this layered structure has been disrupted by several phases of deformation, especially in the region east of the Cavenagh Fault. This deformation includes folding of the Blackstone–Cavenagh intrusion and the overlying Tollu Group (Figs 27 and 28), and dissection of the region by numerous faults, principally normal faults active during the late Giles Event (Joly et al., 2013). Some of these 'late Giles' age faults demonstrate control on the emplacement of Giles Suite (G1) intrusions and Warakurna Supersuite granites, indicating activity throughout the Giles Event.

The Tjuni Purlka Zone is characterized by abundant shear zones, and the dominance of basement rocks, with rocks of the Warakurna Supersuite making up a minor component. This region can be separated into two regions — the northwest Tjuni Purlka zone, and the southeast Tjuni Purlka Zone. In the northwest Tjuni Purlka Zone, the structure is characterized by steeply dipping shear zones within relatively high-density, low-susceptibility basement rocks. These shear zones are mostly interpreted to be the same age as the Petermann Orogeny, although they may

reflect reactivation of Giles-age or even older structures (Smithies et al., 2011; Joly et al., 2013). Although not as extensive as in the Mamutjarra Zone, several outcrops of Giles Suite intrusions are observed throughout the region. Gravity and magnetic modelling indicate that these may form part of a larger intrusion that has subsequently been eroded and dissected by faulting. The preserved thickness of this intrusion is 2–5 km (Fig. 28). Also within this zone, the Murray Range preserves a significant intrusive complex of massive gabbro (G2). Modelling suggests that this fault-bounded region dips moderately to the west, meeting with the Mann Fault (Fig. 27) or TPZ_F1 (Fig. 23) at depth.

The structure of the southeast Tjuni Purlka Zone is dominated by the architecture of Petermann Orogeny shear zones. This region contains several large Giles Suite intrusions that can be used to constrain the Petermann Orogeny architecture (Fig. 29). The Wintiginna Lineament, Hinckley Fault, and Mann Fault are steeply dipping crustal-scale faults. These define the limits of an 80 mGal gravity high, which indicates dense crust that may have been exhumed from depth during the Petermann Orogeny. Although dip-slip offset on the Wintiginna Lineament is probably quite small, the geometry of the Latitude Hills and Michael Hills intrusions indicate that crust to the north of the Wintiginna Lineament has been tilted at an angle of ~12°. This tilting, plus an apparent offset of 3 km to the base of the layered Giles Suite intrusion on the Hinckley Fault, indicates that the Mann Fault has accommodated approximately 10 km of south-side-up reverse offset.

The Walpa Pulka Zone is characterized by high-pressure (10–14 kbar) metamorphic basement that has been exhumed from great depths during the Petermann Orogeny (Scrimgeour and Close, 1999; Raimondo et al., 2010). The structure of this region is defined by intercalation of Pitjantjatjara Supersuite with the Wirku Metamorphics. Pitjantjatjara Supersuite rocks are typically very dense, and typically have high magnetic susceptibilities, whereas Wirku Metamorphics rocks are less dense, and are also generally less magnetic. Structures in this zone are typically shallow-dipping, and south-dipping structures predominate, merging into the basal detachment of the Woodroffe Thrust at depth. However two major faults (the Fanny Fault and WPZ_F1) dip steeply to the north. The thickness of this thrust sheet is variable, but the models suggest that it merges into the Mann Fault or TPZ_F1 at approximately 15 km depth.

Beneath the Woodroffe Thrust, the Mulga Park Zone is characterized by low-density, low-susceptibility crust. This crust is overlain by layered sedimentary–volcanic sequences 5–12 km thick, which are thought to belong to the Tjauwata Group, although outcrop is poor. Despite its position above the Woodroffe Thrust, the Mitika Zone has similar geophysical character to the Mulga Park Zone, although the interpreted thickness of the Tjauwata Group is less (0–5 km), perhaps reflecting uplift by reverse motion on the Woodroffe Thrust.

3D modelling and inversion

3D model building

A 3D model of the west Musgrave Province was constructed with the aim of: 1) improving visualization of crustal structure, and 2) providing an initial model for 3D geophysical inversions, through which crustal structure can be validated in 3D. In MGA 94 Zone 52 coordinates, the model extends from 260000 to 560000 mE (300 km) in X, and from 7000000 to 7290000 mN (290 km) in Y (Fig. 30). In Z, the model extends from the Earth's surface to 75 km depth below the geoid.

Methods

This model was constructed from the geological data, the forward modelled cross sections, and the magnetotelluric profiles. To construct the model we considered firstly the architecture of major faults and shear zones, and secondly, the nature of lithological boundaries within these fault-bounded blocks.

Fault network

The major fault zones used for the model are generated using a simplified version of the fault maps presented in Joly et al. (2013) (Fig. 2). These faults are separated into planar or listric geometry, based on their interpreted geometry in the upper crust (Figs. 23 to 29). These models suggest that a planar geometry is acceptable over the observed length of most faults south of the Woodroffe Thrust. The Woodroffe Thrust and the shear zones to its north typically have listric geometries (Edgoose et al., 2004).

In the model, the traces of planar faults are projected down-dip. Approximate dip and dip direction were derived from the forward models (Figs 23 to 29). For faults not crossed by these profiles, the dip and dip direction were inferred from geological data, including WAROX data, stratigraphic considerations, and the style of deformation adjacent to the fault. The inversion software used (VPmg™) can only modify the depths to boundaries that are already present within the initial column stratification. This means that the inversion software has greater capability to steepen over-shallow dips than it has capacity to shallow out over-steep dips. Because of this, interpreted dips for modelling are at the shallow end of that suggested by the input data (Table 5).

With the exception of the Woodroffe Thrust, listric faults are constructed in three sections. The first section dips at approximately the angle suggested by near-surface geological data, and typically has a length of 10 km (Table 5). The second segment has a shallower dip, and a segment length of 20 km, and the final segment has

Table 5. Fault geometry definition parameters. Faults are separated into planar and listric categories. Dip and dip-direction are derived from a combination of geological data, and the geometries observed in gravity magnetic and magnetotelluric profile modelling.

Planar Faults						
Fault name	*Dip direction*	*Dip (°)*				
TPZ_F1	200	60				
TPZ-F2	115	50				
HF	15	60				
MFN	200	60				
MF	190	60				
MR_east	255	40				
MR_west	255	40				
FF	40	60				
WPZ_F1	40	60				
WPZ_F2	350	30				
WHL	20	50				
WL	30	60				
MZ_F5	340	70				
MZ_F3	0	60				
CF	330	50				
MZ_F4	335	60				
TPZ-F3	30	50				
WF	255	60				
MZ-F1	25	60				
MZ_F2	25	60				
Listric Faults						
Fault Name	*Dip direction*	*Dip1 (°)*	*Dip2 (°)*	*Dip3 (°)*	*L1*	*L2*
BZ	350	20	5	0	10	20
PDZ	315 – 30	30	15	5	10	20
PDZ_WA	345	30	15	5	10	20
WDZ	180	30	15	5	10	20
WT	From models	–	–	–	–	–
WT_S1	From models	–	–	–	–	–
WT_S2	From models	–	–	–	–	–
WT_S3	From models	–	–	–	–	–

very shallow dip (<5°), and extends either until it is truncated by another structure, or reaches the edge of the model space. The Woodroffe Thrust and its splays are constructed differently because they are intersected by most of the forward models, and their geometry can therefore be defined directly from these models. In doing this, the geometry of the Woodroffe Thrust on each profile is extrapolated along strike, defining the geometry of the fault zone within a particular segment (Fig. 30).

Once the fault geometries were defined, the crosscutting relationships between faults were defined (Table 6). Although the crosscutting relationships observed in the near surface were the primary criterion for this, the length scale of the fault was also considered. Where faults meet only at depth, the crosscutting relationship was defined first by the interpreted ages of the faults, and then, if these are the same, by the scale of the fault.

Lithological boundaries

For the model construction, lithological boundaries were divided into two main categories: layered units and plutons. These units were superimposed on fault-bounded basement blocks. Basement blocks are either Wankanki Supersuite dominated or Pitjantjatjara Supersuite dominated, and were assigned the properties of the relevant lithology. The distribution and geometry of the Wirku Metamorphics at depth is difficult to define, so they were included within these basement units.

Layered Units

Layered units are those that can be described by an extensive surface that is fault-bounded, cut by the Earth's surface, or extends to the edge of the model area. These include the Bentley Supergroup and the overlying Centralian Superbasin, the major Giles Suite (G1) plutons (Jameson, Blackstone, Cavenagh, Bell Rock intrusions), and the stratiform Winburn granite. The boundaries between these layers at the surface (Fig. 30) were defined from geologically constrained magnetic/gravity interpretation. As with the faults, the geometry of these surfaces was inferred from a combination of geological data and the forward models. In many cases, a listric geometry is preferred (Table 7) to satisfy the structure imaged in the forward models. For example, the Jameson intrusion, Winburn granite, and Mount Palgrave Group boundaries have moderate to steep dips at the surface (Fig. 30), but have an overall dip of 20º to the southwest at depth.

The more complex geometries of the units involved in the Blackstone Syncline are derived directly from the forward models. As with the Woodroffe Thrust, these model profiles were extrapolated along strike (and up-plunge or down-plunge) to the point where they are truncated by the Wintiginna Lineament and the Cavenagh Fault. The structure of the Officer Basin is revealed in

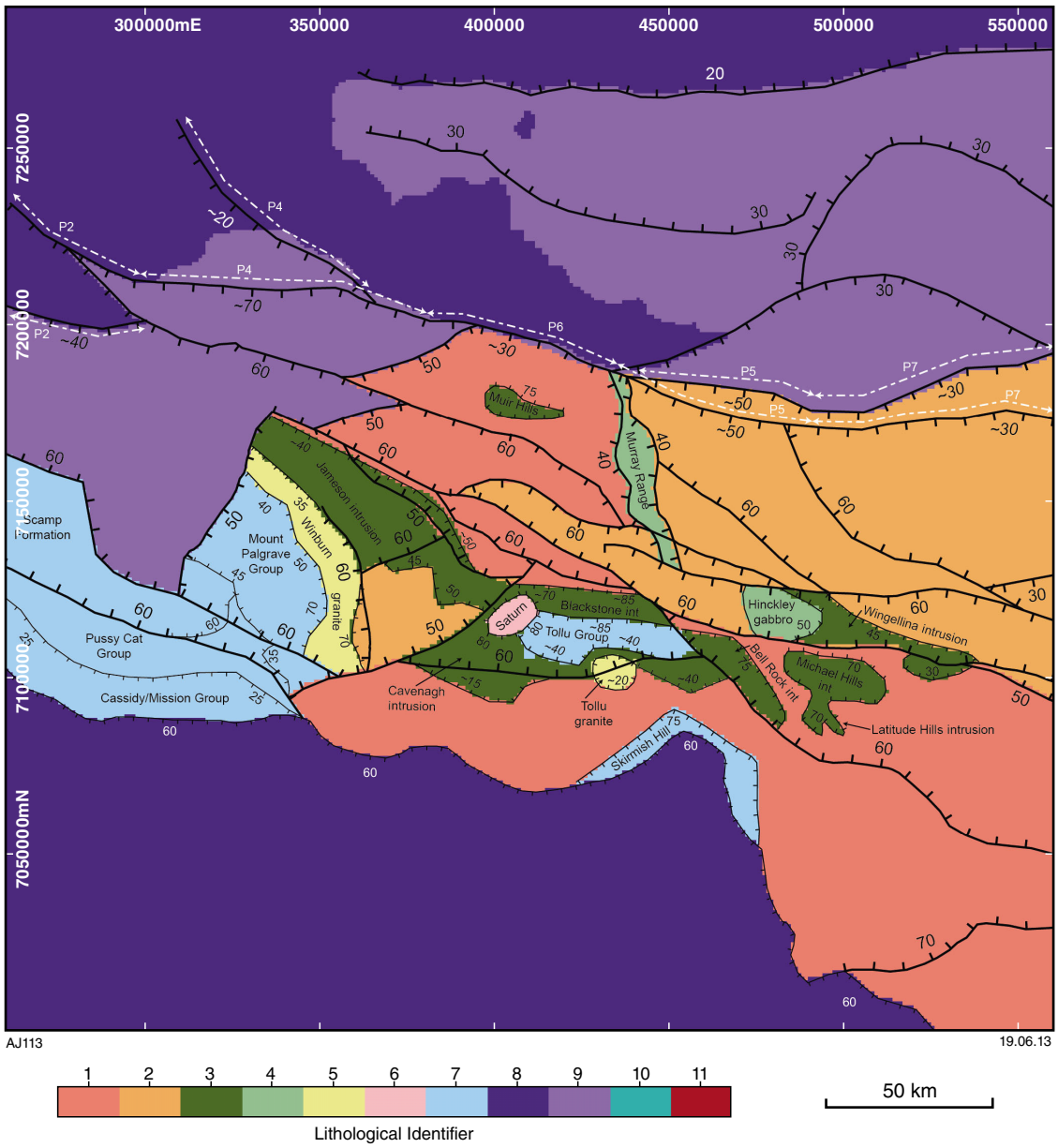

Figure 30. Plan view of the 3D model, showing the near-surface (Z = 0) distribution of lithological units, and the dips of faults (heavy lines) and lithological boundaries (lighter lines). Where dip is in italics, this indicates that the geometry of the feature was derived from the forward models, so these are approximate estimates of the dip at the near surface. For the Woodroffe Thrust and its splays, the relevant profile for each section is labelled P1–P7 (white dash–dot lines). See Tables 5 and 7 for more information on the definition of structures at depth.

Table 6. Fault cutting relationships. These are based on relative age and the scale of the fault, as well as relations observed in gravity magnetic and magnetotelluric profile modelling. Refer to Figure 2 caption for fault name abbreviations

Fault	*Fault cuts*	*Fault cut by*
TPZ_F1	WT_S1, TPZ_F2, WT, MR, HF	MFN
TPZ_F2	None	WT, TPZ_F1, HF, MZ_F1, CF
HF	TPZ_F2, TPZ_F3, CF, WL, MFN	TPZ_F1, MF
MFN	TPZ_F1, HF, WT	HF, MF
MF	WPZ_F1, WPZ_F2, FF, MFN, HF, WT, MR	None
MR	FF	WT, MF, TPZ_F1, HF
FF	None	MR, MF, WT
WPZ_F1	WPZ_F2	WT, MF
WPZ_F2	None	WT, WPZ_F1, MF
WHL	None	HF, MF
WL	MZ_F3, MZ_F5	HF, MF
MZ_F5	None	WL, MZ_F2
MZ_F3	None	WL, CF, MF, MFN, TPZ_F1
CF	TPZ_F3, MZ_F3, WF, TPZ_F2	HF, MZ_F2, TPZ_F1
MZ_F4	None	TPZ_F3, TPZ_F1, WF, TPZ_F2
TPZ-F3	MZ_F4	CF,HF,
WF	MZ_F4	CF, TPZ_F2, MZ_F1
MZ_F1	TPZ_F2, WF, WT_S1	TPZ_F1, CF
MZ_F2	CF, MZ_F5	TPZ_F1
BBZ	None	None
PDZ	None	WDZ
PDZ_WA	None	None
WDZ	PDZ, WT_S2	WT
WT	WT_S3, TPZ_F2, MR, WDZ, FF, WPZ_F1, WT_S2, WPZ_F2	TPZ_F1, MFN, MF
WT_S1	none	TPZ_F1, MZ_F1
WT_S2	None	WDZ, WT
WT_S3	None	WT

the forward models, and these were used to constrain a listric model geometry involving a steeply south-dipping margin that rotates over a short distance to flat-lying (Table 6). The Amadeus and Canning Basins are not included in the forward models, except in isolated areas, so for these basins we apply the basin geometry derived from the SEEBASE project (FrOG Tech Pty Ltd, 2005). In addition to these upper crustal layers, an upper-crust – lower-crust boundary and crust–mantle boundary are included. These are primarily flat layers at 25 km and 50 km depth, respectively. However, a northwards slope of ~12º is included between the Wintiginna Lineament and Mann Fault, based on the interpreted structure in profile 7 (Fig. 29).

Plutons

Five plutons are included to describe those features that cannot easily be defined as fault-bounded layers. These are the Tollu granite, Saturn gabbro, Hinckley gabbro (G2), Muir Hills intrusion (G1), and the Latitude Hills/Michael Hills (G1) intrusions. The geometry of the Tollu granite was defined from the model profiles that cross this pluton (Figs 25 and 28). These indicate a disc-like geometry, with a shallowly north-dipping base and steeply dipping sides. The margins of the other plutons were defined by tube-like extensions of their surface boundaries. Dips were defined by the interpreted dips of the pluton margins (Table 7). In the case of the Saturn gabbro, the dip of the boundaries was not defined by either forward modelling or WAROX data. The boundaries are probably steep, so these are shown as dipping outwards at an angle of 80º. The base of the pluton was set at 5 km depth. On the basis of WAROX data, the Hinckley gabbro (G2) is interpreted to dip north at approximately 50º, and its base was defined by the intersection with the Mann Fault. WAROX data suggest that the Muir Hills intrusion (G1) dips to the north at approximately 75º. The thickness of this pluton is unknown, but was set at 5 km in this model. Profile 7 indicates that the boundaries of the Michael Hills and Latitude Hills intrusions dip steeply to the north (70º), and that the bases of these plutons dip shallowly to the south (12º), with an overall thickness of ~10 km in the south and ~6 km in the north. The folded nature of the base of these plutons is not included in this model.

The model generated by the process above (Fig. 31) illustrates the likely 3D architecture of the events that

Table 7. Lithological boundary geometry definition parameters. Dip and dip-direction are derived from a combination of geological data, and the geometries observed in gravity magnetic and magnetotelluric profile modelling. See Figure 2 caption for fault name abbreviations. Dash (–) indicates no data

Lithological boundaries – layers						
Name	*Dip direction*	*Dip1 (°)*	*L1*	*Dip2 (°)*	*L2*	*Dip 3 (°)*
Jamieson intrusion	From models	–	–	–	–	–
Bell Rock intrusion	230	75	–	–	–	–
Blackstone–Cavenagh Int.	From models	–	–	–	–	–
Hinckley intrusion (G1)	15	30	–	–	–	–
Wingellina intrusion	180	45	–	–	–	–
Winburn granite	250	35	10	20	–	–
Palgrave Group	250	40–70	5	20	–	–
Scamp Group	315	60	10	45	25	–
Cassidy Group	220	25	10	20	30	5
Tollu Group	From models	–	–	–	–	–
Skirmish Hill Volcanics	180	75	3	10	12	0
Officer Basin	180	60	2	10	12	0
Amadeus/Canning Basin	From Seebase	–	–	–	–	–
Plutons						
Name	*Dip direction*	*Dip1 (°)*	*L1*	*Dip2 (°)*	*L2*	*Dip 3 (°)*
Tollu granite	From models	–	–	–	–	–
Saturn gabbro	Outwards	80	5	–	–	–
Hinckley gabbro (G2)	0	50	–	–	–	–
Muir Hills	20	75	5	–	–	–
Latitude Hills/Michael Hills	30	70	6–10	–	–	–

have shaped the west Musgrave Province. However, by applying gravity and magnetic inversions to this model it is possible to: 1) test the validity of the model given petrophysical constraints, and 2) investigate possible alternative geometries.

Inversions

Inversion software and approach

Three-dimensional gravity and magnetic inversions were undertaken using VPmg software (Fullagar et al., 2008). This software has two main modelling modes that operate entirely independently: property optimization and geometry optimization. In each mode, the other parameter cannot change.

Property optimization seeks to reduce the potential field misfit by changing the density or susceptibility distribution within lithological units. Within this mode of inversion there are two options as to how the changes to the property are derived. 'Conventional' property inversion applies a least-squares approach. This approach, at least in principle, generates the smallest possible change to the properties required to achieve a particular misfit reduction. In this case, the initial objective is the smallest perturbation required to halve the chi-squared misfit (Fullagar, 1985; Fullagar, 2011). The alternative, 'stochastic' property inversion applies random perturbations to the data. These are accepted only if they produce a reduction in misfit, and if the resulting property population conforms to the expected property distribution. This property distribution is defined by two 'half-gaussian' curves centred at the initial value. One of these constrains higher values, using the upper property limit as the 99.85 percentile value (mean + 3 standard deviations), whereas the other constrains lower values, using the lower property limit as the 0.15 percentile value (mean – 3 standard deviations). This arrangement permits asymmetric property distributions to be modelled, but does not approximate log-normal or bimodal distributions well (Fullagar, 2011). The results from these two approaches differ in that the conventional approach typically generates smoothly varying property distributions, while the stochastic approach generates chaotic property distributions. They differ also in that the conventional approach will not necessarily generate a realistic property distribution, whereas the stochastic approach will honour the statistical distribution of the property.

Geometry optimisation seeks to reduce the misfit by altering the depth to lithological contacts. As with the conventional property inversion, the initial objective is the smallest perturbation required to halve the chi-squared misfit (Fullagar, 1985; Fullagar, 2011). Only vertical adjustments are permitted, so lithological units cannot

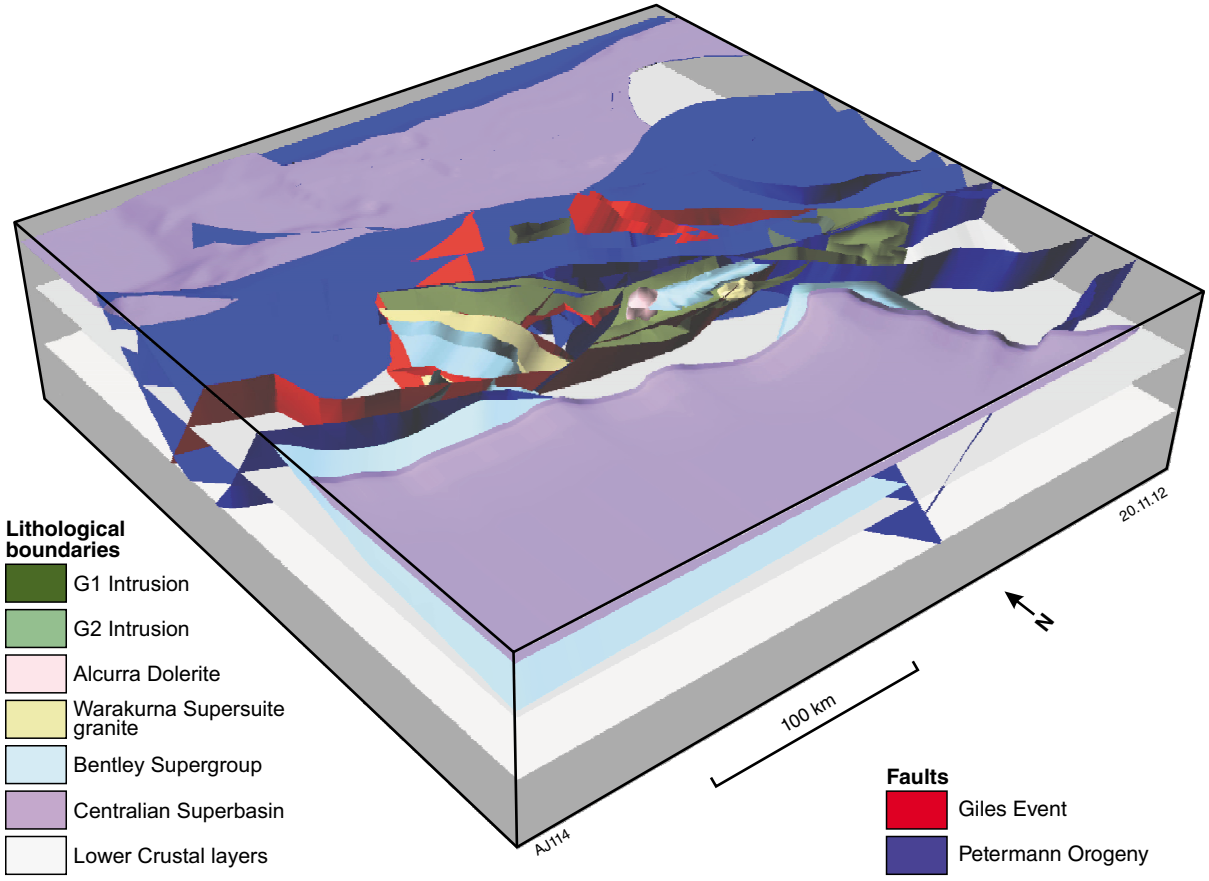

Figure 31. 3D view of the initial 3D model, showing the geometry of lithological units, Giles Event-age faults, and Petermann Orogeny-age faults. The box measures 76 km from top to bottom, 300 km from east to west, and 290 km from north to south. A 3D PDF of this model is included to aid visualization (see supplementary material on CD).

spread laterally beyond their initial extent. For this reason, the dips of boundaries in the initial model were at the shallow end of the range permitted. These surfaces can be constrained according to drillhole and seismic data, however neither set of data was available for this study.

Individual property or geometry inversions fail to deal with the fact that neither the initial geometry of lithological units, nor the distributions of properties within them are perfectly known. In situations where an initial model (other than a homogenous half-space) is proposed, it is useful to explore the relative capacity of property and geometry changes to reduce misfit, and to define how different inversion parameters affect the end result. Combined property–geometry inversion results can be achieved by applying sequential iterations of property and geometry. Using this balanced approach, many models can be generated that inhabit the space between the property-only and geometry-only end-members. From these, an estimate of the most likely model, and an estimate of model variability can be derived.

Model regularization procedures

As a result of the inherent non-uniqueness in potential field inversions (e.g. Parker, 1994), changes in density and structure must be controlled during inversion to guide the inversion towards a realistic result. In VPmg, hard constraints can be imposed by fixing absolute maximum and minimum limits on properties or by fixing the boundaries between lithological units in accordance with constraints from drillhole or seismic data. These constraints are achieved by truncation of the model perturbation vector (Fullagar, 2011).

Soft constraints can be applied by limiting the maximum change in density permitted per iteration or by limiting the maximum percentage change in interface depth per iteration. In property-only and geometry-only inversions, these constraints have some influence on the results, in that tighter limits will lead to more gradual changes. Generally, tighter constraints will lead to smoother results, but they may inhibit the capability of the inversion to reduce the misfit to the data. In contrast, in combined property–geometry inversions these per-iteration constraints are of prime importance. This is because they control the relative influence of property versus. geometry in reducing the misfit to the data. These per-iteration constraints are achieved by increasing the ridge regression parameter, leading to increased damping of the solution (Fullagar, 2011).

Magnetic inversions

Magnetic inversions were undertaken to assess whether the initial model can satisfy the magnetic field without violating susceptibility constraints. Two models were successfully applied: an 'unconstrained' conventional property inversion, and a lithologically constrained conventional property inversion. Attempts at stochastic property inversion were unsuccessful, probably due to the incompatibility of the log-normal statistical distributions observed in petrophysical data with the statistical distribution assumed by the inversion code. Property and combined property–geometry inversions were not attempted with magnetic data, because the variation of magnetic susceptibility within units is an order of magnitude greater than the difference in mean magnetic susceptibility between units (Table 8).

The unconstrained inversion result indicates the distribution of magnetic susceptibility that best satisfies the data, given minimal constraint, whereas the lithologically constrained inversion requires that the petrophysical constraints are satisfied within relevant rock units. This increased constraint causes a reduced capability to replicate the observed magnetic data.

Data processing for magnetic inversion

For inversion, it is critical that the data are processed appropriately to permit the model to generate a meaningful result. The steps undertaken here were reduction to the pole, upward continuation, and the blanking-out of remanent anomalies. Although reduction to the pole is not necessary for inversion, these inversions employed the merged reduced-to-pole aeromagnetic grid that was used for both forward modelling and interpretation (Fig 2a).

For inversion, it is extremely important that the wavelength content in the data is resolvable by the model. A useful rule-of-thumb is to upward-continue the data by half a cell width (Li and Oldenburg, 2003). Following this rule, the data were upward-continued by 500 m. Correspondingly, the nominal flying height was increased to 600 m above the ground surface for the calculation. In addition, the cell-size of the data grid must be well matched to the prism size of the model, with ideally a one-to-one ratio. Too few data points will lead to sub-optimal constraint on the model. Too many data points will lead to larger problem size and, more importantly, instability caused by the inability of the model to resolve misfit between multiple data points that overlie the same model prism.

Table 8. Lithological property parameters for gravity and magnetic inversion. Properties are derived from the petrophysical data where possible. Values in italics indicate values not constrained by petrophysical data.

Lithology	*LithID*	*Initial susceptibility*[(a)]	*Minimum susceptibility*[(a)]	*Maximum susceptibility*[(a)]	*Initial density*[(b)]	*Minimum density*[(b)]		*Maximum density*[(b)]	
Wankanki Supersuite basement	1	700	15	36 500	2730	C –2440	S – 2290	C – 3030	S – 3180
Pitjantjatjara Supersuite basement	2	300	1	66 600	2830	C – 2230	S – 1920	C – 3430	S – 3730
G1	3	600	5	59 000	3100	C – 2790	S – 2660	C – 3320	S – 3450
G2	4	600	7	55 000	2900	C – 2420	S – 2180	C – 3380	S – 3620
Warakurna Supersuite granites	5	200	0	130 000	2790	C – 2350	S – 2130	C – 3230	S – 3450
Saturn gabbro (Alcurra Dolerite)	6	900	27	27 000	2980	C – 2790	S – 2700	C – 3190	S – 3290
Bentley Supergroup	7	300	0	135 000	2750	C – 2480	S – 2350	C – 3030	S – 3160
Centralian Superbasin	*8*	*100*	*1*	*1 000*	*2450*	*C – 2200*	*S – 2200*	*C – 2700*	*S – 2700*
Mulga Park Zone/Mitika Zone Basement	*9*	*0*	*0*	*100 000*	*2700*	*C – 2450*	*S – 2200*	*C – 2950*	*S – 3200*
Lower crust	*10*	*NA*	*NA*	*NA*	*2900*	*NA*		*NA*	
Mantle	*11*	*NA*	*NA*	*NA*	*3300*	*NA*		*NA*	

NOTES: (a) SI units

(b) kg/m^3

Where it is known, the software can account for remanent magnetization, although it is not available as an inversion parameter. In any case, remanent magnetization within the rocks of the west Musgrave Province is not sufficiently well constrained to permit modelling in 3D. Because of this, large-amplitude magnetic anomalies thought to be dominated by remanent magnetization were excluded from the dataset (Fig. 32).

Initial models and inversion setup

The magnetic inversions were undertaken for the upper crust only. The model space involves a box with a base at 25 km, and 1-km by 1-km prisms extending from x = 259500 to 560500 mE (300 prisms) and y = 6999500 to 7290500 mN (292 prisms). Each prism is divided into lithological 'layers', the boundaries of which are precisely defined. For the unconstrained model, just one layer is defined, extending from the Earth's surface to 25 km depth. For the lithologically constrained model, prism layering is generated from the initial model (Fig. 31). Within each prism, each layer is further discretized using increasing cell size with depth. The first cell is 250 m thick, and the thickness of each subsequent cell is multiplied by 1.5 (i.e. 250, 375, 563 m, and so on). For the unconstrained model, this results in 10 cells per prism. The lowest of these has a thickness of approximately 8.5 km.

The initial model for the unconstrained inversion is occupied with a single lithology with susceptibility of 100 x 10^{-5} SI units. The permissible range of susceptibility was defined by minimum and maximum limits of –5000 x 10^{-5} SI units and 25 000 x 10^{-5} SI units respectively. The initial model for the lithologically constrained inversion is occupied with the nine lithologies in the 3D model described above. Each of these has an initial susceptibility that corresponds to the mean susceptibility of the unimodal model (either log-normal or normal) that best fits the petrophysical data. Unfortunately, bimodal distributions cannot be accommodated by the software. Minimum and maximum limits were defined by the mean ± 3σ for each unit (Table 8).

The magnetic inversions were run using the following restrictions. The maximum susceptibility change per iteration was 5000 x 10^{-5} SI units, and the maximum number of iterations was 200. Target misfit was 5 nT, which is slightly more than 1% of the initial misfit (~380 nT). Due to memory restrictions, the number of magnetic data points in the grid (approximately 90 000) was too large to perform inversion using the entire dataset. Instead of reducing the overall number of data, inversions were undertaken using only 50% of the dataset in each iteration. With this inversion option, the inversion software takes a random sub-sample of the data and uses it for a certain number of iterations (in this case, 16). Following this, a forward model is run, a new sub-sample is taken, and a new batch of iterations is run. This approach introduces the potential for changes in susceptibility in regions that are poorly constrained, due to a poorly distributed subset. However, later subsets should cover these areas, permitting any erroneous susceptibility changes to be rectified. This increased nonlinearity means that the process is less stable and less efficient. These drawbacks are offset by the capability to have a more detailed and better constrained model through the use of more data and smaller cell-size.

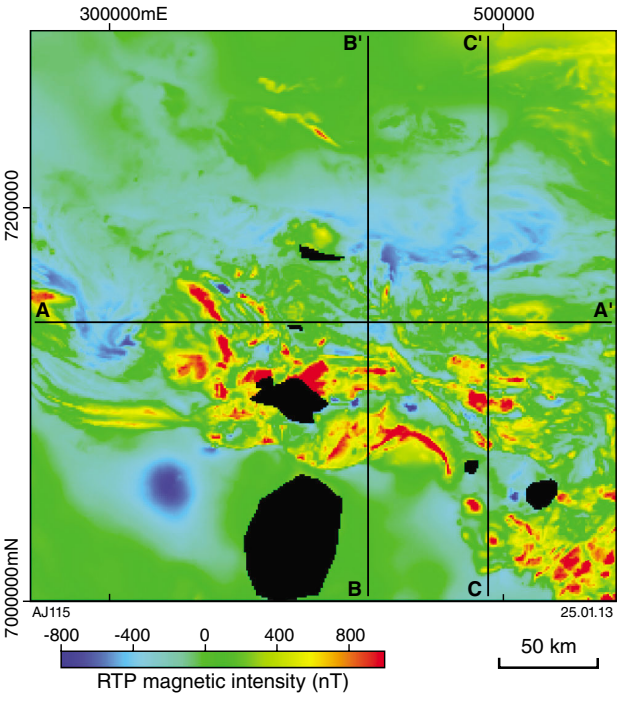

Figure 32. Magnetic data for inversion. Gridded data were reduced to pole, upward continued by 500 m, and resampled at 1 km spacing. Black areas indicate regions where strong remanent anomalies have been removed from the dataset. Lines A–A', B–B', and C–C' indicate the profiles shown in Figure 34.

Results

Unconstrained model

After 35 iterations, the unconstrained model achieved convergence. The remaining misfit (Fig. 33a) is dominantly short wavelength and relatively low amplitude. More significant misfits are focused at the margins of the Giles Suite, where magnetic gradients are especially steep.

Despite the lack of constraint, this model resolves many features quite well (Fig. 34). These include the contrast of the Mitika and Mulga Park Zone crust with higher susceptibility crust of the Mamutjarra, Tjuni Purlka and Walpa Pulka Zones. By virtue of this contrast, several structures are convincingly imaged, including TPZ-F2 (Fig. 34a) and the Woodroffe Thrust/Mann Fault (Fig. 34b,c). Within the Mamutjarra, Tjuni Purlka and Walpa Pulka Zones, many smaller features are imaged that are consistent with the interpreted geological model. However, few of these are particularly robust, and there are many features of the geological model that are unresolved. One that is quite robust is the imaging of the approximate geometry of the Blackstone intrusion and the overlying Tollu Group (Fig. 34).

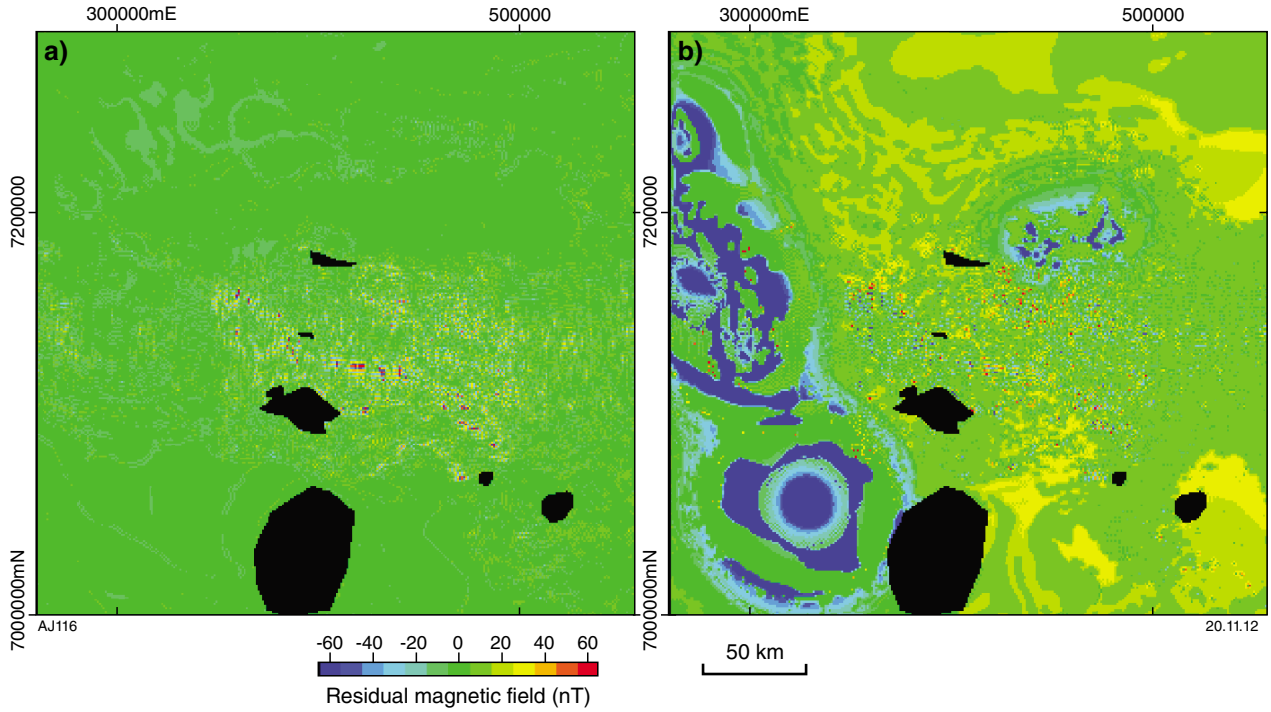

Figure 33. Magnetic modelling misfits showing: a) residual anomalies following the unconstrained magnetic inversion; b) residual anomalies following the lithologically constrained magnetic inversion. The prominent negative residual anomalies indicate the inability of this model to generate negative magnetic susceptibilities.

Lithologically constrained model

After 205 iterations, this model failed to achieve convergence, although misfit was reduced significantly to 42 nT (Fig. 33b). Although further iterations may reduce the misfit somewhat, the relatively high misfit for this model suggests that the initial model is not able to satisfy the magnetic field with current petrophysical constraints.

The remaining misfit (Fig. 33b) contains short-wavelength, low-amplitude oscillations similar to those in the unconstrained model result, but also contains large areas of strong negative misfit (i.e. where the calculated magnetic field is greater than the observed magnetic field). These relate to the inability of the lithologically constrained modelling to include negative susceptibility values in areas with very low magnetic field. In the context of this modelling, magnetic susceptibility is entirely relative, so the inability to fit the data likely results from initial susceptibilities that are too low. This may reflect the influence of weathering on the measured samples.

Despite the higher misfit in certain regions, this model shows a reasonably good fit to the data elsewhere. In particular, misfit is low in the central part of the area. The initial model is petrophysically acceptable in these regions.

The model results show that, by including the initial model, features that were not imaged or were poorly imaged in the unconstrained model were resolved. For example, the geometries of the Woodroffe Thrust, Mann Fault, and Hinckley Fault were imaged more clearly, and the magnetic anomalies associated with the Blackstone intrusion, Tollu Group, and Tollu granite have better defined geometries (Fig. 34b). Alternative geometries are suggested for some features; for example, in the third profile (Fig. 34c), there is a requirement for magnetic material beneath the Woodroffe Thrust that suggests either a near-vertical Mann Fault or a steeper Woodroffe Thrust.

Due to the better imaging of known structures, although they are non-unique solutions and despite the larger misfit, this model is preferred over the unconstrained model. Its 3D geometry is imaged in a fence diagram (Fig. 35).

Gravity inversions

As with the magnetic inversions, gravity inversions were aimed at establishing whether the initial model could satisfy the gravity field without violating petrophysical constraints. Here we apply four inversion schemes. Firstly, we used unconstrained conventional least squares property inversion (as used in the magnetic modelling) to provide an unbiased image of the crustal density distribution. Secondly, we applied a conventional least squares property inversion to a lithologically constrained model. The third approach applied a stochastic property modelling approach to the same lithologically constrained model. Finally, possible alternative model geometries were investigated through the use of combined property and geometry inversions.

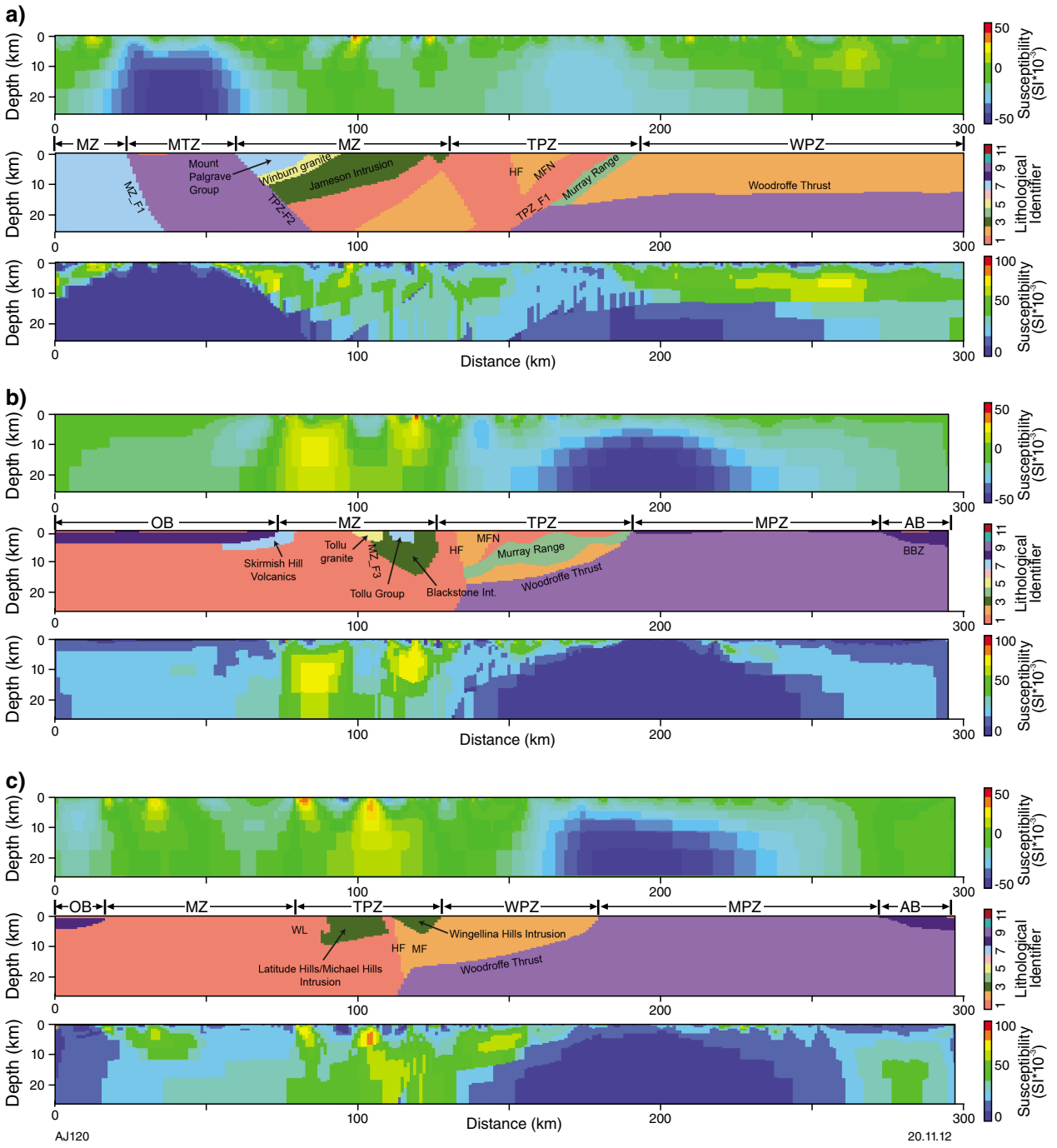

Figure 34. Magnetic modelling results for three profiles, showing: a) model results along an E–W profile at Y = 7142000 mN (line A–A', Fig. 32); b) model results along a S–N profile at X= 431000 mE (line B–B', Fig. 32); c) model results along a S–N profile at X = 491000 mE (line C–C', Fig. 32). Each panel is 25 km from top to bottom and crosses the entire model. There is no vertical exaggeration. For each: (i) the top panel shows the results of the unconstrained magnetic inversion; (ii) the centre panel shows the geological model (see Table 8 for lithological indentifiers); (iii) the bottom panel shows the lithologically constrained inversion result. The two inversion models have different susceptibility colour stretches; however, these are both linear and have the same range, so can be directly compared.

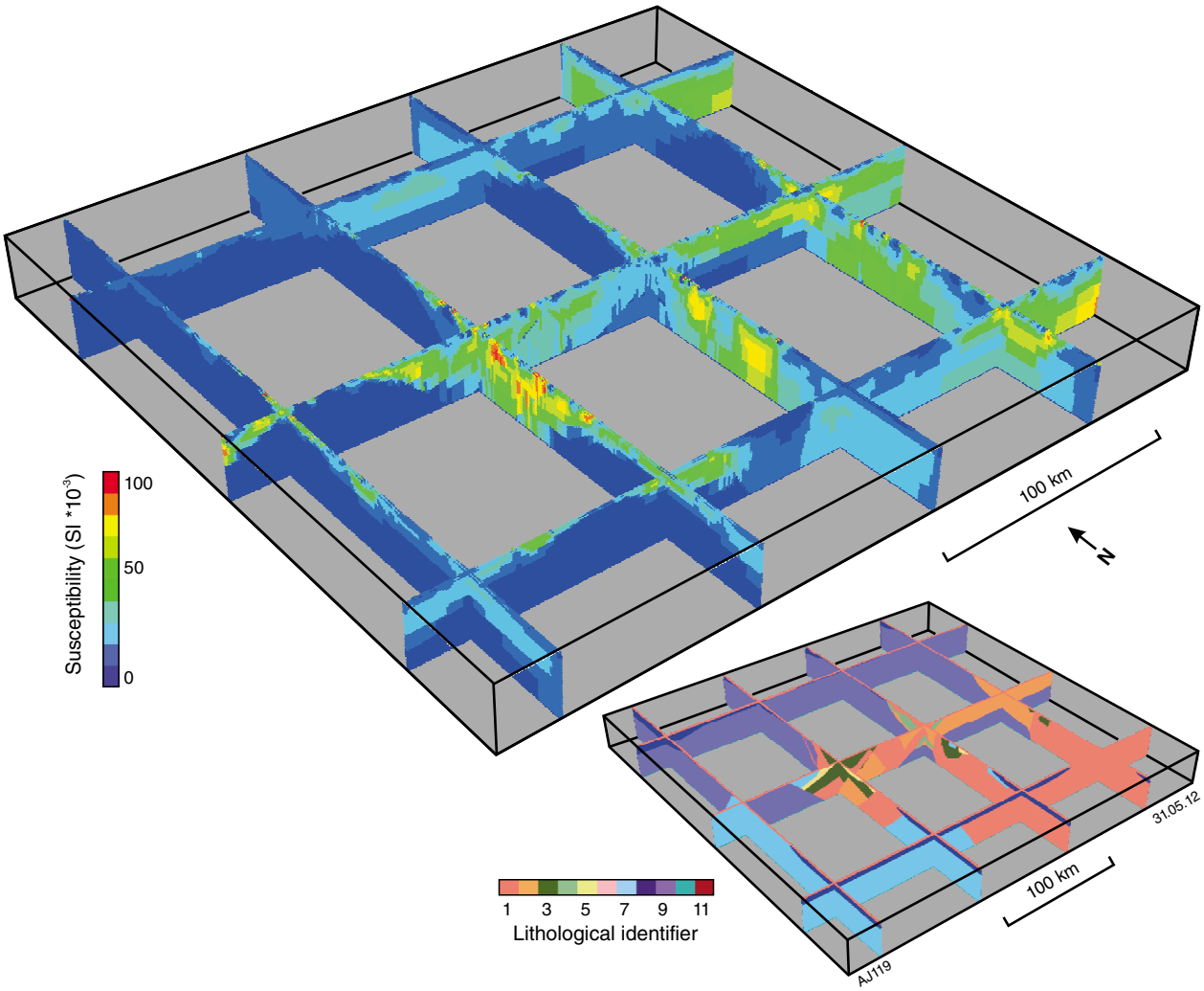

Figure 35. 3D view of the lithologically constrained magnetic inversion result showing the susceptibility distribution (top left) and the geological model (bottom right). The box measures 26 km from top to bottom, 300 km from east to west, and 290 km from north to south. A 3D PDF of this model is included to aid visualization (see supplementary material on CD).

Data processing for gravity inversion

As for the magnetic models, it was important that the gravity data were processed appropriately for inversion. In this case, the kriged free-air anomaly grid (Fig. 2b) was upward continued by 500 m. Compared to the magnetic data, the distribution of gravity data is highly irregular, ranging from dense measurements along several profiles (500 m spacing or less), to a regional grid (2.5 km spacing) throughout the central west Musgrave Province, and much coarser-spaced data (>5 km spacing) elsewhere (Fig. 36). Because of this, a regular grid of measurements was not used, but the upward continued data grid was re-sampled at every data point, and these data points were used in inversion (Fig. 36). For the gravity calculations, measurement height was adjusted to 500 m above the topographic surface.

Initial models and inversion set-up

Gravity inversions were undertaken using the entire crust, including the crust–mantle boundary. The base of the model is at 75 km, and includes a lower crustal layer with a density of 2900 kg/m^3 and a mantle layer with a density of 3300 kg/m^3. Cell size and lateral model extents are the same as for the magnetic model, but the depth discretization is different, with a base cell size of 500 m, and a more gradual multiplicative factor of 1.1 (i.e. 500, 550, 605 m, and so on). The lower crust and mantle layers were excluded from property inversion, so these layers were not vertically discretized.

With the exception of the unconstrained model, which is confined to the upper crust (25 km), all models used the whole-crust 3D model. Initial densities for each

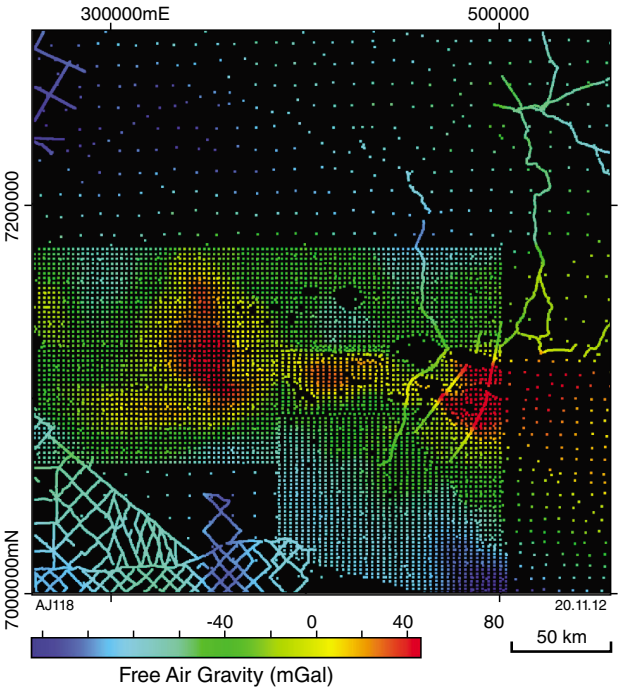

Figure 36. Gravity data for inversion. Gridded free-air gravity data were upward continued by 500 m, and this grid was re-sampled at the original data points.

lithological package are equal to the mean density of the unimodal model that best fits the petrophysical data (Table 8). The permitted density range for conventional property inversion was defined as the mean ± 2σ for each unit. However, this was increased to ± 3σ for the stochastic inversion (Table 8), to provide the correct property distribution. Property-only gravity inversions were run using the following restrictions: the maximum density change per iteration was 20 kg/m^3, and the maximum number of iterations was 40. This results in a maximum possible density change of 800 kg/m^3. Target misfit was 0.5 mGal, which is approximately 2% of the initial misfit (28.1 mGal).

Combined property–geometry inversions were used to investigate potential alternative geometries for the model. A particular focus was to assess potential changes to the geometry of the lower-crustal layers, and the depth to the base of Giles Suite intrusions. These inversions used a series of forty alternating density and geometry inversions of one iteration each. As a result of this method, the per-iteration constraints became very important in controlling the degree to which the misfit is reduced by changes to model geometry, or alternatively intra-unit density. The configuration required to best replicate nature is unknown, so it is important to test several configurations. In this work, five different configurations were applied, from which the lithological mode (the most commonly observed lithology) and the mode order (the number of times this lithology was observed) were derived. These provided an indication of the most likely lithology given the initial conditions of the model, and an indication of the variability of this result under different inversion conditions.

Results

Unconstrained density model

For this inversion, initial density was 2770 kg/m^3, the minimum bound was 2400 kg/m^3 and the maximum bound was 3400 kg/m^3. After 40 iterations, this inversion achieved an acceptable misfit to the data (1.29 mGal), although it did not converge to the target misfit of 0.5 mGal. The remaining misfit is characterized by generally short-wavelength patterns. The highest misfits are observed in the east of the model, within the southeast Tjuni Purlka Zone, around the Jameson intrusion and Cavenagh Fault, and in the Mulga Park Zone (Fig. 37a).

Although this model provides a reasonable indication of the relative mass excess (or deficit) within the crust, it fails to resolve the geometry of key features (Fig. 38), and is generally characterized by over-smoothed, subvertical features. This model is not considered further here, although it is available in 3D PDF format for visualization (supplementary material on CD).

Lithologically constrained density models

After 40 iterations, the conventional property model achieved a misfit of 1.28 mGal, suggesting that the initial model is petrophysically acceptable. The remaining misfit is generally low, and fairly evenly distributed (Fig. 37b), although a few 'hotspots' exist over the Michael Hills and Wingellina Hills intrusions. These may be topography related. The northernmost Mulga Park Zone exhibits positive misfit, suggesting insufficient density, although this area is at the edge of the model, and this may in part be an edge effect.

Despite lower efficiency due to the random nature of property changes, the stochastic property model showed similar performance, achieving a misfit of 2.11 mGal after 40 iterations. More iterations would likely reduce this further. The remaining misfit in this model is generally low, but contains two prominent hotspots, and several smaller areas of poor fit to the data (Fig. 37c). The positive hotspot lies over a gravity high within the Bentley Supergroup, likely caused by abundant basaltic layers within the Cassidy Group. The negative hotspot lies within the Walpa Pulka Zone, between the Fanny Fault and WPZ_F1. Gravity in this region is slightly lower than the rest of the Walpa Pulka Zone, although not especially so, perhaps indicating a greater abundance of Wirku Metamorphics. These residual anomalies are interpreted to represent areas where the imposed petrophysical limits have reduced the capability of the inversion to reduce misfit. In the petrophysical data, both the Bentley Supergroup and the Pitjantjatjara Supersuite have bimodal density distributions (Fig. 21), and the use of a unimodal distribution for modelling may be inappropriate.

A smaller area of poor fit over the Jameson intrusion highlights another case where the imposed statistical distribution has limited the ability of the algorithm to fit the data. In this case, the region of poor fit coincides with a small region of Warakurna granite contained within the Jameson intrusion, but not included in the model. This granitic material is imaged on profile 1 (Fig. 38a) as a

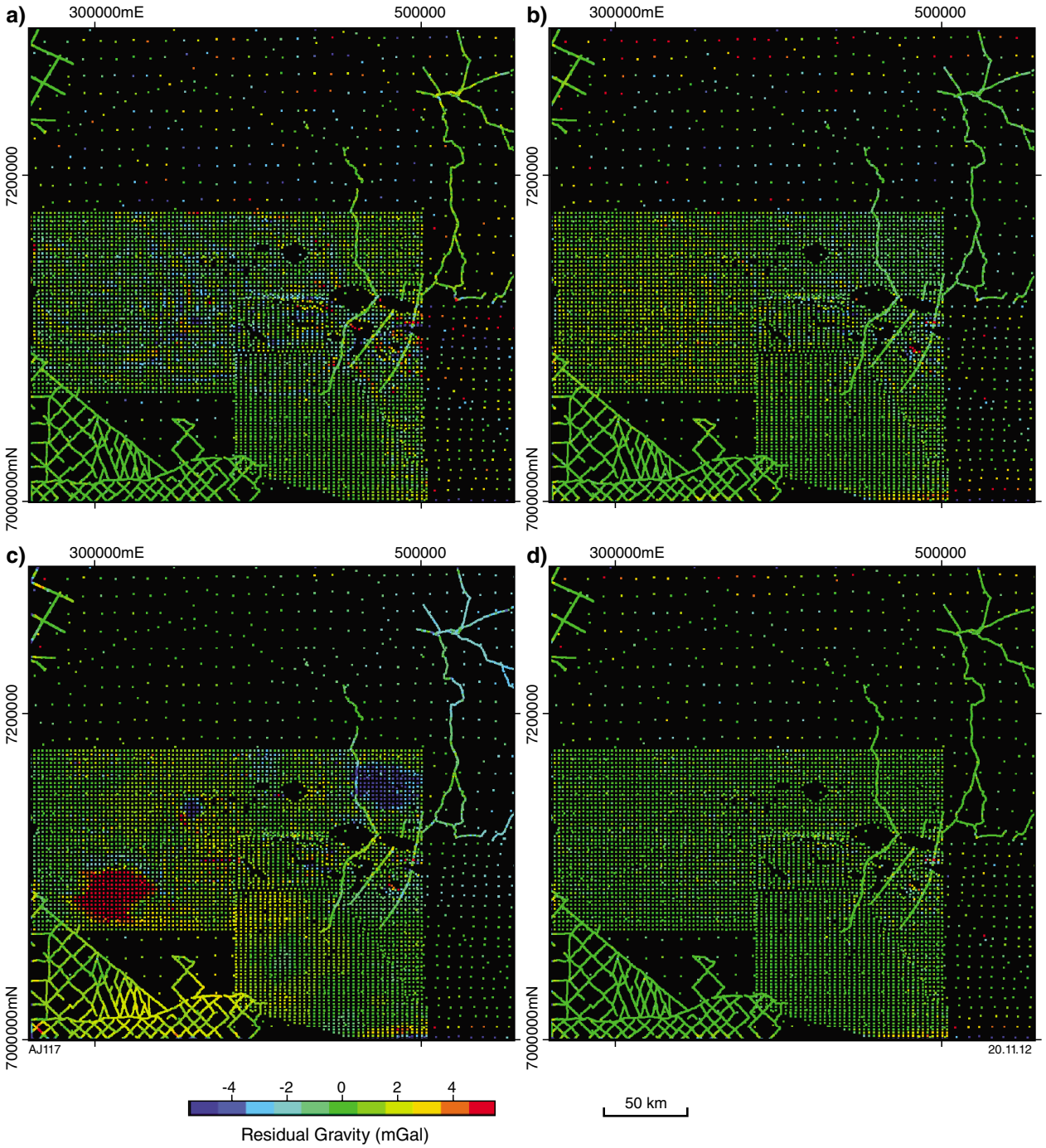

Figure 37. Gravity modelling misfits for: a) the unconstrained gravity inversion; b) the conventional property inversion model; c) the stochastic property inversion model; d) the final geometry–property inversion model

sub-circular density low within the Jameson intrusion (approximately 100 km along profile), although its structure is probably tabular, and southwest dipping, similar to the Winburn granite (see Fig. 23). Other small regions of poor fit correspond to the margins of Giles Suite intrusions. These may reflect the difficulty of matching steep gradients in the data, or errors in mapping the boundaries of these intrusions accurately.

The conventional and stochastic models show the different nature of the property distributions derived by each inversion process. However, if the stochastic result is smoothed (Fig. 38), the results are shown to be quite similar, although the stochastic inversion shows a greater range of density values. In part, this may reflect the broader property limits, but also reflects the more chaotic property distribution, which puts high and low values proximal to each other.

The key profiles (Fig. 38) show that significant intra-unit density variations are observed. Despite these intra-unit variations, the fundamental boundaries in the model (e.g. the margins of Giles Suite intrusions, the base of Centralian Superbasin, the Woodroffe Thrust, and the Mann Fault) remain quite distinct, suggesting that the initial model was largely acceptable. Of course, the acceptability of these models does not mean that other models are unacceptable, and it is useful to explore some alternative geometries.

Combined density–geometry models

Combined property–density inversions were run with the following restrictions: the maximum density change per iteration was constant at 20 kg/m^3. In five different inversions, the maximum permitted change to boundaries was set at 0.25, 0.5, 1, 2 and 5% of their depth. All other inversion parameters were unchanged from the density-only modelling.

Each inversion was run with alternating iterations until the inversion stalled; i.e. the iteration failed to reduce the misfit. In each case, geometrical inversion proved to be less effective at reducing the misfit than density inversion. However, the per-iteration constraints proved highly influential in controlling the final geometry.

With a permitted change of 5%, geometry inversion proved ineffective beyond the fifth iteration, whereas with a permitted change of 0.25%, geometry inversion proved effective until iteration 55. Geometry changes with 2%, 1%, and 0.5% permitted change proved effective to iterations 13, 19, and 37, respectively. The effect of this parameter on the model result is that, where larger geometry changes are permitted, more of the misfit is resolved through geometry changes, resulting in greater change to the model geometry overall.

Using a voxet, with X and Y discretization as before, but Z discretized into regular 500-m-thick cells, the lithological mode was calculated for each model cell from the five model results. This indicates the most likely lithological result given the initial conditions of the inversion (Fig. 39). Simultaneously, the order of this mode was derived to indicate variability (centre panel of each profile in Fig. 39). An order of five indicated that all models generated the same lithology for that cell, whereas lower values indicated that the cell had been occupied by other lithologies in at least one model. Most contacts involve just two lithologies, but some involve three, in which case a mode order of two is possible, although these are quite rare.

This result shows that, when the geometry is permitted to change by up to 5% per iteration, these changes are relatively minor. Permitted per-iteration changes of greater than 5% result in unrealistic geometries in the lower crust. Geometry changes are concentrated at the boundaries with greatest density contrast. Hence the crust–mantle boundary and the upper crust – lower crust boundary demonstrate the greatest variability, although the boundaries of Giles Suite intrusions and the Woodroffe Thrust also show significant variability.

It is important to note that variability is not the same as an error estimate, but rather a test of how robust the inversion result is with different parameters. Importantly, low variability does not necessarily indicate that the boundary location is high in confidence, but may mean that the gravity inversion is insensitive to changes to this boundary, perhaps due to low density contrast. In addition, the depth of the grid cells used in the calculation of these (500 m) will not detect small geometrical changes. This is especially important for the boundary between basement rocks and the Centralian Superbasin, as relatively small changes here will affect the fit to the gravity field considerably.

To generate a final model of density structure that is consistent with the gravity field, the upper-crustal units of the modal lithology model were subjected to property inversion using a conventional approach (lower panel of each profile in Fig. 39). This model converged after 69 iterations, with a final misfit of 0.82 mGal. Misfit in this model is uniformly low (Fig. 37d). The intra-unit density structures generated by this model are similar to those of the models without any geometrical changes (compare Fig. 38 with Fig. 39).

Tectonic implications for the crustal structure of the west Musgrave Province

The magnetotelluric modelling, 2D potential field forward modelling, and 3D magnetic and gravity inversions indicate that crustal structure dominantly reflects the tectonics of the Giles Event and the Petermann Orogeny. The geometries of earlier events (Mount West Orogeny, Musgrave Orogeny) are recognized in places; however, at the crustal scale, these have been comprehensively overprinted, and are not discussed here. The structure of the Alice Springs Orogeny is also important in places — most notably at the southern margin of the province, and in the vicinity of the Lasseter–Mundrabilla Shear Zone. These were discussed in the preceding text, and are not discussed further here.

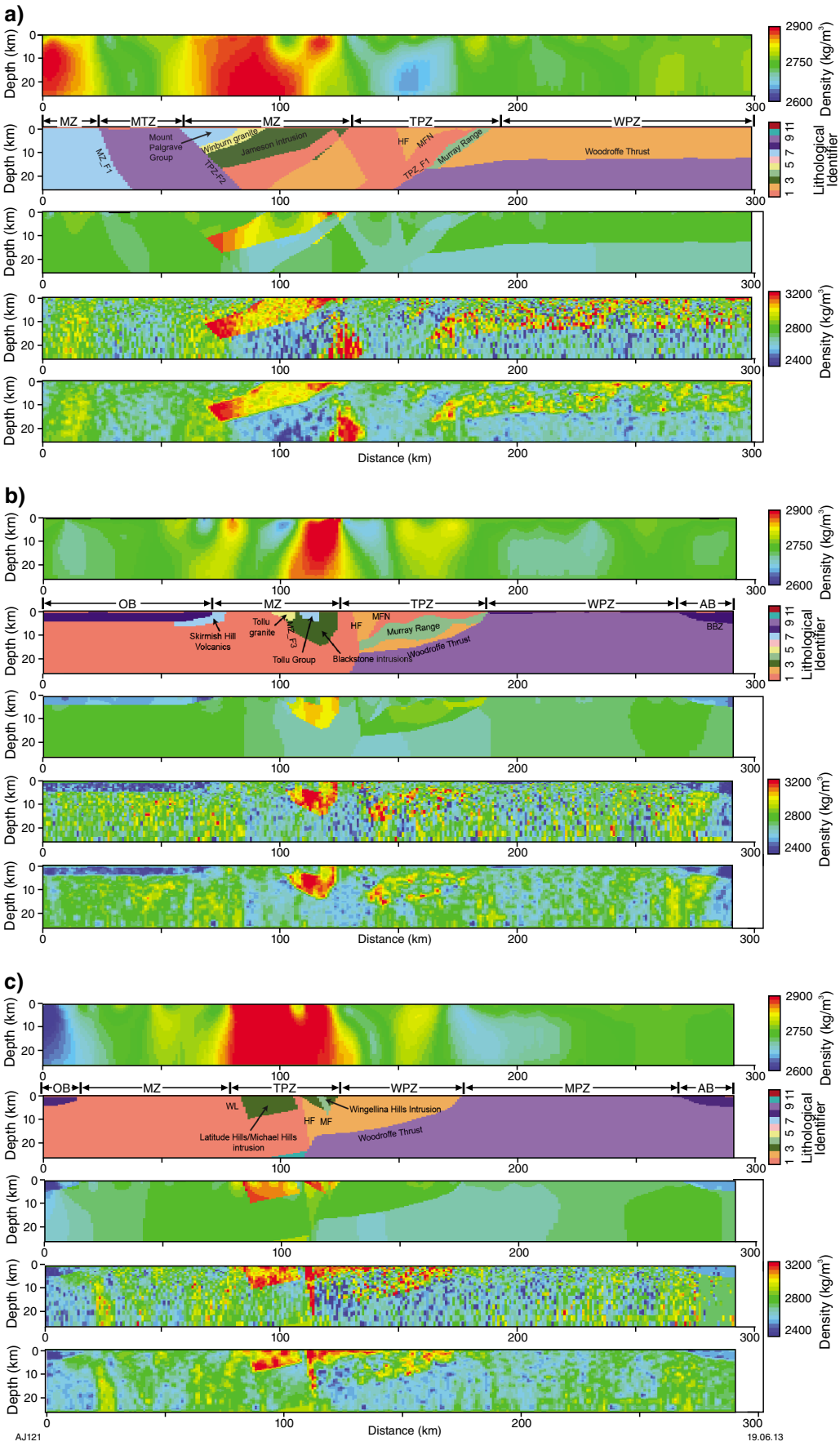
a)
b)
c)
Depth (km)
Distance (km)
Density (kg/m³)
Lithological Identifier
MZ
MTZ
TPZ
WPZ
OB
AB
MPZ
Mount Palgrave Group
Winburn granite
Jameson intrusion
MZ_F1
TPZ_F2
TPZ_F1
HF
MFN
Murray Range
Woodroffe Thrust
Skirmish Hill Volcanics
Tollu granite
TPZ_F3
Tollu Group
Blackstone intrusions
BBZ
WL
Wingellina Hills Intrusion
MF
Latitude Hills/Michael Hills intrusion
AJ121
19.06.13

Figure 38. (facing) Gravity modelling results for three key profiles: a) model results along an E–W profile at Y = 7142000 mN (line A–A', Fig. 32); b) model results along a S–N profile at X = 431000 mE (line B–B', Fig. 32); c) model results along a S–N profile at X = 491000 mE (line C–C', Fig. 32). Each panel is 25 km from top to bottom, and crosses the entire model. There is no vertical exaggeration. For each: (i) the top panel shows the results of the unconstrained inversion; (ii) the next panel shows the geological model (see Table 8 for lithological indentifiers); (iii) the panels beneath show the density distributions from conventional, stochastic, and smoothed stochastic inversions in that order. The unconstrained inversion model has a different colour stretch. See Figure 2 caption for fault abbreviations

The Giles Event

The Giles Event has contributed to the crustal structure of the west Musgrave Province in two main ways. Firstly, Giles Event magmatism resulted in a major addition of material to the crust, and secondly, syn- to post-magmatic deformation generated (or reactivated) many of the major faults. This is especially true of the Mamutjarra Zone, where original structure is well preserved (Evins et al., 2010; Joly et al., 2013). The steepness and orientation of Petermann-aged structures within the Tjuni Purlka Zone may suggest reactivation of earlier Giles Event rift architecture.

Geometry of the Giles Suite intrusions

The Giles Suite represents an enormous injection of mantle material into the crust, with a total preserved volume of >42 000 km^3. Most of this material belongs to the early-stage layered (G1) intrusions (36 000 km^3), but a significant component is made up of later stage massive gabbros (G2), especially in the Hinckley and Murray Range (7000 km^3).

The distribution and structure of G1 intrusions indicates several key controls on their emplacement. Firstly, the intrusions are, by and large, parallel with layering in the Kunmarnara Group suggesting that they were emplaced as lopoliths within the lower Bentley Supergroup. Gravity and magnetic modelling indicates that the major G1 intrusions of the Mamutjarra Zone (the Jameson intrusion, the Cavenagh intrusion, and the Blackstone intrusion, as well as the Bell Rock intrusion) are connected at depth (Fig. 41), and may have been emplaced as one enormous intrusion, with a total preserved volume of approximately 32 000 km^3. The exact nature of the relationships between these intrusions is disrupted by post-emplacement faulting and folding. However, the following relationships can be defined.

The Cavenagh and Blackstone intrusions are folded beneath the Tollu Group and are connected at depth. The Cavenagh intrusion lies beneath the Blackstone intrusion, although it is restricted in extent, lying east of the Cavenagh Fault but not reaching profile 6. The Blackstone and Bell Rock intrusions are separated by the Wintiginna Lineament, but they show clear mineralogical and structural similarities, indicating that they were once continuous. This relationship permits an estimate of motion on the Wintiginna Lineament. The vector connecting the fold axis at the base of the Blackstone intrusion with the deepest point at the base of the Bell Rock intrusion, interpreted as the same fold axis, indicates approximately 12.5 km of dextral strike-slip motion, and approximately 2 km of north-side-up reverse motion (Fig. 41). The Blackstone intrusion is also connected to the Jameson intrusion through a zone of deformation involving the Cavenagh Fault, and several other faults. A near continuous layer of relatively low-density troctolite can be traced through this zone, connecting the two intrusions (Fig. 41).

Although they each show later activity, the steeply north-dipping MZ_F1 and MZ_F3 faults, which are interpreted to be originally continuous, delimit the southern margins of the Jameson and Blackstone intrusions respectively. The Cavenagh intrusion is present on both sides of this structure, although it is significantly displaced across it (Figs 40a and 27). These relationships are interpreted to suggest that, after the emplacement of the relatively thin and spatially restricted Cavenagh intrusion, this structure became active during the emplacement of the Blackstone intrusion, accommodating the addition of more material to the crust. The Jameson intrusion is also bounded to the west by a normal fault, TPZ_F2, which likely accommodated the addition of material in a similar fashion. The location of the northern boundary of this mega-intrusion is not known; however, given the current geometries of the Jameson and Blackstone intrusions, it is extremely likely that the intrusion originally continued above the currently exposed level for some distance.

As a result of the Petermann Orogeny, the Tjuni Purlka Zone can be separated into northwest and southeast sections. Within the northwest Tjuni Purlka Zone, G1 rocks are relatively rare and disconnected in outcrop. However, forward modelling of gravity and magnetic data across this zone (Fig. 28) indicates that Giles Suite rocks are relatively extensive, but the intrusions are relatively thin (<5 km) and are dissected by later structures. These likely represent the lower levels of a relatively large intrusion. Connectivity between this intrusion and the intrusions of the Mamutjarra Zone is a possibility, but the models do not provide a particularly compelling geometry for such a link.

The Murray Range, dominated by G2 rocks, dips to the west at a moderate to shallow angle. The Hinckley gabbro dips to the north at ~50º. These gabbroic intrusions share many similarities, and were likely emplaced together, although they are now offset sinistrally by ~30 km across the Mann Fault (Evins et al., 2010). Although denser than most basement rocks, these gabbroic intrusions are not especially dense (2900 kg/m^3).

Gravity and magnetic forward modelling (Fig. 29) suggests that G1 intrusions within the southeast Tjuni Purlka Zone have been folded. The Michael Hills – Latitude Hills intrusion has also been tilted, such that

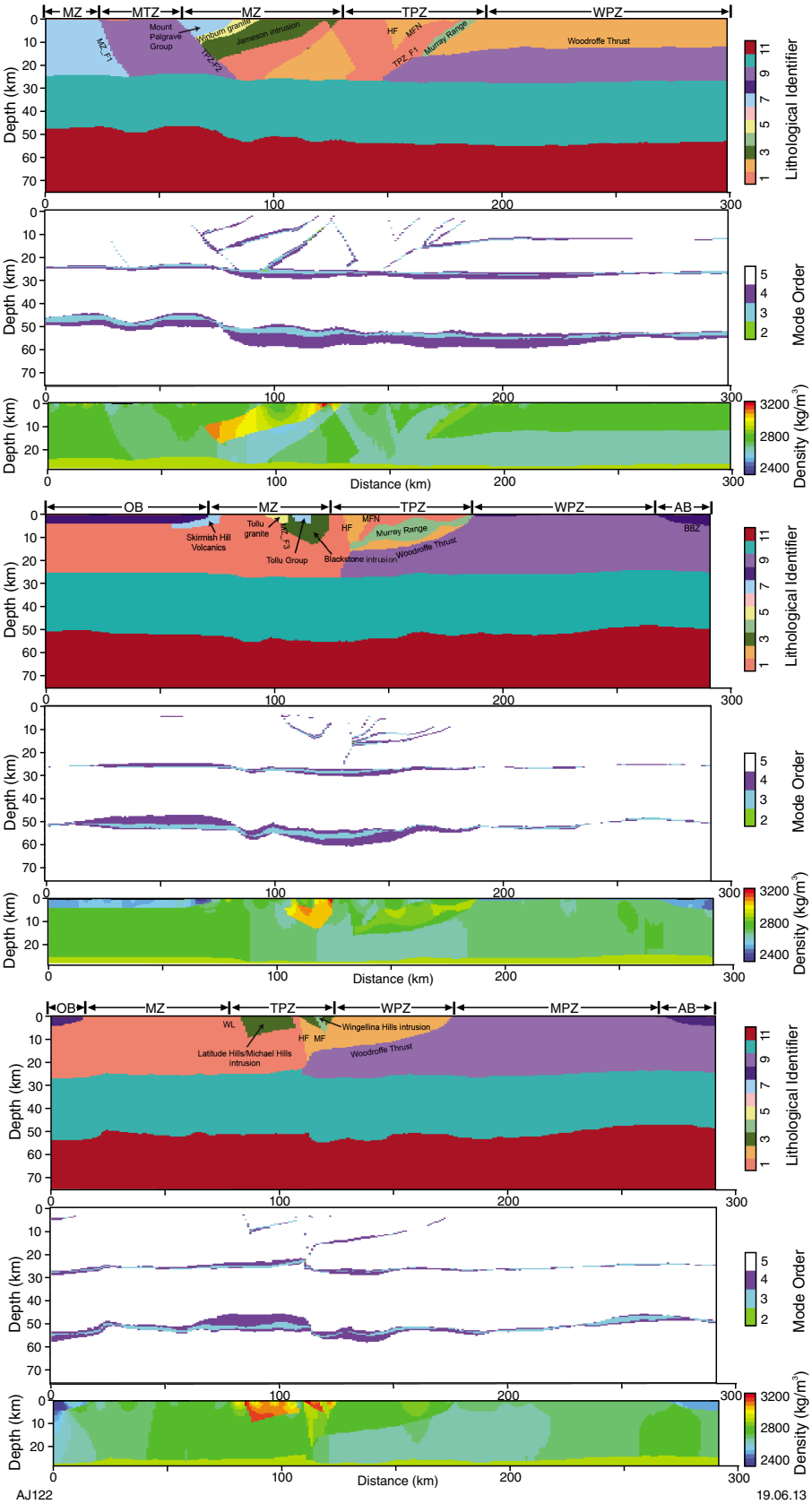
MZ
MTZ
MZ
TPZ
WPZ
Mount Palgrave Group
Winburn granite
Jameson Intrusion
MZ_F1
TPZ_F2
HF
MFN
TPZ_F1
Murray Range
Woodroffe Thrust
Depth (km)
Lithological Identifier
Mode Order
Density (kg/m3)
Distance (km)
OB
MZ
TPZ
WPZ
AB
Skirmish Hill Volcanics
Tollu granite
Tollu Group
Blackstone intrusion
BBZ
MZ
TPZ
WPZ
MPZ
AB
WL
Wingellina Hills intrusion
Latitude Hills/Michael Hills intrusion
HF
MF
Woodroffe Thrust
AJ122
19.06.13

Figure 39. (facing) Gravity modelling results from the combined property–density modelling, showing: a) model results along an E–W profile at Y = 7142000 mN (line A–A', Fig. 32); b) model results along a S–N profile at X = 431000 mE (line B–B', Fig. 32); c) model results along a S–N profile at X = 491000 mE (line C–C', Fig. 32). For each: (i) the top panel shows the lithological mode — the most commonly observed lithology for that cell (see Table 8 for lithological indentifiers); (ii) the middle panel shows the mode order — the number of times that cell is occupied by the mode value. This is a measure of model variability under differing inversion conditions; (iii) the bottom panel shows the upper-crustal density distributions required to satisfy the gravity misfit using the lithological model in the top panel. The top two panels are 75 km from top to bottom, and cross the entire model. Due to geometric changes, the depth of the bottom panel is variable, but it has the same vertical scale. There is no vertical exaggeration. See Figure 2 for fault abbreviations

the base of the intrusion slopes south at 12º. Maximum thickness (at the Mount West Fault) is ~10 km, and this reduces to ~6 km at the Hinckley Fault (Fig. 29). This forward model also indicates that these intrusions may originally have been continuous with the Hinckley intrusion (G1), and that this continuity has been disrupted by approximately 3 km of north-side-up reverse offset on the Hinckley Fault.

Architecture of the Bentley Supergroup and Warakurna Supersuite granites

The Bentley Supergroup dominates outcrop in the western third of the studied area. Along with geological mapping, this study shows that, although it is disrupted by faulting and folding in places, the overall stratigraphy of the Bentley Supergroup is largely well preserved and little deformed. Overall, this sequence dips shallowly to the southwest. Modelling suggests that the sequence comprises an approximately 15-km-thick sequence from the base of the Mount Palgrave Group to the top of the Mission Group. This thickness estimate does not include the Kunmarnara Group, the Tollu Group, the Scamp Formation, or the Pussy Cat Group, for which thicknesses are not defined. The total volume of the Bentley Supergroup in the 3D model is 360 000 km^3, although this is likely an overestimate due to their extended continuation beneath the Officer Basin, and the lack of a basement beneath the Pussy Cat Group. Nevertheless, the preserved volume of the Bentley Supergroup is likely to be of the order of 50 000 to 100 000 km^3.

Warakurna Supersuite granites exist throughout the area, although only two have been modelled in detail in this study — the Winburn granite and the Tollu granite. The Winburn granite is a large (~4500 km^3) stratiform intrusion that sits above the Jameson intrusion along almost its entire length (Fig. 30). Gravity and magnetic modelling indicates that this intrusion is approximately 5–6 km thick, and dips shallowly to the southwest. It is made up of two parts — a dense, magnetic lower part that is relatively thin (2 km), and a low-density, low-susceptibility upper part (Fig. 23). The emplacement of this intrusion was likely focused along the contact between the Jameson intrusion and the overlying strata. The relative ages of these intrusions are not well constrained by current radiometric dating.

The Tollu granite has an important role in constraining the tectonic evolution of the Mamutjarra Zone during the Giles Event. This intrusion lies symmetrically across the MZ_F3 fault zone, suggesting that this fault may have focused its emplacement. The intrusion is characterized by low density and low susceptibility. Its geometry is a shallowly north-dipping disc that reaches a maximum thickness of ~5 km. This geometry is parallel to layering in the Tollu Group and Blackstone intrusion (Fig. 28), suggesting that the intrusion was emplaced along a stratigraphic horizon. It is currently unclear whether emplacement preceded or postdated folding of these rocks. However, the disruption of fold-axial planes is interpreted to suggest synfolding emplacement (Joly et al., 2013).

Fault and fold architecture of the Giles Event

Several structures are preserved that are interpreted to be Giles Event-age, and from these, the fault and fold architecture of the Giles Event can be interpreted (Fig. 40a). The earliest Giles Event structures preserved are those that display apparent control on the emplacement of the Giles Suite (G1) intrusions: namely MZ_F3, MZ_F1, and TPZ_F2. MZ_F1 and MZ_F3, which dip steeply to the north-northwest, and TPZ_F2, which dips steeply to the east-southeast. These faults are interpreted as normal faults that have accommodated the intrusion of the voluminous Giles Suite (G1) intrusions. Although later reactivation episodes cannot be discounted, the fault-bounded geometry of the Murray Range is interpreted to be preserved from early Giles Event deformation (Joly et al., 2013). Forward modelling of gravity and magnetic data indicates that the faults that bound the Murray Range dip to the west at moderate angles (Figs 23 and 27).

Following exhumation and erosion of the Giles Suite intrusions and deposition of the Tollu Group (Evins et al., 2010), the next phase of deformation was characterized by east–west to northeast–southeast oriented folding. This folding is clearly imaged in the geometry of the Blackstone, Cavenagh, Michael Hills, and Latitude Hills intrusions, as well as the Tollu Group (Figs 27, 28, and 29). This event represents approximately north–south shortening within the southeast Tjuni Purlka Zone and the Mamutjarra Zone, although it is only observed to the east of the Cavenagh Fault.

The current crustal structure of the Mamutjarra Zone was largely established during the late stages of the Giles Event. Late Giles deformation is characterized by three fault sets: north–east trending normal faults, east-southeast trending dextral transtensional faults, and north–south trending sinistral transtensional faults (Joly et al., 2013). In the models, these faults are shown to

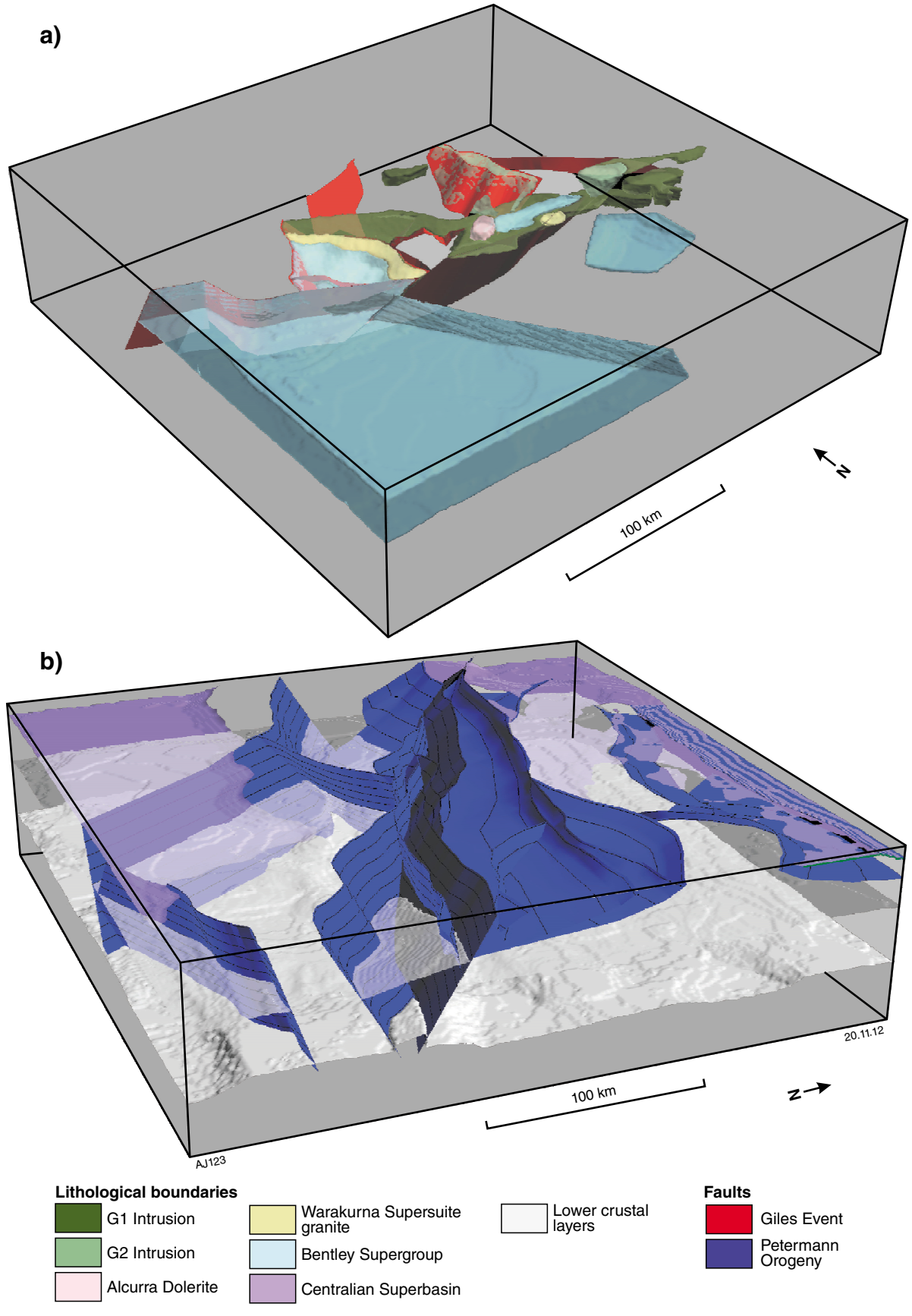

Figure 40. 3D perspective view of the final model showing: a) the architecture of the Giles Event viewed fron the southwest; b) the architecture of the Petermann Orogeny viewed from the east. In each, the box measures 76 km from top to bottom, 300 km from east to west, and 290 km from north to south. A 3D PDF of this model is included to aid visualization (see supplementary material on CD).

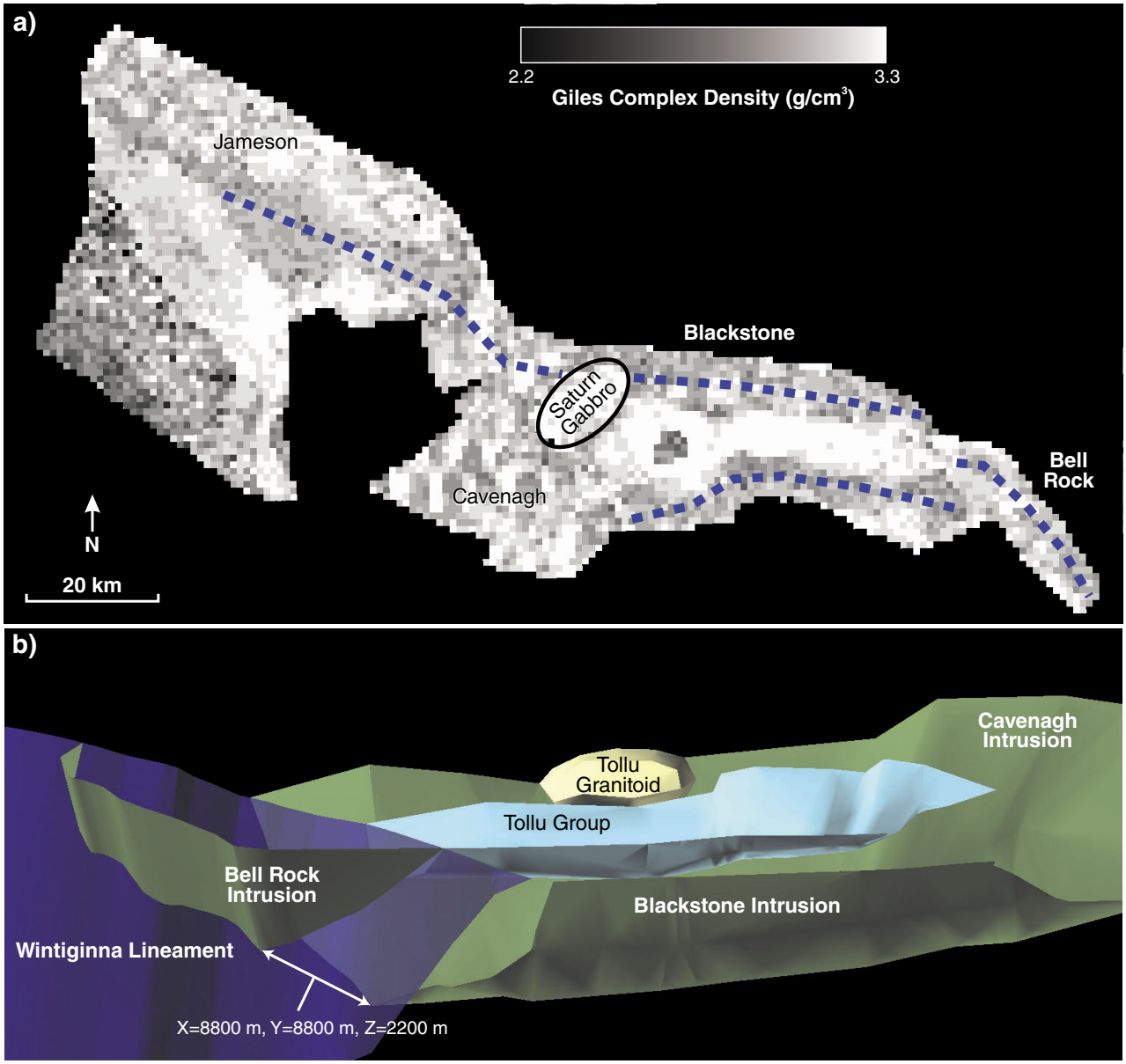

Figure 41. 3D models showing: a) geometry of the Giles Suite mega-intrusion, viewed from the top, incorporating the Jameson, Cavenagh, Blackstone, and Bell Rock intrusions. Note the continuous, low-density layer throughout these intrusions (dashed blue line). This is cut by the Saturn gabbro; b) perspective view of the Blackstone syncline area also showing the dislocation of the Bell Rock intrusion from the Blackstone intrusion. The view is from the north-northeast, slightly elevated. Post-Giles Suite offset on the Wintiginna Lineament is well constrained by the dislocation of the fold axis.

truncate and dissect the Upper Bentley Supergroup and disrupt the stratigraphy of the Giles Suite (Figs 23 to 28). Due to later deformation, late Giles Event structures are harder to define within the Tjuni Purlka and Walpa Pulka Zones. In the Tjuni Purlka Zone, most major faults are steeply dipping and, although interpreted to be of Petermann Orogeny age, may represent Giles Event-age rift architecture. In the Walpa Pulka Zone, the Fanny Fault is interpreted to be late Giles age (Joly et al., 2013). This fault and WPZ_F1 dip steeply to the northeast, and may indicate the architecture of the Giles Event in the Walpa Pulka Zone.

The Petermann Orogeny

This study provides a snapshot of the crustal structure of the Petermann Orogeny in Western Australia, including the geometry of major fault zones and the resulting topography of the upper crust – lower crust and crust–mantle boundaries.

Shear zone architecture of the Petermann Orogeny

Each of the zones of the west Musgrave Province displays different architecture for Petermann Orogeny shear zones. Although the Mamutjarra Zone was relatively unaffected by the Petermann Orogeny (Joly et al., 2013), several major faults were reactivated, including the Cavenagh Fault and MZ_F2 (Figs 31 and 40b). These faults appear to have undergone dominantly strike-slip movement during the Petermann Orogeny. Assuming MZ_F1 and MZ_F3 were originally continuous, approximately 20 km of apparent sinistral offset is recorded on the Cavenagh Fault since the emplacement of these intrusions (Fig. 2a). MZ_F2 cuts the Cavenagh Fault, and at its eastern end, is associated with approximately 12.5 km of apparent dextral offset of the Cassidy Group, causing a distinct step in the gravity anomaly near the province margin (Fig. 2b). The kinematics of the western part of this shear zone are uncertain, but north-side-up reverse movement on a steep fault plane is likely (Fig. 24).

The crustal structure of the Tjuni Purlka Zone is largely defined by Petermann Orogeny shear zones (Fig. 40b), although it is likely these have an earlier history, perhaps extending as far back as the Mount West Orogeny (Smithies et al., 2011). The major fault zones are steeply dipping, and are of sufficient scale to penetrate the entire crust. Three major fault systems are identified: the Wintiginna Lineament, the Hinckley Fault, and the Mann Fault – Mann Fault North – TPZ_F1 fault system. The Wintiginna Lineament demarcates the boundary between the moderate-density crust of the Mamutjarra Zone and the high-density crust of the southeast Tjuni Purlka Zone. This fault dips moderately steeply to the northwest, and may have accommodated 14 km of dextral offset and 3 km of north-side-up reverse offset. This shear zone continues into South Australia, where gravity and magnetic modelling suggests upwards of 5 km offset on the crust–mantle boundary (Aitken et al., 2009b). This shear zone does not reach mantle depths in Western Australia due to its truncation by the Mann Fault (Fig. 29).

The Hinckley Fault extends almost linearly through the centre of the Tjuni Purlka Zone (Figs 2a and 30). This shear zone is a fundamental crustal boundary, juxtaposing crustal blocks of different geological and geophysical properties along its length. Magnetic and gravity modelling suggests that this fault dips steeply to the north. In the southeast Tjuni Purlka Zone (Fig. 29), this fault is associated with the juxtaposition of extremely dense rocks against dense rocks, and, based on the offset to the base of the Hinckley intrusion from the Michael Hills intrusion, may have accommodated 3 km of north-side-up reverse offset. This reverse offset is also supported farther west by the juxtaposition of basement rocks against the Jameson intrusion (Fig. 26).

The Mann Fault, Mann Fault North, and TPZ_F1 are interpreted to be one fault system, with strain on the Mann Fault stepping over to the Mann Fault North, and strain from the Mann Fault North stepping over onto TPZ_F1. These faults are steeply south dipping overall, although dip becomes shallower towards the west (cf. Figs 23 to 29). In the easternmost part of the west Musgrave Province, the offset of the Murray Range from the Hinckley gabbro may indicate approximately 30 km of sinistral motion (Evins et al., 2010), although this is not a unique correlation. Added to this is approximately 10 km of south-side-up reverse motion (Fig. 29). The Mann Fault North also generates 10 km of apparent sinistral offset on the Murray Range. TPZ-F1 does not show much evidence of strike-slip motion, indicating that movement on this shear zone was dominated by dip-slip motion. Prominent isoclinal folding of Kunmarnara Group rocks in the hanging wall of this shear zone (Evins et al., 2009) supports reverse motion. Modelling suggests that the northernmost Tjuni Pulka Zone, north of TPZ-F1, is a wedge of crust thrust over the Mulga Park Zone via the Woodroffe Thrust. The existence of Giles Suite intrusions within this region may indicate that it represents a shallower-crustal level than the block to the south of the TPZ_F1, which is dominated by Kunmarnara Group and basement rocks.

The Walpa Pulka Zone also occupies a position above the Woodroffe Thrust, with Mulga Park Zone crust below. Structures in the Walpa Pulka Zone are typically shallowly south dipping, representing the influence of thrusting and crustal flow zones above the Woodroffe Thrust. Also present are two major fault zones — the Fanny Fault and WPZ_F1 — that dip more steeply to the north. These may represent Giles Event-age normal faults, although they have been significantly disrupted by Petermann Orogeny activity.

The east–west trending Woodroffe Thrust extends fairly linearly within Western Australia (Figs 2 and 30). Modelling indicates that the dip of this shear zone is approximately 30–50º to the south, but has a listric geometry, and flattens to a shallow-dipping detachment within 10–20 km of the surface. The Woodroffe Thrust merges into the MF – MFN – TPZ_FI fault system at approximately 15–20 km depth (Figs 28 and 29). Along its length, the Woodroffe Thrust has spawned numerous splays in both its footwall and hanging wall, although these are most pronounced at the western end where the fault system terminates in a series of splays (Fig. 2).

In the Northern Territory, the structure of the Mulga Park Zone is characterized by shallowly dipping thrusts, and nappe-style folding of both basement rocks and overlying sedimentary and volcanic rocks (Edgoose et al., 2004; Flöttmann et al., 2005). This structural character extends into Western Australia. However, there are significant differences. The Piltardi Detachment Zone extends only 15 km into Western Australia, before it is terminated by a sinistral tear fault that accommodates the differential motion between this thrust and PDZ_W, which likely shows much less motion. The models suggest that the amount of shortening reduces over a short distance to the west, with only limited folding of the Tjauwata Group on profile 5 (Fig. 27), and no folding of the Tjauwata Group on profile 6 (Fig. 28). The Mitika Zone shows crustal structure that is similar to the Mulga Park Zone, although faults in the Mitika Zone are typically steeper dipping.

Geometry of the lower crust in the west Musgrave Province

Recent work in South Australia has indicated interesting structure in the lower crust, characterized by thickened crust at the margins of the province, but with an uplifted wedge of mantle in the central region (Aitken et al., 2009a,b; Korsch and Kositcin, 2010). The structure of the lower crust was investigated as part of the gravity inversion process, and the likely geometry of the upper-crust – lower-crust transition and the crust–mantle boundary can be derived from these results (Fig. 42). It is important to note that, in the absence of any constraints, gravity inversion can only generate thinner, higher density crust, or thicker, lower density crust from the initial model. Seismic data and seismically constrained gravity inversions indicate that much of western central Australia contains thick, dense crust, possibly related to a mafic underplate (Aitken, 2010; Kennett et al., 2011). The method used cannot account for this underplate, so the geometry imaged by this method is best considered as representing the top of this feature.

Although the uncertainties are relatively high, each of these surfaces shows links to the major tectonic boundaries at the surface (Fig. 42). The two surfaces show similar geometry, although the upper-crust – lower-crust boundary has approximately half the amplitude of the crust–mantle boundary. From here on, discussion is directed at the crust–mantle boundary. However the same arguments apply to the upper-crust – lower-crust boundary.

The Mulga Park Zone is characterized by southward sloping crustal boundaries, indicating the influence of crustal thickening during the Petermann Orogeny. The maximum depth of the crust–mantle boundary beneath this zone is approximately 54 km (Fig. 42). South of the Woodroffe Thrust, the crust is generally thinner, although the tectonic zones have a strong influence. The Walpa Pulka Zone is underlain by very thick crust (55 km) in the region west of WPZ_F1, and slightly thinner crust to the east, thickening towards the south (49–52 km).

The northeast and southeast Tjuni Purlka Zones each exhibit relatively thin crust (45–48 km). These may relate to uplift on the Mann Fault and TPZ_F1. Note that the prominent thinning in the southeast Tjuni Purlka Zone is preserved from the initial model, with little variation across models. This implies that it is consistent with the gravity field, although alternative geometries are possible. However, the central Tjuni Purlka Zone shows a deep crustal depression (>54 km). This change in lower crustal structure coincides with the location of the Mann Fault North, indicating that crustal thickening is observed within the zone of strain transfer from the Mann Fault to TPZ-F1.

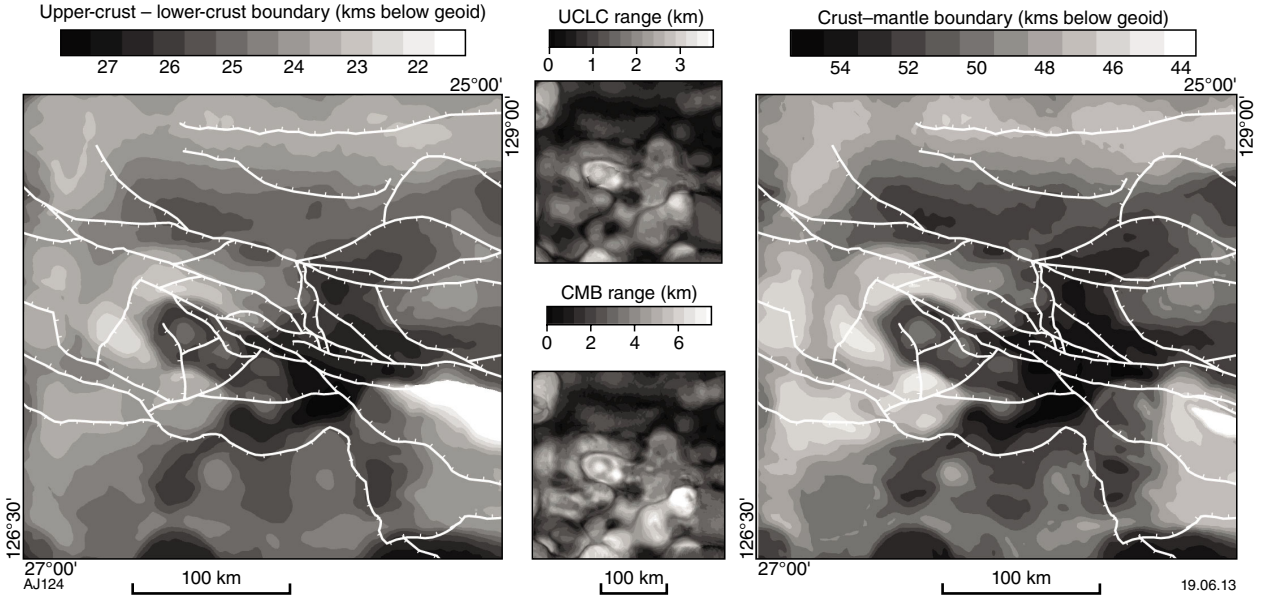

Figure 42. Geometries of the upper-crust/lower-crust boundary (left) and the crust–mantle boundary (right) resulting from inversion. Also shown is the range in geometry from the five property–geometry models (UCLC = upper crust – lower crust, CMB = crust–mantle boundary). These images show the clear link between the geometry of the lower-crustal and upper-crustal features.

In the Mamutjarra Zone, the crust is thick (>50 km) beneath the major Jameson–Blackstone–Cavenagh G1 intrusion, perhaps reflecting the influence of these intrusions on crustal thickness. The southeast Mamutjarra Zone is underlain by thick crust also; however, the western Mamutjarra Zone and the Mitika Zone are underlain by thinner crust (45–50 km).

Conclusions

Constrained inverse and forward modelling of potential field data, allied with magnetotelluric modelling has been used to image the crustal structure of the west Musgrave Province. These models show that, although earlier and later events are influential in places, crustal structure dominantly reflects the architecture derived during the Giles Event and the Petermann Orogeny.

The Giles Event is characterized by the addition of a large amount of material to the crust, in the form of mafic intrusions and supracrustal volcanic sequences. Layered mafic intrusions (G1) are up to 8 km thick. The major intrusion was emplaced along an ESE-trending axis bounded to the south and west by faults that appear to have accommodated the inflation of the crust. Subsequent massive gabbro intrusions (G2) were dominantly emplaced along a north-northwest trending, west-dipping axis (the Murray Range). Later stages of the Giles Event saw the eruption of the Bentley Supergroup volcanic rocks, predominantly in the western Mamutjarra Zone. These volcanic rocks attain a thickness of at least 15 km. The later stages of the Giles Event are characterized by deformation of these units, including folding and several generations of steeply dipping normal and transtensional faults. This sequence of events defines the current structure of the the Mamutjarra Zone, and it may well have influenced later deformation within the other zones.

The Petermann Orogeny is characterized by differing styles of deformation within each zone of the province. Deformation is limited in the Mamutjarra Zone, where Giles Event structure is largely preserved. In the Tjuni Purlka Zone, structure is characterized by major, crustal-scale, transpressional shear zones that have accommodated significant offsets, causing juxtaposition of crustal blocks of different character. The Walpa Pulka Zone is characterized by the thrusting of lower-crustal material over the Mulga Park Zone, with associated crustal thickening. The Mulga Park Zone is characterized by crustal thickening due to low-angle thrust faulting.

The full implications of the above work for mineral exploration are discussed in the companion report of Joly et al. (2013).

Acknowledgements

The Musgraves MT survey was funded by the Exploration Incentive Scheme of the Western Australian Government. We acknowledge the support of AuScope for the ANSIR MT equipment, and Goran Boren for his assistance in the use of it. We thank GSWA field staff Mario, Ray, and Paul for their assistance in collecting the MT data, Chris Hocking for collecting the petrophysical data, and Mario Werner and Heather Howard for their help understanding the geology of the west Musgrave Province.

References

Abeysinghe, PB 2003, Mineral occurrences and exploration potential of the Arunta–Musgrave area: Geological Survey of Western Australia, Record 2002/9, 33p.

Aitken, ARA 2010, Moho geometry gravity inversion experiment (MoGGIE): a refined model of the Australian Moho, and its tectonic and isostatic implications: Earth and Planetary Science Letters, v. 297, p. 71–83.

Aitken, ARA and Betts, PG 2008, High-resolution aeromagnetic data over central Australia assist Grenville-era (1300–1100 Ma) Rodinia reconstructions: Geophysical Research Letters, v. 35 (L01306), doi:10.1029/2007GL031563.

Aitken, ARA and Betts, PG 2009a, Constraints on the Proterozoic supercontinent cycle from the structural evolution of the south-central Musgrave Province, central Australia: Precambrian Research, v. 168, no. 3–4, p. 284–300.

Aitken, ARA and Betts, PG 2009b, Multi-scale integrated structural and aeromagnetic analysis to guide tectonic models: an example from the eastern Musgrave Province, central Australia: Tectonophysics, v. 476, no. 3–4, p. 418–435.

Aitken, ARA, Betts, PG and Ailleres, L 2009a, The architecture, kinematics, and lithospheric processes of a compressional intraplate orogen occuring under Gondwana assembly: the Petermann Orogeny, central Australia: Lithosphere, v. 1, no. 6, p. 343–357.

Aitken, ARA, Betts, PG, Weinberg, RF and Gray, D 2009b, Constrained potential field modelling of the crustal architecture of the Musgrave Province in central Australia: Evidence for lithospheric strengthening due to crust-mantle boundary uplift: Journal of Geophysical Research, v. 114, no. B12, doi:10.1029/2008JB006194.

Baker, PM and Waugh, RS 2005, The role of surface geochemistry in the discovery of Babel and Nebo magmatic nickel–copper–PGE deposits: Geochemistry: Exploration, Environment, Analysis, v. 5, p. 195–200.

Ballhaus, C and Berry, RF 1991, Crystallization pressure and cooling history of the Giles layered igneous complex, central Australia: Journal of Petrology, v. 32, no. 1, p. 1–28.

Begg, GC, Hronsky, JMA, Arndt, NT, Griffin, WL, O'Reilly, S and Hayward, N 2010, Lithospheric, cratonic, and geodynamic setting of Ni–Cu–PGE sulfide deposits: Economic Geology, v. 105, p. 1057–1070.

Braun, J, McQueen, H and Etheridge, M 1991, A fresh look at the Late Palaeozoic tectonic history of western-central Australia: Exploration Geophysics, v. 22, p. 49–54.

Caldwell, TG, Bibby, HM and Brown, C 2004, The magnetotelluric phase tensor: Geophysical Journal International, v. 158, p. 457–469.

Chave, AD and Smith, JT 1994, On electric and magnetic galvanic distortion tensor decompositions: Journal of Geophysical Research, v. 99 (B3), p. 4669–4682.

Chave, AD, Thomson, DJ and Ander, ME 1987, On the robust estimation of power spectra, coherences, and transfer functions: Journal of Geophysical Research, v. 92, no. B1, p. 633–648.

Clarke, GL, Sun, S-S and White, RW 1995, Grenville age belts and associated older terranes in Australia and Antarctica: AGSO Journal of Australian Geology and Geophysics, v. 16, p. 25–39.

Collins, CDN, Drummond, BJ and Nicoll, MG 2003, Crustal thickness patterns in the Australian continent: Geological Society of America Special Papers, v. 372, p. 121–128.

Dunlop, D and Ozdemir, O 1997, Rock magnetism: Cambridge University Press, Cambridge, UK, 526p.

Edgoose, CJ, Scrimgeour, IR and Close, DF 2004, Geology of the Musgrave Block, Northern Territory: Northern Territory Geological Survey, Report 15, 46p.

Evins, PM, Smithies, RH, Howard, HM, Kirkland, CL, Wingate, MTD and Bodorkos, S 2010, Devil in the detail; The 1150–1000 Ma magmatic and structural evolution of the Ngaanyatjarra Rift, west Musgrave Province, Central Australia: Precambrian Research, v. 183, p. 572–588.

Evins, PM, Smithies, RH, Maier, WD and Howard, HM 2009, Holt, WA Sheet 4546: Geological Survey of Western Australia, 1:100 000 Geological Series.

Flöttmann, T, Hand, M, Close, D, Edgoose, C and Scrimgeour, I 2005, Thrust tectonic styles of the intracratonic Alice Springs and Petermann Orogenies, Central Australia: AAPG Memoir, v. 82, p. 538–557.

FrOG Tech Pty Ltd (compiler) 2005, OZ SEEBASE Study, in Public Domain Report to Shell Development Australia: FrOG Tech Pty Ltd, Canberra, Australian Capital Territory, Australia, 135p.

Fullagar, PK 1985, Spike recovery deconvolution, in Developments in Geophysical Exploration Methods (6th edition) edited by AA Fitch: Elsevier Applied Science Publishers, London, UK, p. 1–25.

Fullagar, PK 2011, VPmg™ User Documentation V 6.1: Fullagar Geophysics, Brisbane, Queensland.

Fullagar, PK, Pears, GA and McMonnies, B 2008, Constrained inversion of geologic surfaces — pushing the boundaries: The Leading Edge, v. 27, no. 1, p. 98–105.

Gamble, TD, Goubau, WM and Clarke, J 1979, Magnetotellurics with a remote reference: Geophysics, v. 44, p. 53–68.

Glikson, AY, Ballhaus, CG, Clarke, GL, Sheraton, JW, Stewart, AJ and Sun, SS 1995, Geological framework and crustal evolution of the Giles mafic/ultramafic complex and environs, western Musgrave Block, central Australia: AGSO Journal of Australian Geology and Geophysics, v. 16, p. 41–67.

Glikson, AY, Stewart, AJ, Ballhaus, C, Clarke, B, Feeken, EHJ, Leven, JH, Sheraton, JW and Sun, SS 1996, Geology of the western Musgrave Block, Central Australia, with particular reference to the mafic–ultramafic Giles Complex: AGSO Bulletin, v. 239, p. 41–68.

Groom, RW and Bailey, RC 1989, Decomposition of magnetotelluric impedance tensor in the presence of local three-dimensional galvanic distortion: Journal of Geophysical Research, v. 94, p. 1913–1925.

Howard, HM, Smithies, RH, Evins, PM, Pirajno, F and Skwarnecki, MS 2009, Bell Rock, WA Sheet 4645 (2nd edition): Geological Survey of Western Australia, 1:100 000 Geological Series.

Howard, HM, Werner, M, Smithies, RH, Evins, PM, Kirkland, CL, Kelsey, DE, Hand, M, Collins, AS, Pirajno, F, Wingate, MTD, Maier, WD and Raimondo, T 2011, The geology of the west Musgrave Province and the Bentley Supergroup — a field guide: Geological Survey of Western Australia, Record 2011/4, 116p.

Joly, A, Dentith, MC, Porwal, A, Spaggiari, CV, Tyler, IM and McCuaig, TC 2013, An integrated geological and geophysical study of the west Arunta Orogen and its mineral prospectivity: Geological Survey of Western Australia, Report 113, 89p.

Jones, AG 1999, Imaging the continental upper mantle using electromagnetic methods: Lithos, v. 48, p. 57–80.

Jones, AG and Garcia, X 2004, Electrical resistivity structure in the Yellowknife River fault zone and surrounding region, *in* Gold in the Yellowknife Greenstone Belt, Northwest Territories: Results of the EXTECH III Multidisciplinary Project *edited by* CD Anglin et al: Geological Association of Canada Mineral Deposits Division, Special Publication, p. 126–141.

Jones, AG and Jödicke, H 1984, Magnetotelluric transfer function estimation improvement by a coherence based rejection technique (EM1.5), *in* Abstract Volume: 54th Society of Exploration Geophysics Annual General Meeting, Atlanta, Georgia, USA, SEG Extended Abstracts v. 3, p. 51–55.

Kennett, BLN, Salmon, M, Saygin, E and AusMoho Working Group 2011, AusMoho: the variation of Moho depth in Australia: Geophysical Journal International, v. 187, no. 2, p. 946–958, doi:10.1111/j.1365-246X.2011.05194.x.

Kirkland, CL, Wingate, MTD and Smithies, RH 2011, 194762: leucogabbro, Mount Finlayson; Geochronology Record 966: Geological Survey of Western Australia, 4p.

Korsch, RJ and Kositcin, N 2010, GOMA (Gawler Craton – Officer Basin – Musgrave Province – Amadeus Basin) Seismic and MT Workshop 2010: Geoscience Australia, Record 2010/39, 162p.

Lambeck, K and Burgess, G 1992, Deep crustal structure of the Musgrave Block, central Australia: results from teleseismic travel-time anomalies: Australian Journal of Earth Sciences, v. 39, p. 1–20.

Li, Y and Oldenburg, DW 2003, Fast inversion of large-scale magnetic data using wavelet transforms and a logarithmic barrier method: Geophysical Journal International, v. 152, no. 2, p. 251–265.

Lindsay, JF and Leven, JH 1996, Evolution of a Neoproterozoic to Palaeozoic intracratonic setting, Officer Basin, South Australia: Basin Research, v. 8, no. 4, p. 403–424.

Parker, RL 1994, Geophysical inverse theory: Princeton University Press, Princeton, New Jersey, USA, 386p.

Pellerin, L, Schmidt, JM and Hoversten, GM 2003, Two-dimensional inverse and three-dimensional forward modelling of MT data to evaluate the mineral potential of the Amphitheater Mountains, Alaska, USA in Proceedings of the 3rd International Symposium in Three-dimensional Electromagnetics (3DEM-3), 20–21 February 2003, Adelaide, South Australia.

Raimondo, T, Collins, AS, Hand, M, Walker-Hallam, A, Smithies, RH, Evins, PM and Howard, HM 2010, The anatomy of a deep intracontinental orogen: Tectonics, v. 29 (TC4024), doi:10.1029/2009TC002504.

Rodi, W and Mackie, RL 2001, Nonlinear conjugate gradients algorithm for 2-D magnetotelluric inversion: Geophysics, v. 66, p. 174–187.

Scrimgeour, IR and Close, DF 1999, Regional high pressure metamorphism during intracratonic deformation: the Petermann Orogeny, central Australia: Journal of Metamorphic Geology, v. 17, p. 557–572.

Seat, Z, Beresford, SW, Grguric, BA, Waugh, RS, Hronsky, JMA, Gee, MMA, Groves, DI and Mathison, CI 2007, Architecture and emplacement of the Nebo–Babel gabbro–norite-hosted magmatic Ni–Cu–PGE sulfide deposits, west Musgrave, Western Australia: Mineralium Deposita, v. 42, p. 551–582.

Selway, K, Hand, M, Heinson, GS and Payne, JL 2009, Magnetotelluric constraints on subduction polarity: Reversing reconstruction models for Proterozoic Australia: Geology, v. 37, no. 9, p. 799–802.

Selway, KM, Hand, M, Payne, JL, Heinson, GS and Reid, A 2011, Magnetotelluric constraints on the tectonic setting of Grenville-aged orogenesis in central Australia: Journal of the Geological Society, v. 168, no. 1, p. 251–264.

Simpson, F and Bahr, K 2005, Practical magnetotellurics: Cambridge University Press, Cambridge, England, 270p.

Smithies, RH, Howard, HM, Evins, PM, Kirkland, CL, Bodorkos, S and Wingate, MTD 2009a, West Musgrave Complex — new geological insights from recent mapping, geochronology, and geochemical studies: Geological Survey of Western Australia, Record 2008/19, 20p.

Smithies, RH, Howard, HM, Evins, PM, Kirkland, CL, Kelsey, DE, Hand, M, Wingate, MTD, Collins, AS and Belousova, E 2011, High-temperature granite magmatism, crust–mantle interaction and the Mesoproterozoic intracontinental evolution of the Musgrave Province, Central Australia: Journal of Petrology, v. 52, no. 5, p. 931–958, doi: 10.1093/petrology/egr010.

Smithies, RH, Howard, HM, Maier, WD and Evins, PM 2009b, Blackstone, WA Sheet 4545: Geological Survey of Western Australia, 1:100 000 Geological Series.

Stewart, AJ 1995, Resolution of conflicting structures and deformation history of the Mount Aloysius granulite massif, western Musgrave Block, central Australia: AGSO Journal of Australian Geology and Geophysics, v. 16, p. 91–105.

Sun, S-S, Sheraton, JW, Glikson, AY and Stewart, AJ 1996, A major magmatic event during 1050–1080 Ma in central Australia, and an emplacement age for the Giles Complex: AGSO Journal of Australian Geology and Geophysics, v. 24, p. 13–15.

Wade, BP, Barovich, KM, Hand, M, Scrimgeour, IR and Close, DF 2006, Evidence for early Mesoproterozoic arc magmatism in the Musgrave Block, Central Australia: implications for Proterozoic crustal growth and tectonic reconstructions of Australia: Journal of Geology, v. 114, p. 43–63.

Wade, BP, Kelsey, DE, Hand, M and Barovich, KM 2008, The Musgrave Province: stitching north, west and south Australia, *in* Assembling Australia: Proterozoic building of a continent: Precambrian Research, v. 166, no. 1–4 , p. 370–386, doi: 10.1016/j.precamres.2007.05.007.

Weaver, JT, Agarwal, AK and Lilley, FEM 2000, Characterization of the magnetotelluric tensor in terms of its invariants: Geophysical Journal International, v. 141, p. 321–336.

White, RW, Clarke, GL and Nelson, DR 1999, SHRIMP U–Pb zircon dating of Grenville-age events in the western part of the Musgrave Block, central Australia: Journal of Metamorphic Geology, v. 17, p. 465–481.

Wight, DE and Bostick, FX 1981, Cascade decimation — a technique for real time estimation of power spectra: Institute of Electrical and Electronic Engineers; International Conference on Acoustics, Speech, and Signal Processing, Atlanta, Georgia, USA, 30 March 1981; Proceedings, p. 626–629.

Appendix

Apparent resistivity and phase data

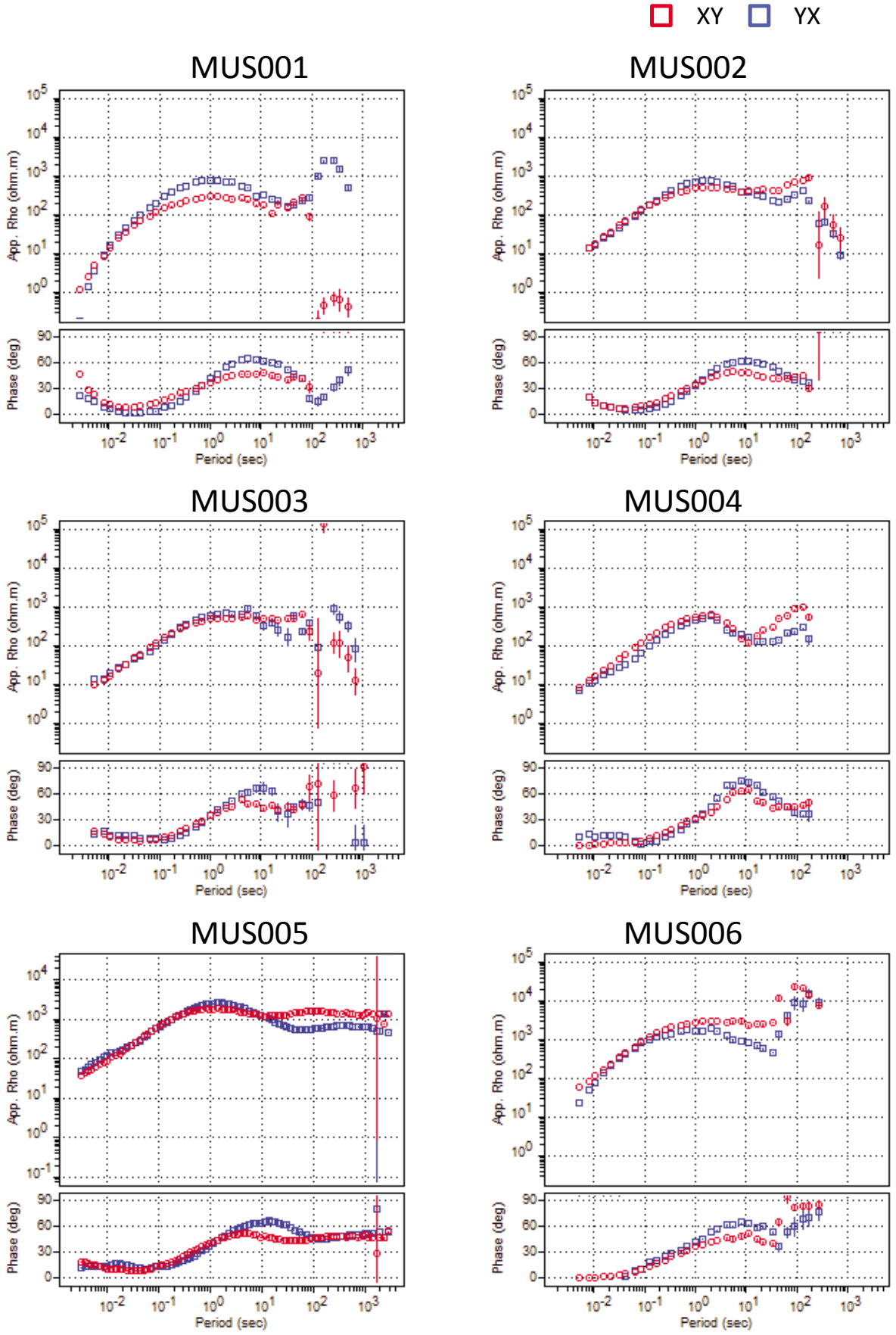

XY YX

MUS007

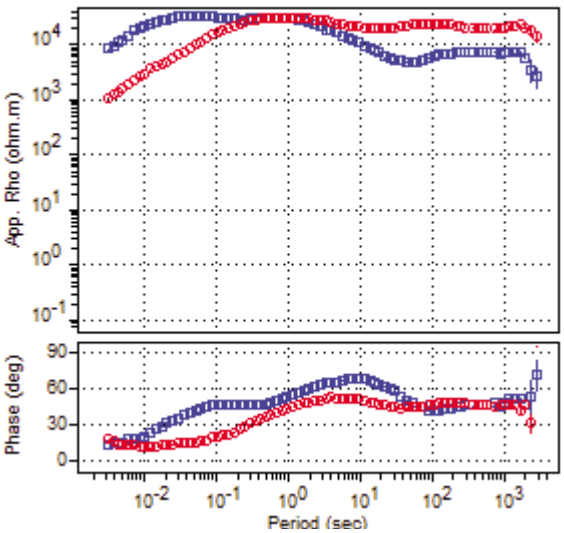

MUS008

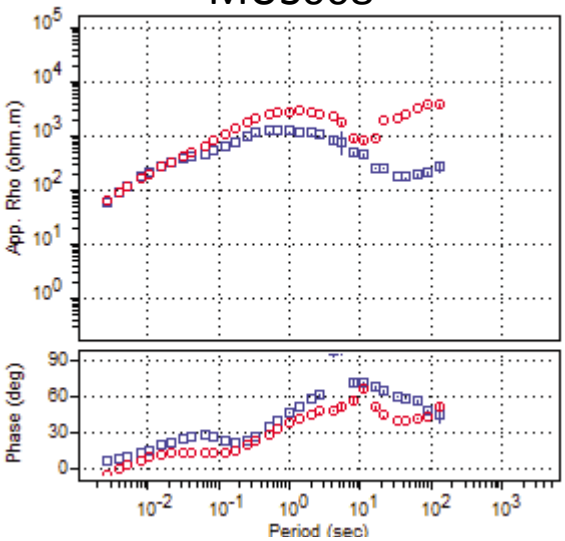

MUS009

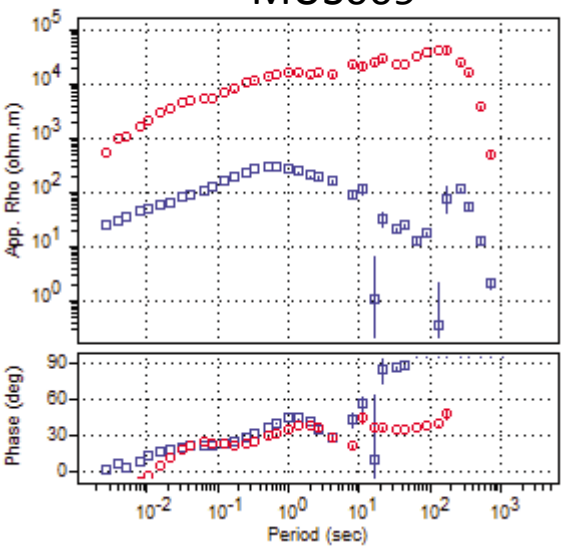

MUS010

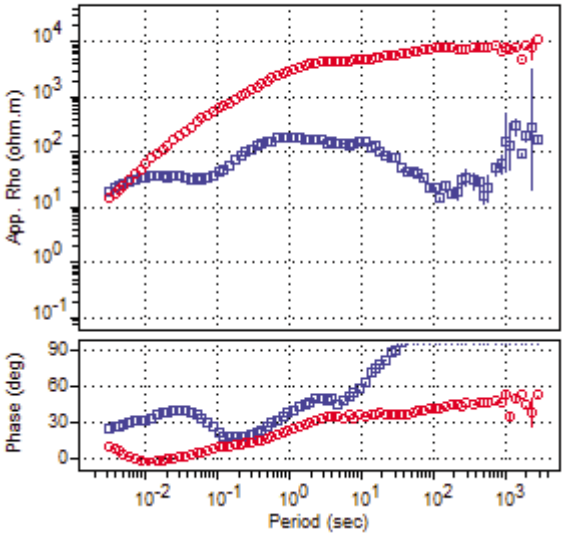

MUS011

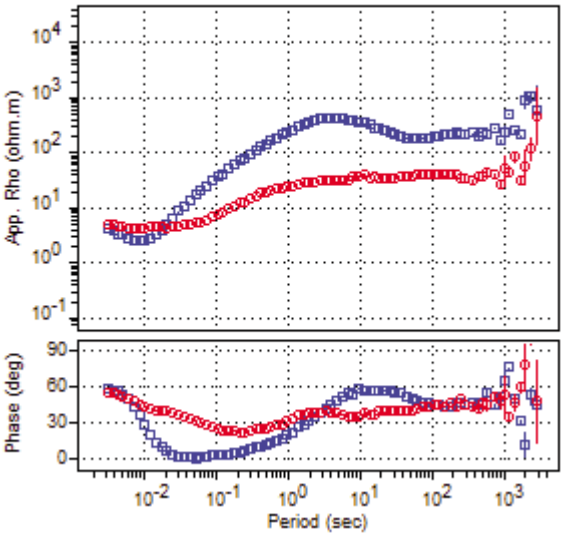

MUS012

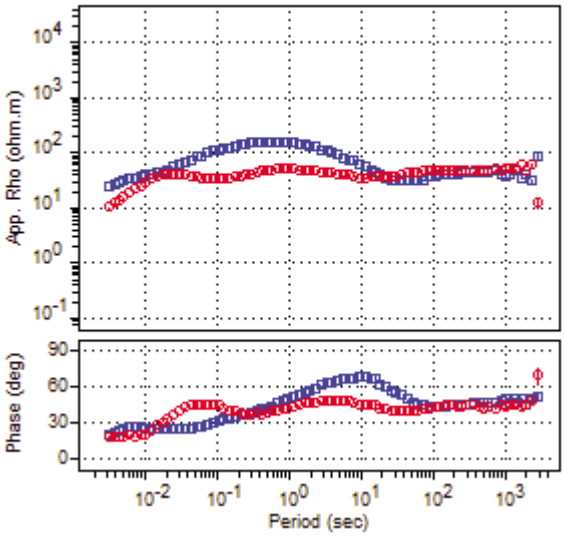

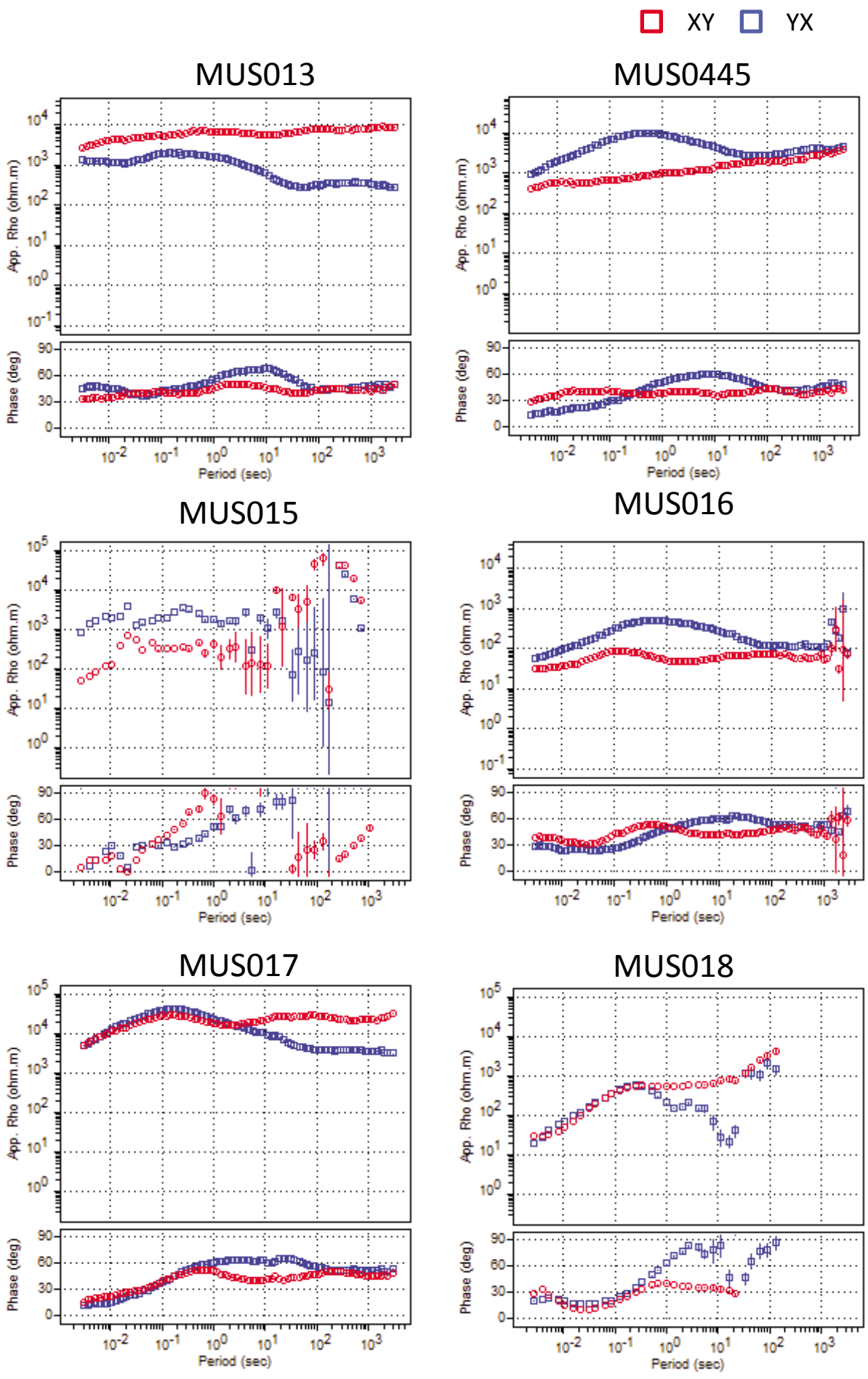
XY
YX
MUS013
MUS0445
MUS015
MUS016
MUS017
MUS018
App. Rho (ohm.m)
Phase (deg)
Period (sec)

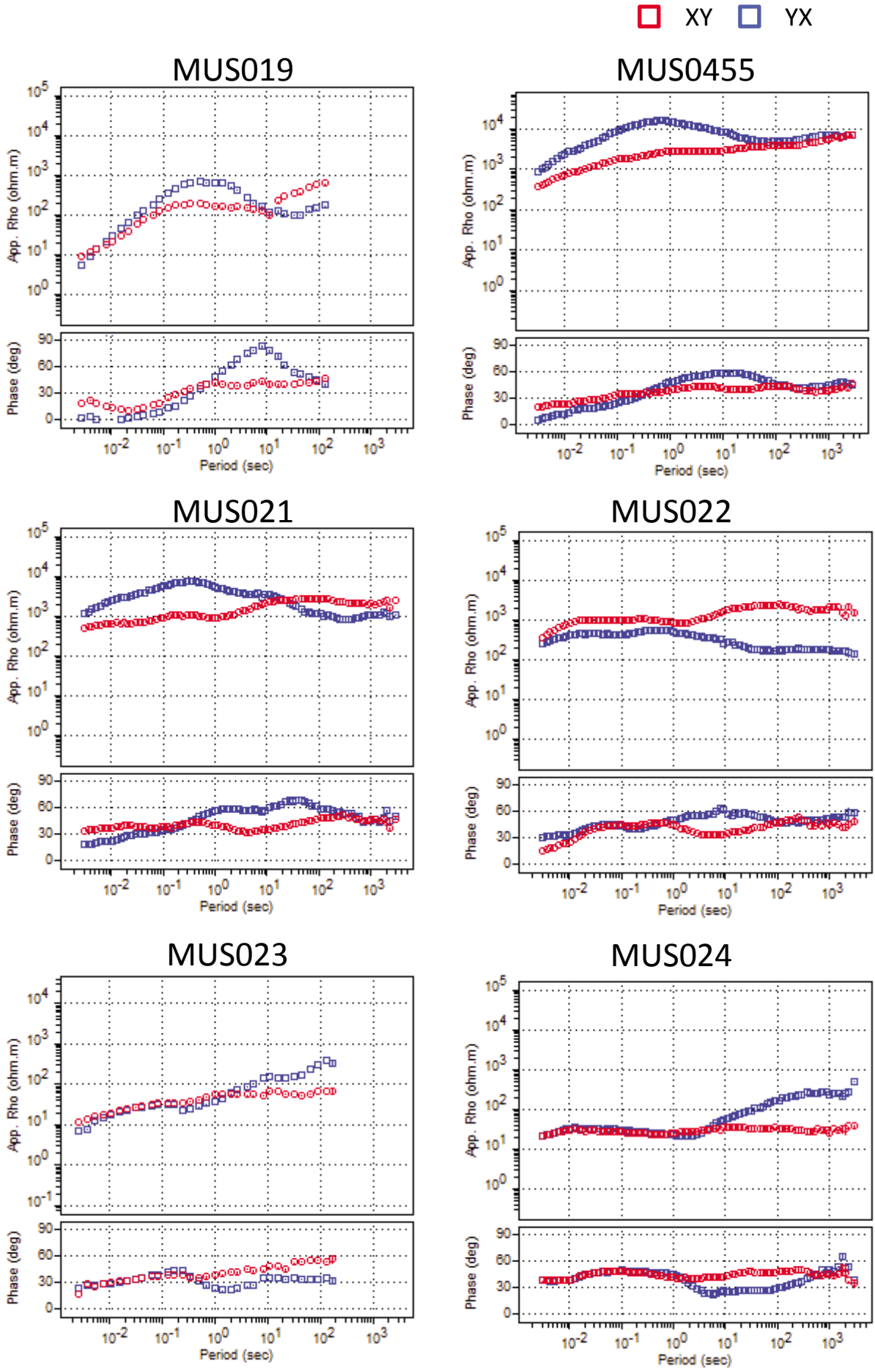
XY
YX
MUS019
MUS0455
MUS021
MUS022
MUS023
MUS024
App. Rho (ohm.m)
Phase (deg)
Period (sec)

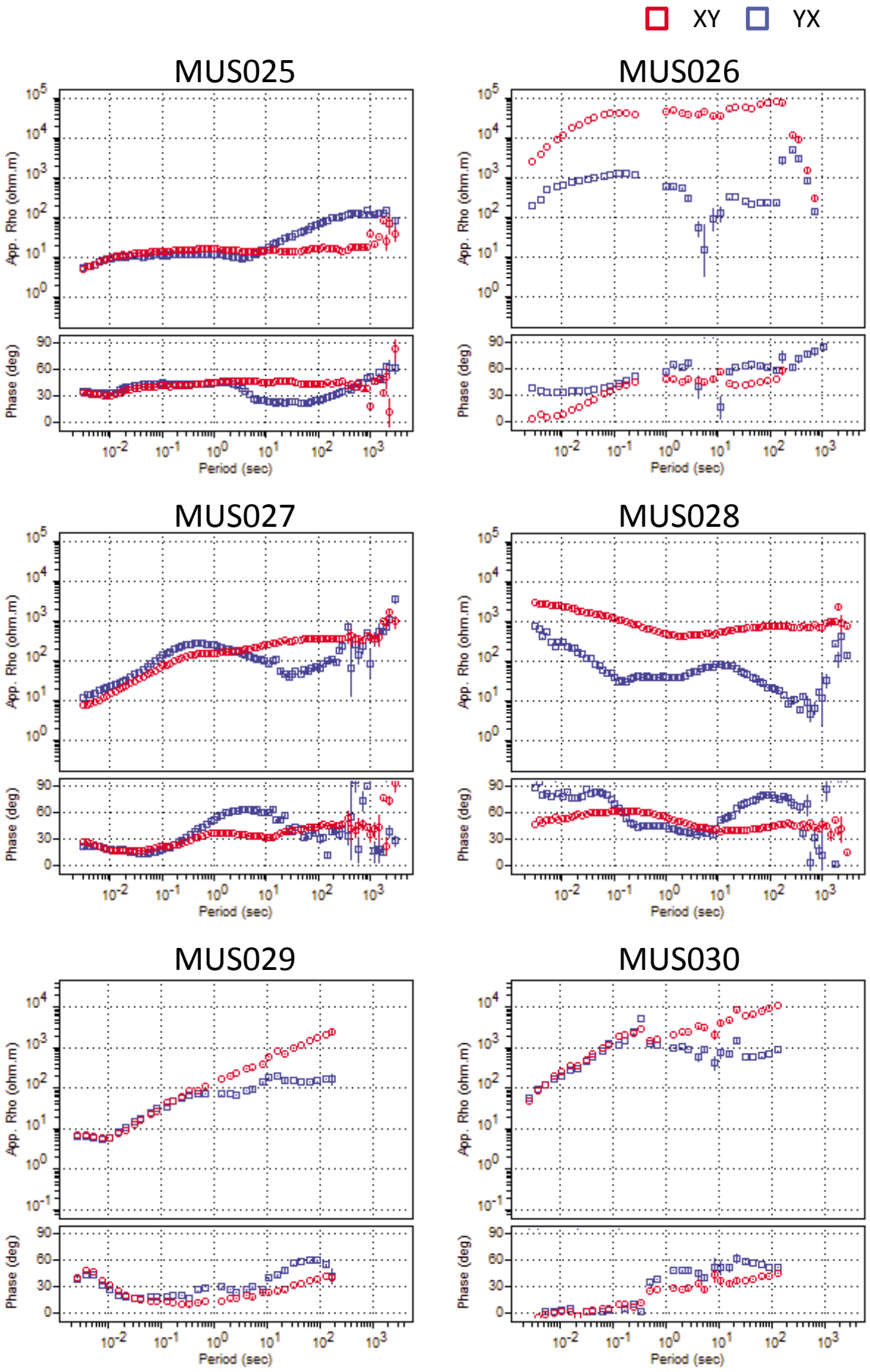
XY
YX
MUS025
MUS026
MUS027
MUS028
MUS029
MUS030
App. Rho (ohm.m)
Phase (deg)
Period (sec)

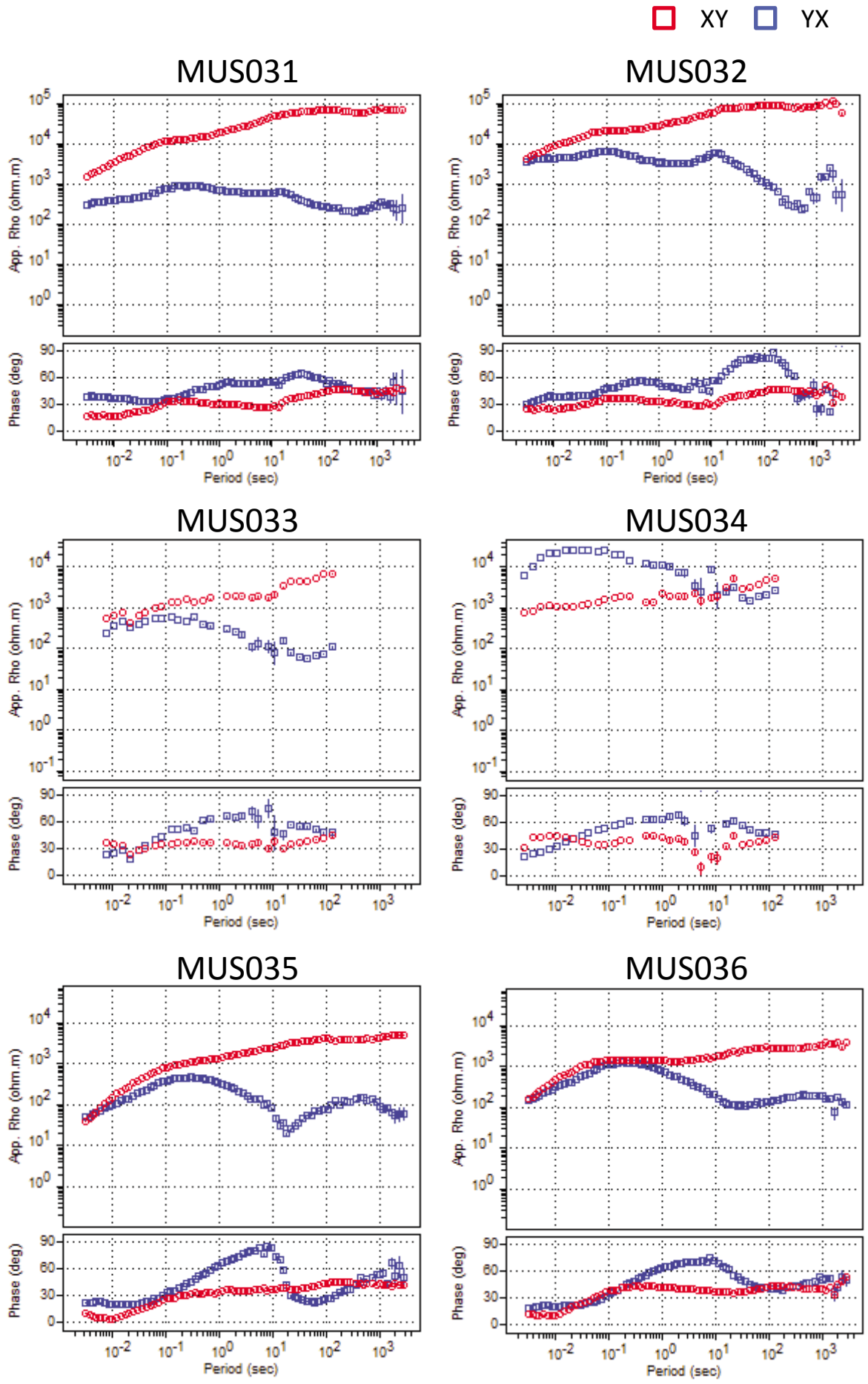
XY
YX
MUS031
MUS032
MUS033
MUS034
MUS035
MUS036
App. Rho (ohm.m)
Phase (deg)
Period (sec)

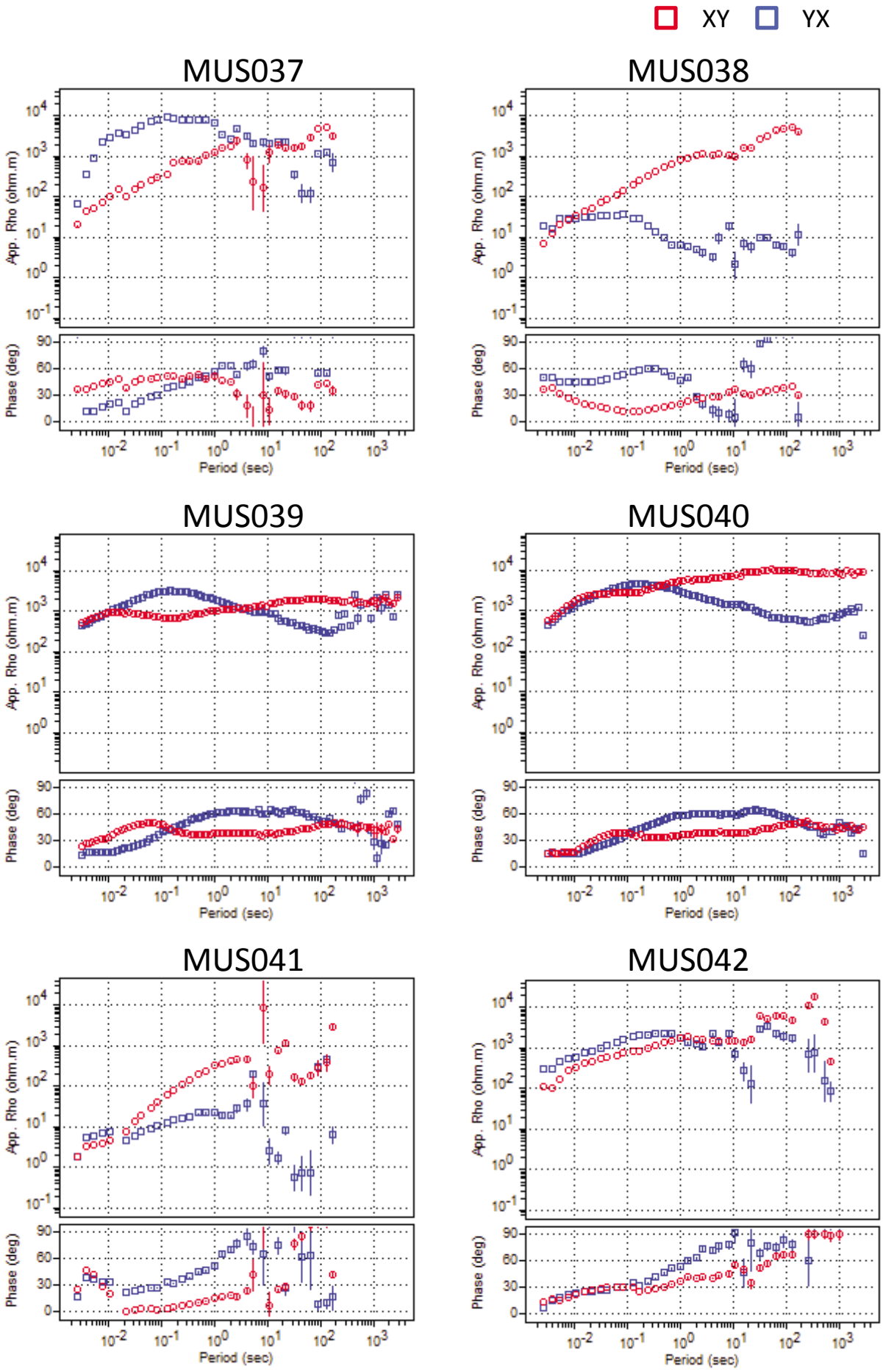
XY
YX
MUS037
MUS038
MUS039
MUS040
MUS041
MUS042
App. Rho (ohm.m)
Phase (deg)
Period (sec)

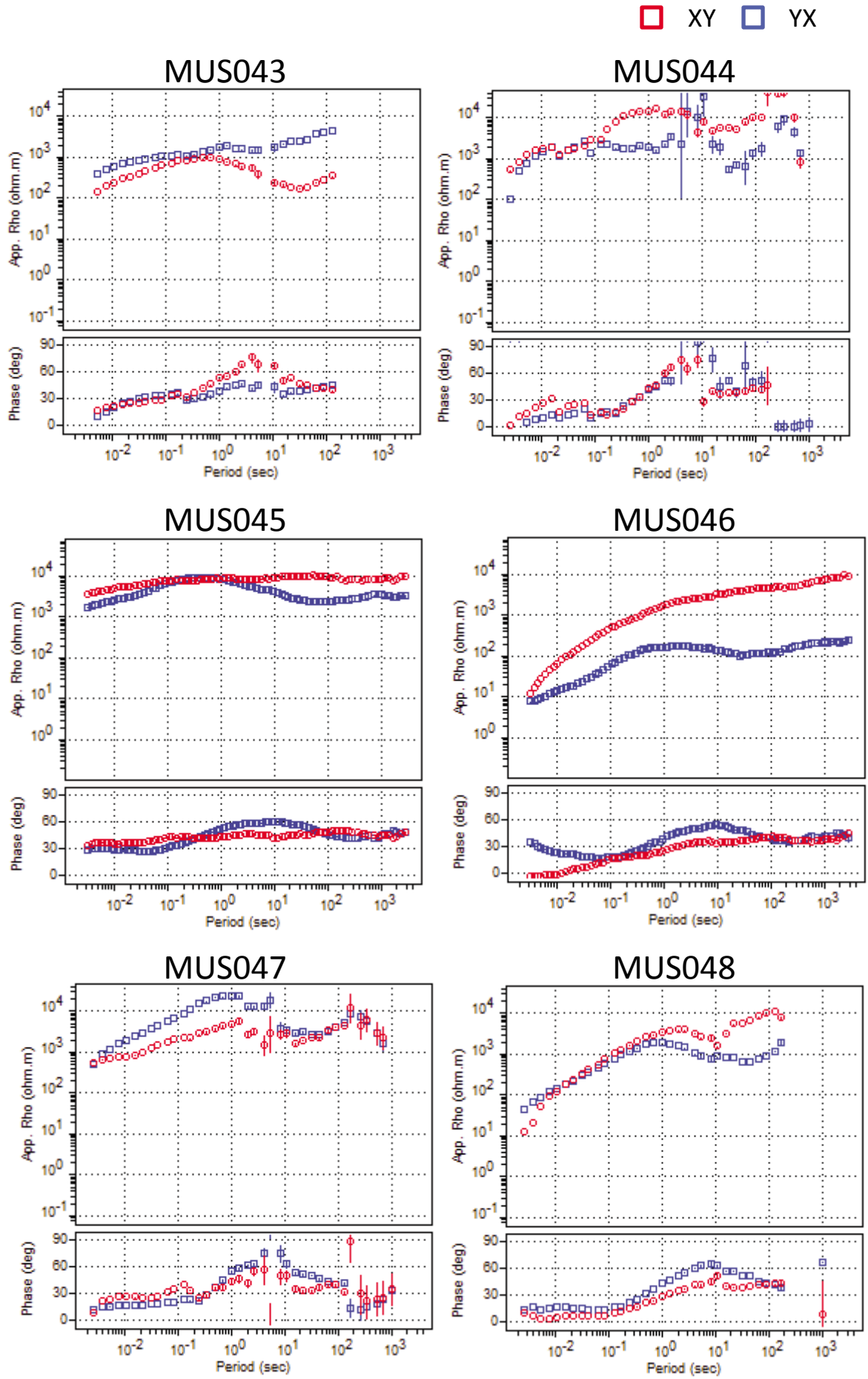
XY
YX
MUS043
MUS044
MUS045
MUS046
MUS047
MUS048
App. Rho (ohm.m)
Phase (deg)
Period (sec)

XY YX

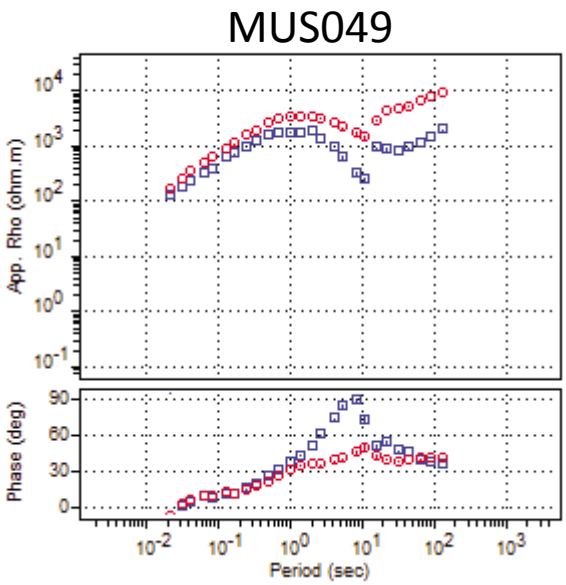

The west Musgrave Province was a focal point for tectonic activity from the Mesoproterozoic through to the latest Proterozoic and is prospective for several commodities, principally Ni, Cu, and PGEs, but also gold and base metals. We use magnetotelluric, gravity, and magnetic data to determine the crustal structure of this region, including economically important features such as major shear zones and intrusions. The Giles Event dominates the south and west of the area investigated, characterized by the intrusion of ~8–10-km-thick intrusions into the upper crust and the deposition of the volcanic-sedimentary Bentley Supergroup. Magmatic layering consistently dips shallowly to the south or southwest, but is disrupted in many places by faulting and folding that occurred late in the Giles Event and during other events. The Petermann Orogeny involves fold–thrust geometries in the footwall of the Woodroffe Thrust, low-angle thrusts and crustal flow zones in the hanging wall of the Woodroffe Thrust, and high-angle transpressional shear zones in the orogenic hinterland.

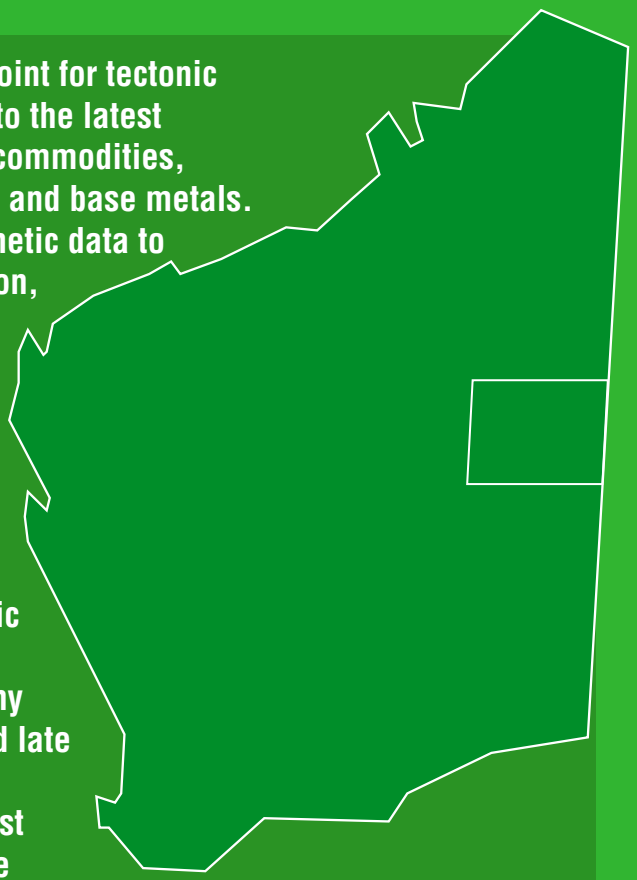

Further details of geological products and maps produced by the Geological Survey of Western Australia are available from:

Information Centre
Department of Mines and Petroleum
100 Plain Street
EAST PERTH WA 6004
Phone: (08) 9222 3459 Fax: (08) 9222 3444

www.dmp.wa.gov.au/GSWApublications

Aitkin et al.

IMAGING CRUSTAL STRUCTURE IN THE WEST MUSGRAVE PROVINCE FROM MAGNETOTELLURIC AND POTENTIAL FIELD DATA

REPORT 114